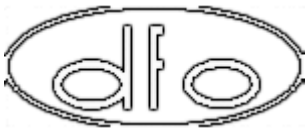

Università degli Studi di Milano – Bicocca

Analysis of surface radioactive background contribution and study of rare decays in the CUORE experiment

Supervisor : Prof. Ezio PREVITALI

Thesis submitted for the degree of Ph.D.
by

Cecilia G. MAIANO

UNIVERSITÀ DEGLI STUDI DI MILANO-BICOCCA

Analysis of surface radioactive background contribution and study of rare decays in the CUORE experiment

Cecilia G. Maiano

Supervisor:
Prof. Ezio PREVITALI

A thesis submitted for the
degree of Doctor of Philosophy in Physics and Astronomy
in the
Dipartimento di Fisica G. Occhialini

March 4^{th}, 2011

cecilia.maiano@mib.infn.it

'Science is a wonderful thing if one does not have to earn one's living at it.'

Albert Einstein.

Contents

List of Figures

List of Tables

To my sweet sister Francesca

Chapter 1

Introduction

Rare Physics event is playing a crucial role, not only in Fundamental Interaction Physics, but also in Astroparticle Physics and in Cosmology. These signals, if detected, woul give an importatnt evidence of *new* Physics.

The CUORE experiment (Cryogenic Underground Observatory for Rare Events) is a proposed tightly packed array of 988 TeO_2 bolometers, each being a cube 125 cm^3 on a side with a mass of 750 g. The array consists of 19 vertical towers, arranged in a compact cylindrical structure. Each tower will consist of 13 layers of 4 crystals. The design of the detector is optimized for ultralow-background searches.
Neutrinoless double-beta decay ($\beta\beta0\nu$) is the main goal of CUORE. What is new is the fact that positive observation of neutrino oscillations gives new motivation for more sensitive searches.
Neutrino oscillation experiments can only provide data on the mass differences of the neutrino mass-eigenstates. The absolute scale can only be obtained from direct mass measurements (β-decay end point measurements), or in the case of Majorana neutrinos, more sensitively by neutrinoless double-beta decay observation.
$\beta\beta0\nu$ is not the only exotic process which can be observed in the CUORE experiment. Other rare events, from cold dark matter, to rare nuclear decays and electron decay can in principle be studied with the CUORE experimental facility. I will discuss the last process in the 6^{th} chapter.

The topic which joins the exotic and rare processes discussed is the unwanted radioactive background which is inevitably present in the experimental measurements.

CUORICINO, almost a single CUORE tower, was constructed as a smaller scale experiment and operated from december 2003 to June 2008. Besides being a sensitive experiment on ^{130}Te double beta decay, CUORICINO is a conclusive test of CUORE. CUORICINO provided important results concerning both the technical performances of the bolometric tower (CUORE will be made of 19 such towers), the *background level* .In particular, one of the information gained is that the most probable candidates for the continuum background observed in the spectra, are the surface α contaminations of the copper mounting frame.

Silicon Barrier Detectors (SBD) are a powerful instrument to study charged particle radiation (like α particles). During my PHD one of the activity I focused on was the optimization of the SBD used in the radioactivity laboratoty of the the University of Milano Bicocca A complete procedure for the calibration of these detectors was settled. In fact, one of the main problem to face with, (due also to the extremely low activity measured), is the discrimination of their intrinsic background level from that of the sample measured. The SBD are always operated in Ultra Low Background vacuum chambers. In the context of the discrimination of the background, evaluation of the muon and shower contribution to the acquired spectra were performed. The latter were done through a coincidence measurement between the SBD and a scintillator. The result of the measurements and of their ananlysis showed that the major contribution to the spurious counts comes from the showers.
A dedicated acquisition was done for the detectors, with a module which lets to have event's temporal imformation. To give limits on the surface activities of the samples the use of Monte Carlo (MC) simulation is mandatory in order to have an estimation of the efficiency of energy detection. The use of the MC simulation was optimized: different depht and profiles of contamination were studied and tested. This optimization allows to give limits on surface ^{232}Th, ^{238}U and ^{210}Pb-Po activities which depend on the depht of contamination. The drastic reduction of the sensitivity achieved (from 10^{-5} to 10^{-7} and 10^{-8} Bq $\cdot$ cm^2 fo the cleanest material measured) is due to the described optimization. Last, but non least, the SBD measurements played a crucial role in the material selection, depending on the radiopurity required, for the CUORE experiment.

Concering the $\beta\beta0\nu$, a crucial role, in the theoretical interpretation of the experimental result, is played by the Nuclear Matrix Element (NME) used to transalte the observed rate (in the energy region where the signal is expected) in a sensitivity on the effective neutrino mass $|m\nu|$. In fact, the formula which relates the rate to $|m_\nu|$ is: $\tau_{0\nu}^{1/2} = G_{0\nu} \cdot |M_{0\nu}|^2 \cdot \frac{|m_\nu|^2}{m_e^2}$ where $\tau_{0\nu}^{1/2}$ is the half life for $\beta\beta0\nu$ decay; $G_{0\nu}$ is the phase space factor, $|M_{0\nu}|$ is the NME and m_e is the electron mass. I performed a study in order to compare and understand the different nuclear models used nowadays, and the respective Phase Space Factors (PSF) used. This study allows to compare, in a quantitative way, the different experiments on neutrinoless double beta decay. A database was realized in which all the inputs are collected, comments and references on NME and PSF are illustrated and the kind of short range correlation is used in the calculation of the matrix element. The database, with the information collected and properly organized, allows to evaluate the sensitivity on $|m_\nu|$ of all the experiments now at work, depending on the nuclear model used. The difficulties encountered in the comprehension of the nuclear models and in the PSF used are due to three main reasons.

- the PSF shoul be in principle standard and unambiguous, not depending on the nuclear model, but just on the initial and final states J^P. This is not what the study showed: the PSF, in the different formulation, show discrepancies of a factor 5 or 6.
- the nuclear models assume different approaches to the process and should lead to different results. Two models, i.e., the Shell Model and the IBM (Interactive Boson Model) have a similar approach, but they differ in handling the states which are 'far from closed shells', so in the handling of the nuclear deformations. The QRPA, (in the version pnQRPA an rQRPA, Quasi Random Phase Approximation), have

a different approach to the previous models, because it introduces the concept of quasiparticle, which are states built with a 'mixing' of creation and annihilation operators (a theory very similar to BCS for the superconductivity) and it leads to a correlation between particles and holes and not just between particles (g_{ph} and not only g_{pp} pairing).

- the SRC (shot range correlation) used should be univocal, but this is not the case. The theoreticians don't give a clear choice of the proper SRC to be used.

Finally I performed a study on the electron decay, in the channel $e^- \leftarrow \gamma + \nu$, using CUORICINO data. Moreover I performed a calculation of the cross section for the process, assuming a massless neutrino in the first step and a massive neutrino in the second step. The study of the channel implies to evaluate the signature of the decay, which depends on the material and atomic shell from which the electron disappears. In fact the visible energy changes if the decay happens in the active volume of the detector or in the surroinding materials: $E_v = \frac{(m_e c^2 - E_b)}{2} + E_X = \frac{(m_e c^2 + E_b)}{2}$ where m_e is the electron mass, E_b is the binding energy, E_X is the X-ray energy following the decay. The last term is included only if the decay happens inside the active volume of the detectors. Thus, there are several signatures which can be discriminated from the background only if the detector resolution is excellent. Moreover the doppler broadening of the lines, due to the orbital motion of the electron in the shell, must be considered. I thus studied the different signatures in several materials, (potential emitters). In the analysis I included the efficiences for the signatures, using Monte Carlo simulations, expressely conformed to experimental set-up and charachteristics (such as real thresholds, active channels). The correction to the efficiencies, i.e. the loss of 'good events', due to the analysis cuts, was evaluated. All the analysis done led to a promising result for this decay, in competition with the current limits given from other collaborations.
The cross section calculation allowed to give an estimation of the CNC parameter, using as inputs the available experimental data.
Introduction

Chapter 2

Rare physics event

2.1 Introduction: why beyond the Standard Model

What is the physics beyond the standard model? This is in some sense an ill-defined assignment, because it is a vast subject for which physicists know pratically nothing about. It is vast because there are so many possibilities and speculations, and a lot of ink and many many pages of paper had been devoted to explore it. On the other hand, we know practically nothing about it by definition, because if we did, it should be a part of the standard model of particle physics already. I will therefore focus more on the motivation *why* we should consider physics beyond the standard model and discuss a few candidates.

2.1.1 Particle and Cosmology

Which is the connection between Particle and Cosmology? At the first sight, it seems strange to talk about particle physics and cosmology together. Cosmology is the study of the universe, where the distance scale involved is many Gigaparsecs $\sim 10^{28}$ cm. Particle physics studies the fundamental constituent of matter, now reaching the distance scale of $\sim 10^{-17}$ cm. How can they have anything in common? The answer is the Big Bang. Discovery of Hubble expansion showed that the visible universe was much smaller in the past, and the study of cosmic microwave background showed the universe was filled with a hot plasma made of photons, electrons, and nuclei in thermal equilibrium. It was hot. As we contemplate earlier and earlier epochs of the universe, it was correspondingly smaller and hotter.

On the other hand, the study of small scales d in particle physics translates to large momentum due to the uncertainty principle, $\mathrm{p} \sim \hbar/d$. Since large momentum requires relativity, it also means high energy $\mathrm{E} \sim \mathrm{cp} \sim \mathrm{c/d}$. Physics at higher energies is relevant for the study of higher temperatures $\mathrm{T} \sim \mathrm{E/k}$, which was the state of the earlier universe.
This way, Big Bang connects microscopic physics to macroscopic physics. And we have already seen two important examples of this connection.

Atomic and molecular spectroscopy is based on quantum physics at the atomic distance d $\sim 10^{-8}$ cm. This spectroscopy is central to astronomy to identify the chemical composition of faraway stars and galaxies which we never hope to get to directly and measure their redshifts to understand their motion including the expansion of the space itself. The cosmic microwave background also originates from the atomic-scale physics when the universe was as hot as T $\sim$ 4000 K and hence was in the plasma state. This is the physics which we believe to understand from the laboratory experiments and knowledge of quantum mechanics and hence we expect to be able to extract interesting information about the universe. Ironically, cosmic microwave background also poses a 'wall' because the universe was opaque and we cannot 'see' with photons the state of the universe before this point. We have to rely on other kinds of 'messengers' to extract information about earlier epochs of the universe.

FIGURE 2.1: Potential messangers from the early universe

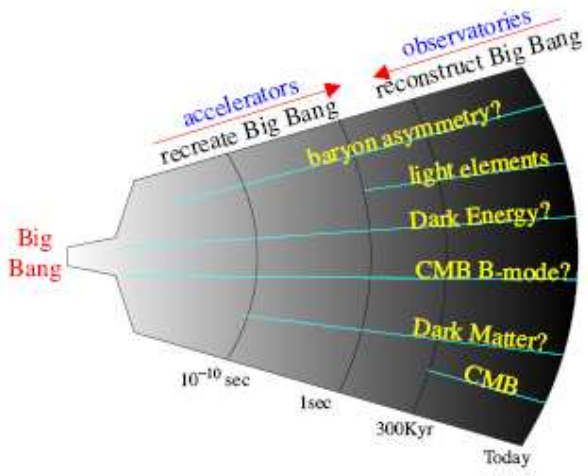

The next example of the micro-macro connection concerns with *nuclear physics*. The stars are powered by nuclear fusion, obviously a topic in nuclear physics. This notion is now well tested by the recent fantastic development in the study of solar neutrinos, where the core temperature of the Sun is inferred from the helioseismology and solar neutrinos which agree at better than a percent level. Nuclear physics also determines death of a star. Relatively heavy stars even end up with nuclear matter, i.e. neutron stars, where the entire star basically becomes a few kilometer-scale nucleus. On the other hand, when the universe was as hot as MeV (ten billion degrees Kelvin), it was too hot for protons and neutrons to be bound in nuclei. One can go through theoretical calculations on how the protons and neutrons became bound in light nuclear species, such as deuterium, ^{3}He, ^{4}He, ^{7}Li, based on the laboratory measurements of nuclear fusion cross sections, as well as number of neutrino species from LEP (Large Electron Positron collider at CERN). This process is called Big-Bang Nucleosynthesis (BBN). There is only one remaining free parameter in this calculation: *cosmic baryon density*. The resulting predictions can be compared to astronomical determinations of light element abundances by carefully

selecting the sites which are believed to be not processed by stellar evolutions. There is reasonable agreement between the observation and theoretical predictions (see, e.g., [1]). This agreement gives us confidence that we understand the basic history of the universe since it was as hot as MeV.

We currently do not have messengers from epochs in early universe above the MeV temperature. In other words, our understanding of early universe physics is not tested well for T $\sim>$ MeV. Many of the topics discussed here are possible messengers from earlier era: dark matter (10^3 GeV?), baryon asymmetry of the universe (10^{10} GeV?), density perturbations (scalar and tensor components) from the inflationary era (10^{16} GeV?). These are the energy scales that laboratory measurements have not reached to reveal the full particle spectrum and their interactions, hence the realm of physics beyond the standard model. Understanding of such early stages of the universe requires the development in particle physics, while the universe as a whole may be regarded as a testing ground of hypothesized particle physics at high energies beyond the reach of accelerators. This way, cosmology and particle physics help and require each other.

2.1.2 Next Threshold

There is a strong anticipation in the physicist community that we are just about to reveal a new threshold in physics. Let's discuss why from a historical perspective. The physicists do not witness crossing a new threshold very often, but each time it happened, it resulted in a major change in the understanding of Nature.

Around year 1900, the threshold of atomic scale was crossed. It is impressive to recall how much progress chemists have made without knowing the underlying dynamics of atoms and molecules. But the empirical understanding of chemistry had clear limitation. For example, van der Waals equation of state showed there was the distance scale of about 10^{-8} cm below which the state-of-art scientific knowledge of the time could not be applied, namely the size of atoms. Once the technology improved to study precision spectroscopy that allowed people to probe physics inside the atoms, a revolution followed. It took about three decades for quantum mechanics to be fully developed but it forever changed our understanding of nature. The revolution went on well into the 40's when the marriage of quantum mechanics and relativity was completed in *Quantum ElectroDynamics*.

Next important threshold was crossed around 1950 when new hadron resonances and strange particles were discovered, crossing the threshold of the strong interaction scale $\sim 10^{-13}$ cm. Discovery of a zoo of elementary particles led to a great deal of confusion for about three decades. It eventually led to the revelation of non-perturbative dynamics of quantum field theory, namely confinement of quarks, dimensional transmutation, and dynamical symmetry breaking of chiral symmetry. More importantly, it showed a new layer in nature where quarks and gluons take over the previous description of subatomic world with protons and neutrons. One more force that is yet to be fully understood is the weak interaction. Its scale was known from the time of Fermi back in 1933 when he wrote the first theory of nuclear beta decay. The theory contained one dimensionful constant. $GF \approx (300GeV)^{-2} \approx (10^{-16}cm)^2$. Seven decades later, we are just about to reach this energy scale in accelerator experiments, at Tevatron and LHC. We do

not really know what Nature has in store for us, but at least we have known all along that this is another important energy scale in physics. If we are not misled, this is the energy scale associated with the cosmic superconductor. Just like the Meissner effect lets magnetic field penetrate into a superconductor only over a finite distance, the cosmic superconductor lets the weak force carried by W and Z bosons go over a tiny distance: a billionth of a nanometer. Right now we are only speculating what revolution may take place at this distance scale. A new layer of matter? New dimensions of space? Quantum dimensions? Maybe string theory? We just don't know yet.
Of course historical perspective does not guarantee that history repeats itself in an equally exciting fashion. But from all what we know, there is a good reason to think that indeed a new threshold is waiting to be discovered at the TeV energy scale, as I will discuss in the next section.

Another simple fact is that crossing a new threshold is something like twice-in-a-century experience.

An interesting question is what fundamental physics determines these thresholds. The atomic scale, that looked like a fundamental limitation in understanding back in the 19^{th} century, did not turn out to be a fundamental scale at all. It is a derived scale from the mass of the electron and the fundamental constants,

$$a_B = \frac{\hbar^2}{e^2 m_e} \approx 10^{-8} cm$$

The strong-interaction scale is also a derived energy scale from the coupling constant Because of the asymptotic freedom, the strong coupling constant is weak at high energies, while it becomes infinitely strong at low energies. The scale of strong interaction is where the strength of the interaction blows up. In other words, the two thresholds crossed so far were extremely exciting, yet they turned out to be not fundamental. They point to yet deeper physics that determines these parameters in nature. Maybe the weak-interaction scale is also a derived scale from some deeper physics at yet shorter distances.

2.1.3 Empirical reasons

Until about ten years ago, particle physicists lamented that the standard model described every new data that came out from experiments and we didn't have a clue what may lie beyond the standard model. Much of the discussions on physics beyond the standard model therefore were not based on data, but rather on theoretical arguments, primarily philosophical and aesthetic displeasure with the standard model. It all changed the last ten years when empirical evidence appeared that demonstrated that the standard model is incomplete:

- Neutrino mass
- Non-baryonic dark matter
- Dark energy
- Baryon asymmetry.

The bottom line is simple: we already know that there must be physics beyond the standard model. However, we don't necessarily know the energy (or distance) scale for this new physics, nor what form it takes. One conservative approach is to try to accommodate all of these established empirical facts into the standard model with minimum particle content: The New Minimal Standard Model [5]. Theoretical arguments suggest the true model be much bigger, richer, and more interesting.

2.1.4 Philosophical and Aesthetic Reasons

What are the theoretical arguments that demand physics beyond the standard model? They are based on somewhat philosophical arguments and aesthetic desires and not exactly on firm footing.
Nonetheless they are useful and suggestive, especially because nature did solve some of the similar problems in the past by invoking interesting mechanisms. A partial list is

- Hierarchy problem: why $\mathrm{G}_F \sim 10^5$ GeV^{-2} $<<$ $\mathrm{G}_N \sim 10^{38}$ GeV^{-2} ?
- Why are there three generations of particles?
- Why are the quantum numbers of particles so strange, yet do anomalies cancel so non-trivially?

To understand what these questions are about, it is useful to remind ourselves how the standard model works. It is a gauge theory based on the $SU(3) \otimes SU(2) \otimes U(1)$ gauge group with the Lagrangian

$$L_{SM} = -\frac{1}{4 \cdot g'^2} B_{\mu\nu} B^{\mu\nu} - \frac{1}{2 \cdot g^2} Tr(W_{\mu\nu} W^{\mu\nu}) - \frac{1}{2 g_s^2} Tr(G_{\mu\nu} G^{\mu\nu})$$

$$+ \bar{Q}_i i \not{D} Q_i + \bar{L}_i i \not{D} L_i + \bar{u}_i i \not{D} u_i + \bar{d}_i i \not{D} d_i + \bar{e}_i i \not{D} e_i$$

$$+ Y_u^{ij} \bar{Q}_i u_j \widetilde{H} + Y_u^{ij} \bar{Q}_i d_j \widetilde{H} + Y_d^{ij} \bar{Q}_i e_j \widetilde{H} + h.c$$

$$+ (D_\mu H)^\dagger (D^\mu H) - \lambda (H^\dagger H)^2 - m H^\dagger H + \frac{\theta}{32\pi^2} \epsilon^{\mu\nu\rho\sigma} Tr(G_{\mu\nu} G_{\rho\sigma}) \qquad (2.1)$$

The first two lines describe the gauge interactions The covariant derivatives $\not{D} = \gamma^\mu D_\mu$ in the second line are determined by the gauge quantum numbers.

This part of the Lagrangian is well tested, especially by the LEP/SLC data in the $90's$. However, the quantum number assignments (especially U(1) hypercharges) appear very strange and actually hard to remember. Why this peculiar assignment is one of the things people don't like about the standard model. Many physicists are left with the feeling that there must be a deep reason for this baroque quantum number assignments which had led to the idea of grand unification.

The third line of the Lagrangian comes with the generation index i, j = 1, 2, 3 and it is responsible for masses and mixings of quarks and masses of charged leptons. The quark part has been tested precisely in this decade at B-factories. In addition, it appears unnecessary for nature to repeat elementary particles three times. The repetition of generations and the origin of mass and mixing patterns remains an unexplained mystery in the standard model.

The last line is completely untested. The first two terms describe the Higgs field and its interaction to the gauge fields and itself. Having not seen the Higgs boson so far, it is far frome being established. The mere presence of the Higgs field poses an aesthetic problem. It is the only spinless field in the model, but it is introduced for the purpose of doing the most important job in the model. In addition, we have not seen any elementary spinless particle in nature! Moreover, the potential needs to be chosen with $m^2 < 0$ to cause the cosmic superconductivity which does not give any reason why our universe is in this state. Overall, this part of the model looks very artificial.

The last term is the so-called θ-term in QCD and violates T and CP. The vacuum angle θ is periodic under $\theta \to \theta + 2\pi$, and hence a 'natural' value of θ is believed to be order unity. On the other hand, the most recent experimental upper limit on the neutron electric dipole moment $|d_n| < 2.9 \cdot 10^{-26} e$ cm (90% C.L.) [2] translates to a stringent upper limit $\theta < (1.2 \pm 0.6) \cdot 10^{-10}$. Why θ is so much smaller than the 'natural' value is the strong CP problem, and again the standard model does not offer any explanations.

Now we have more to say about the Higgs sector (the third line). Clearly it is very important because (1) this is the only part of the StandardModel which has a dimensionful parameter and hence sets the overall energy scale for the model, and (2) it has the effect of causing cosmic superconductivity without explaining its microscopic mechanism. For the usual superconductors studied in the laboratory, we can use the same Lagrangian, but it is derived from the more fundamental theory by Bardeen, Cooper, and Schrieffer. The weak attractive force between electrons by the phonon exchange causes electrons to get bound and condense. The Higgs field is the Cooper pair of electrons. And one can show why it has this particular potential. In the standard model, we do not know if Higgs field is elementary or if it is made of something else, nor what mechanism causes it to have this potential.

All the puzzles raised here (and more) cry out for a more fundamental theory underlying the Standard Model. What history suggests is that the fundamental theory lies always at shorter distances than the distance scale of the problem. For instance, the equation of state of the ideal gas was found to be a simple consequence of the statistical mechanics of free molecules. The van der Waals equation, which describes the deviation from the ideal one, was the consequence of the finite size of molecules and their interactions. Mendeleev's periodic table of chemical elements was understood in terms of the bound electronic states, Pauli exclusion principle and spin. The existence of varieties of nuclide was due to the composite nature of nuclei made of protons and neutrons. The list could go on and on. Indeed, seeking answers at more and more fundamental level is the heart of the physical science, namely the reductionist approach.

The distance scale of the Standard Model is given by the size of the Higgs boson condensate $v = 250$ GeV. In natural units, it gives the distance scale of $d \sim c/v = 0.8 \cdot 10^{-16}$ cm. We therefore would like to study physics at distance scales shorter than this eventually, and try to answer puzzles whose partial list was given in the previous section. Then the idea must be that we imagine the Standard Model to be valid down to a distance scale shorter than d, and then new physics will appear which will take over the Standard Model. But applying the Standard Model to a distance scale shorter than d poses a serious theoretical problem. In order to make this point clear, we first describe a related problem in the classical electromagnetism, and then discuss the case of the Standard Model later along the same line [6].

2.2 Positron Analogue

In the classical electromagnetism, the only dynamical degrees of freedom are electrons, electric fields, and magnetic fields. When an electron is present in the vacuum, there is a Coulomb electric field around it, which has the energy of

$$\Delta E_{Coulomb} = \frac{1}{4\pi\epsilon_0}\frac{e^2}{r_e} \tag{2.2}$$

Here, r_e is the size of the electron introduced to cutoff the divergent Coulomb self-energy. Since this Coulomb self-energy is there for every electron, it has to be considered to be a part of the electron rest energy. Therefore, the mass of the electron receives an additional contribution due to the Coulomb self-energy:

$$(m_e c^2)_{OBS} = (m_e c^2)_{BARE} + \Delta E_{Coulomb} \tag{2.3}$$

Experimentally, we know that the 'size of the electron is small, $r_e <\sim 10^{17}$ cm. This implies that the self-energy ΔE is greater than 10 GeV or so, and hence the 'bare' electron mass must be negative to obtain the observed mass of the electron, with a fine cancellation like

$$0.000511 = (3.141082 + 3.141593)GeV.$$

Even setting a conceptual problem with a negative mass electron aside, such a fine-cancellation between the 'bare' mass of the electron and the Coulomb self-energy appears ridiculous.

In order for such a cancellation to be absent, we conclude that the classical electromagnetism cannot be applied to distance scales shorter than $e^2/(4_0 m_e c^2) = 2.8 \cdot 10^{-13}$ cm. This is a long distance in the present-day particle 'physics' standard.

The resolution to this problem came from the discovery of the anti-particle of the electron, the positron, or in other words by *doubling the degrees of freedom* in the theory. The Coulomb self-energy discussed above can be depicted by a diagram Fig. 2 where the electron emits the Coulomb field (a virtual photon) which is absorbed later by the electron (the electron feels its own Coulomb field).[1]

[1] The diagrams Figs. 2, 3 are not Feynman diagrams, but diagrams in the old-fashioned perturbation theory with different T-orderings shown as separate diagrams. The Feynman diagram for the self-energy is the same as Fig. 2, but represents the sum of Figs. 2, 4 and hence the linear divergence is already cancelled within it. That is why we normally do not hear/read about linearly divergent self-energy diagrams in the context of field theory.

FIGURE 2.2: The Coulomb self-energy of the electron.

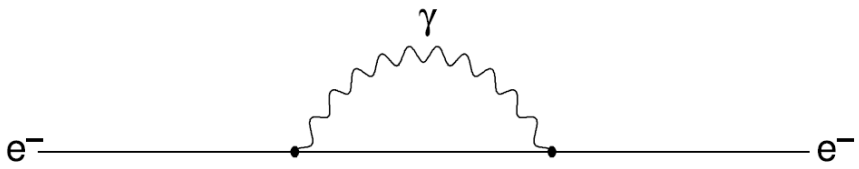

FIGURE 2.3: The bubble diagram which shows the fluctuation of the vacuum.

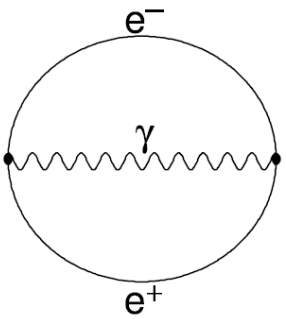

But now that we know that the positron exists (thanks to Anderson back in 1932), and we also know that the world is quantum mechanical, one should think about the fluctuation of the 'vacuum' where the vacuum produces a pair of an electron and a positron out of nothing together with a photon, within the time allowed by the energy-time uncertainty principle $\Delta t \sim \hbar/\Delta E \sim \hbar/2m_e c^2$ (Fig. 2.3). This is a new phenomenon which didn't exist in the classical electrodynamics, and modifies physics below the distance scale $d \sim c\Delta t \sim \hbar c/(2m_e c^2) = 200 \cdot 10^{-13}$ cm. Therefore, the classical electrodynamics actually did have a finite applicability only down to this distance scale, much earlier than $2.8 \cdot 10^{-13}$ cm as exhibited by the problem of the fine cancellation above. Given this vacuum fluctuation process, one should also consider a process where the electron sitting in the vacuum by chance annihilates with the positron and the photon in the vacuum fluctuation, and the electron which used to be a part of the fluctuation remains instead as a real electron (Fig. 2.4). V. Weisskopf [7] calculated this contribution to the electron self-energy, and found that it is negative and cancels the leading piece in the Coulomb self-energy exactly: [2]

$$\Delta E_{PAIR} = -\frac{1}{4\pi\epsilon_0}\frac{e^2}{r_e} \tag{2.4}$$

After the linearly divergent piece $1/r_e$ is canceled, the leading contribution in the $r_e \to 0$ limit is given by

[2] An earlier paper by Weisskopf actually found two contributions to add up. After Furry pointed out a sign mistake, he published an errata with no linear divergence.

$$\Delta E = \Delta E_{PAIR} + \Delta E_{Coulomb} = \frac{3\alpha}{4\pi} m_e c^2 log \frac{\hbar}{m_e c r_e} \tag{2.5}$$

There are two important things to be said about this formula. First, the correction ΔE is proportional to the electron mass and hence the total mass is proportional to the 'bare' mass of the electron

$$(m_e c^2)_{OBS} = (m_e c^2)_{bare} \left[1 + \frac{3\alpha}{4\pi} log \frac{\hbar}{m_e c r_e} \right] \tag{2.6}$$

Therefore, we are talking about the 'percentage' of the correction, rather than a huge additive constant. Second, the correction depends only logarithmically on the Fsize‘ of the electron. As a result, the correction is only a 9% increase in the mass even for an electron as small as the Planck distance $r_e = 1/M_{Pl} = 1.6 \cdot 10^{33}$ cm. The fact that the correction is proportional to the 'bare' mass is a consequence of a new symmetry present in the theory with the antiparticle (the positron): the chiral symmetry. In the limit of the exact chiral symmetry, the electron is massless and the symmetry protects the electron from acquiring a mass from self energy corrections. The finite mass of the electron breaks the chiral symmetry explicitly, and because the self-energy correction should vanish in the chiral symmetric limit (zero mass electron), the correction is proportional to the electron mass. Therefore, the doubling of the degrees of freedom and the cancellation of the power divergences lead to a sensible theory of electron applicable to very short distance scales.

2.3 The Hierarchy Problem

In the Standard Model, the Higgs potential is given by

$$V = m^2 |H|^2 + |H|^4 \tag{2.7}$$

where $v^2 =< H >^2 = \frac{m^2}{2} = (176 GeV)^2$. Because perturbative unitarity requires that $\lambda <\sim 1$, m^2 is of the order of $(100 GeV)^2$. However, the mass squared parameter m^2 of the Higgs doublet receives a quadratically divergent contribution from its self-energy corrections. For instance, the process where the Higgs doublets splits into a pair of top quarks and come back to the Higgs boson gives the self-energy correction

$$\Delta m^2_{top} = -6 \frac{h_t^2}{4\pi^2} \frac{1}{r_H^2} \tag{2.8}$$

where r_H is the 'size' of the Higgs boson, and $h_t \sim 1$ is the top quark Yukawa coupling. Based on the same argument in the previous section, this makes the Standard Model not applicable below the distance scale of 10^{-17} cm. This is the hierarchy problem. In other words, if we don't solve this problem, we can't even talk about physics at much shorter distances without an excessive fine-tuning in parameters. It is worth pondering if the nature may fine-tune. Now that the cosmological constant appears to be fine-tuned at

the level of 10^{-120}, should we be really worried about the fine-tuning of $v^2/M_{Pl}^2 \approx 10^{-30}$ [8] [9] [10].

FIGURE 2.4: The Coulomb self-energy of the electron.

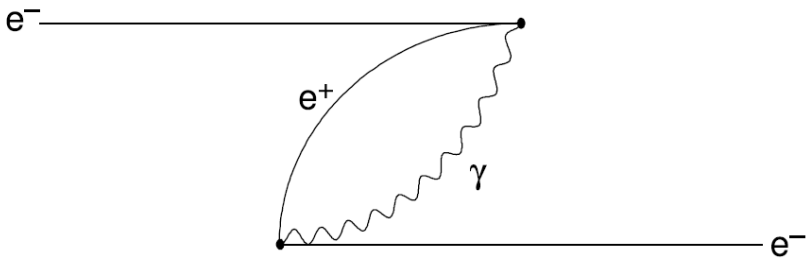

2.4 Examples of Physics Beyond the Standard Model

Given various problems in the standard model discussed in the previous section, especially the hierarchy problem, many possible directions of physics beyond the standard model have been proposed. I will review only a few of them.

2.4.1 Supersymmetry

The motivation for supersymmetry is to make the Standard Model applicable to much shorter distances so that we can hope that the answers to many of the puzzles in the Standard Model can be given by physics at shorter distance scales [11]. In order to do so, supersymmetry repeats what history did with the positron: doubling the degrees of freedom with an explicitly broken new symmetry. Then the top quark would have a superpartner, the stop, whose loop diagram gives another contribution to the Higgs boson self energy.

$$\Delta m_{STOP}^2 = +6\frac{h_t^2}{4\pi^2}\frac{1}{r_H^2} \tag{2.9}$$

The leading pieces in $1/rH$ cancel between the top and stop contributions, and one obtains the correction to be

$$\Delta m_{top}^2 + \Delta m_{top}^2 + 6\frac{h_t^2}{4\pi^2}(m_{\tilde{t}}^2 - m_t^2 log\frac{1}{r_H^2 m_t^2}) \tag{2.10}$$

One important difference from the positron case, however, is that the mass of the stop, $m_{\tilde{t}}$, is unknown. In order for the Δm^2 to be of the same order of magnitude as the tree-level value $m^2 = 2\lambda v^2$, we need $m_{\tilde{t}}^2$ to be not too far above the electroweak scale. TeV stop mass is already a fine tuning at the level of a percent. Similar arguments apply to masses of other superpartners that couple directly to the Higgs doublet. This

is the so-called naturalness constraint on the superparticle masses (for more quantitative discussions, see papers [12]). Supersymmetry doubles the number of degrees of freedom in the standard model. For each fermion (quarks and leptons), you introduce a complex scalar field (squarks and sleptons). For each gauge boson, you introduce gaugino, a partner Majorana fermion (a fermion field whose anti-particle is itself). I do not go into technical aspect of how to write a supersymmetric quantum field theory; some review articles can be c0nsulted [13] [14].
One important point related to dark matter is the proton longevity. We know from experiments such as SuperKamiokande that proton is very long lived (if not immortal). The life time for the decay mode $p \to e^+\pi^0$ is longer than $1.6 \cdot 10^{33}$ years, at least twenty-three orders of magnitude longer than the age of the universe! On the other hand, if you write the most general renormalizable theory with standard model particle content consistent with supersymmetry, it allows for vertices such as $\epsilon_{ijk} u^i d^j \tilde{s}^k$ and $e u^i \tilde{s}_i^*$ (here i, j, k are color indices). Then one can draw a Feynman diagram like one in Fig. 2.5. If the couplings are O(1), and superparticles around TeV, one finds the proton lifetime as short as $\tau_p \sim m_{\tilde{s}}^4/m_p^5 \sim 10^{-12} sec ... too\ short.$

FIGURE 2.5: A possible Feynman diagram with supersymmetric particles that can lead to a too-rapid proton decay $p \to e^+\pi^0$.

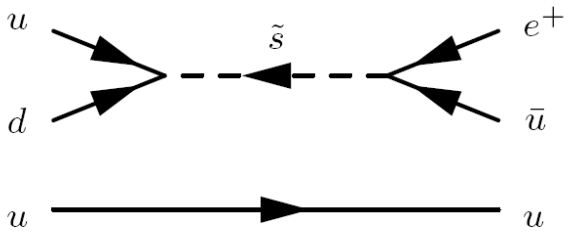

Because of this embarrassment, we normally introduce a $\mathbb{Z}_2$ symmetry called 'R-parity' defined by:

$$R_P = (-1)^{3B+L+2s} = (-1)^{matter} R_{2\pi} \tag{2.11}$$

where s is the spin. What it does is to flip the sign of all matter fields (quarks and leptons) and perform 2π rotation of space at the same time. In effect, it assigns even parity to all particles in the standard model, and odd parity to their superpartners. Here is a quick check. For the quarks, $B = 1/3$, $L = 0$, and $s = 1/2$, and we find $R_p = +1$, while for squarks the difference lies in $s = 0$ and hence $R_p = 1$. This symmetry forbids both of the bad vertices in Fig. 2.5. Once the R-parity is imposed, there are no baryon- and lepton-number violating interaction you can write down in a renormalizable Lagrangian with the standard model particle content. This way, the R-parity makes sure that proton is long lived. Then the lightest supersymmetric particle (LSP), with odd R-parity, cannot decay because there are no other states with the same R-parity with smaller mass it can decay into by definition. In most models it also turns out to be electrically neutral. Then one can talk about the possibility that the *LSP* is the *dark matter of the universe.*

2.4.2 Composite Higgs

Another way the hierarchy problem may be solved is by making the Higgs boson to actually have a finite size. Then the correction in Eq. (2.9) does not require tremendous fine-tuning as long as the physical size of the Higgs boson is about $r_H \approx (TeV)^{-1} \approx 10^{-17}$ cm. This is possible if the Higgs boson is a composite object made of some elementary constituents.
The original idea along this line is called *technicolor* (see reviews [15,16]), where a new strong gauge force binds fermions and anti-fermions much like mesons in the real QCD. Again just like in QCD, fermion anti-fermion pair have a condensate $<\bar{\psi}\psi>\neq 0$ breaking chiral symmetry. In technicolor theories, this chiral symmetry breaking is nothing but the breaking of the electroweak SU(2) $\otimes$ U(1) symmetry to the U(1) QED subgroup. Because the Higgs boson is heavy and strongly interacting, it is expected to be too wide to be seen as a particle state.
It is fair to say, however, that the technicolor models suffer from various problems. First of all, it is difficult to find a way of generating sufficient masses for quarks and leptons, especially the top quark, because you have to rely on higher dimension operators of type $\bar{q}q\bar{\Psi}\psi/\Lambda^2$. The scale Λ must be low enough to generate m_t, while high enough to avoid excessive flavor-changing neutral current. In addition, there is tension with precision electroweak observables. These observables are precise enough that they constrain heavy particles coupled to Z and W- bosons even though we cannot produce them directly.

Because of this issue, there are various other incarnations of composite Higgs idea, which try to get a relatively light Higgs boson as a bound state [17,18]. One of the realistic models is called little Higgs [19, 20]. Because of the difficulty of achieving Higgs compositeness at the TeV scale, we are better off putting off the compositeness scale to about 10 TeV to avoid various phenomenological constraints. Then you must wonder if the problem with Eq. (2.9) comes back. But there is a way of protecting the scale of Higgs mass much lower than the compositeness scale by using symmetries similar to the reason why a pion is so much lighter than a proton. You could arrange the structure of symmetry such that it eliminates the one-loop correction in Eq. (2.9) and the correction arises only at the two-loop level. Then the compositeness $\sim$ 10 TeV is not a problem.
Another attractive idea is to use extra dimensions to generate the Higgs field from a gauge field, called 'Higgs-gauge unification' [21, 22, 23, 24]. We know the mass of the gauge boson is forbidden by the *gauge invariance*. If the Higgs field is actually a gauge boson (spin one), but if it is spinning in extra dimensions, we (as observers stuck in four dimensions) perceive it not to spin. Not only this gives us apparently spinless degrees of freedom, it also provides protection for the Higgs mass and hence solves the hierarchy problem. The best implementation of this line of thinking is probably the *holographic* Higgs model in Refs. [25, 26] which involves the warped extra dimension. It should also be said that many of the ideas mentioned here are closely related to each other [27].
Similarly to the case of supersymmetry, people often introduce a $\mathbb{Z}_2$ symmetry to avoid certain phenomenological embarrassments. In little Higgs theories, treelevel exchange of new particles tend to cause tension with precision electroweak constraints. Then the new states must be sufficiently heavy so that the hierarchy problem is reintroduced. By imposing 'T -parity', new particles can only appear in loops for low-energy processes and the constraints can be easily avoided [28]. Then the lightest T -odd particle (LTP) becomes a candidate for dark matter. In technicolor models, the lightest technibaryon is stable (just like proton in QCD) and a dark matter candidate [29].

2.5 Evidence for Dark Matter

Now we turn our attention to the problem of non-baryonic dark matter in the universe. Even though this is a sudden change in the topic, you will see soon that it is connected to the discussions we had on physics beyond the standard model.
First review basics of observational evidence for non-baryonic dark matter, and then discuss how some of the interesting candidates are excluded. It leads to a paradigm that dark matter consists of unknown kind of elementary particles. By a simple dimensional analysis, we find that a weakly coupled particle at the GeV-scale naturally gives the correct abundance in the current universe. We will take a look at a simple example quite explicitly so that you can get a good feel on how it works. Then I will discuss more attractive dark matter candidates that arise from various models of physics beyond the standard model I discussed in the previous section.
The argument for the existence of 'dark matter', namely mass density that is not luminous and cannot be seen in telescopes, is actually very old. Zwicky back in 1933 already reported the 'missing mass' in Coma cluster of galaxies. By studying the motion of galaxies in the cluster and using the virial theorem (assuming of course that the galactic motion is *virialized*) he determined the mass distribution in the cluster and reported that a substantial fraction of mass *is not seen*. Since then, the case for dark matter has gotten stronger and stronger and most of us regard its existence established by now [32]. Arguably the most important one is the determination of cosmological parameters by the power spectrum of CMB anisotropy. In the fit to the power-law flat ΛCDM model gives

$\Omega_M h^2 = 0.127^{+0.007}_{0.013}$ and $\Omega_B h^2 = 0.0223^{+0.0007}_{0.0009}$[32].

The point here is that these two numbers are different. Naively subtracting the baryon component, and adding the errors by quadrature, I find $(\Omega_M - \Omega_B)^2 = 0.105^{+0.007}_{0.0136} \neq 0$

at a very high precision. This data alone says most of the matter component in the universe is not atoms, something else.
Another important way to determine the baryon density of the universe is based on Big-Bang Nucleosynthesis (BBN). The baryon density is consistent with what is obtained from the CMB power spectrum, $\Omega_B h^2 = 0.0216^{+0.0020}_{0.0021}$ from five best measurements of deuterium abundance [33] using hydrogen gas at high redshift (and hence believed to be primordial) back-lit by quasars. This agrees very well with the CMB result, even though they refer to very different epochs: T $\sim$ 1 MeV for BBN while T $\sim$ 0.1 eV for CMB.
A novel technique to determine M uses large-scale structure, namely the power spectrum in galaxy-galaxy correlation function. As a result of the acoustic oscillation in the baryon-photon fluid, the power spectrum also shows the 'baryon oscillation' which was discovered only the last year [34]. Without relying on the CMB, they could determine $\Omega_M h^2 = 0.130 \pm 0.010$. Again this is consistent with the CMB data, confirming the need for non-baryonic dark matter.

It is also need to mention a classic strong evidence for dark matter in galaxies. It comes from the study of rotation curves in spiral galaxies. The stars and gas rotate around the center of the galaxy. For example, our solar system rotates in our Milky Way galaxy at the speed of about 220 km/sec. By using Kepler's law, the total mass $M(r)$ within the radius r and the rotation speed at this radius $v(r)$ are related by

$$v(r)^2 = G_N \frac{M(r)}{r} \tag{2.12}$$

Once the galaxy runs out of stars beyond a certain r, the rotation speed is hence expected to decrease as $v(r) \propto r^{-1/2}$. This expectation is not supported by observation.
You can study spiral galaxies which happen to be 'edge-on'. At the outskirts of a galaxy, where you don't find any stars, there is cold neutral hydrogen gas. It turns out you can measure the rotation speed of this cold gas. A hydrogen atom has hyperfine splitting due to the coupling of electron and proton spins, which corresponds to the famous $\lambda = 21$ cm line emission. Even though the gas is cold, it is embedded in the thermal bath of cosmic microwave background whose temperature 2.7 K is hot compared to the hyperfine excitation $hc/k\lambda = 0.069K$. Therefore the hydrogen gas is populated in both hyperfine states and spontaneously emits photons of wavelength 21 cm by the M1 transition. This can be detected by radio telescopes. Because you are looking at the galaxy edge-on, the rotation is either away or towards us, causing Doppler shifts in the 21 cm line. By measuring the amount of Doppler shifts, you can determine the rotation speed. Surprisingly, it was found that the rotation speed stays constant well beyond the region where stars cease to exist.

FIGURE 2.6: 10. Rotation curve of a spiral galaxy [31]

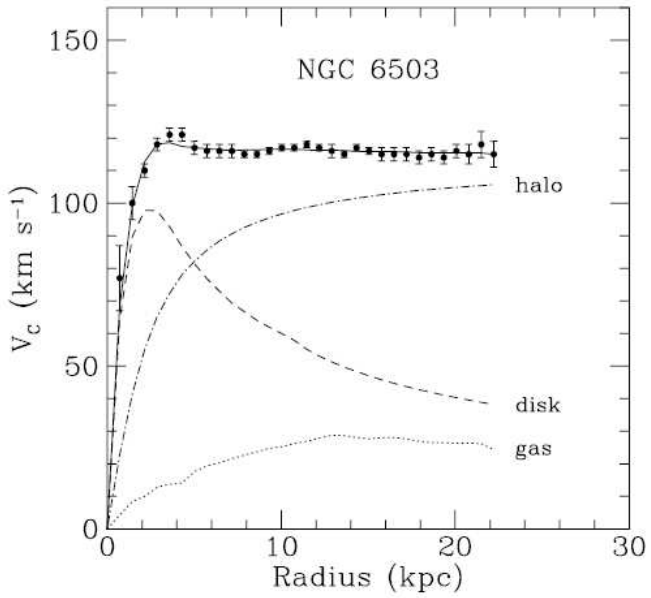

I mentioned this classic evidence because it really shows galaxies are filled with dark matter. This is an important point as we look for signals of dark matter in our own galaxy. It is not easy to determine how much dark matter there is, however, because eventually the hydrogen gas runs out and we do not know how far the flat rotation curve extends. Nonetheless, it shows the galaxy to be made up of a nearly spherical 'halo' of dark matter in which the disk is embedded.

2.5.1 What Dark Matter Is Not

We don't know what dark matter is, but we have learned quite a bit recently what it is not. I have already discussed that it is not ordinary atoms (baryons). I mention a few others of the excluded possibilities.

2.5.1.1 MACHOs

The first candidate for dark matter that comes to mind is some kind of astronomical objects, namely stars or planets, which are is too dark to be seen. People talked about 'Jupiters', 'brown dwarfs' etc. In some sense, that would be the most conservative hypothesis. Because dark matter is not made of ordinary atoms, such astronomical objects cannot be ordinary stars either. But one can still contemplate the possibility that it is some kind of exotic objects, such as black holes. Generically, one refers to MACHOs which stand for MAssive Compact Halo Objects.
Black holes may be formed by some violent epochs in Big Bang (primordial black holes or PBHs) [35] (see also [36]). If the entire horizon collapses into a black hole, which is the biggest mass one can imagine consistent with causality, for example in the course of a strongly first order phase transition, the black hole mass would be

$$M_{PBH} \approx M_{\odot} \left(\frac{T}{100MeV}\right) \left(\frac{g_*}{10.75}\right)^{-1/2} \tag{2.13}$$

Therefore, there is no causal mechanism to produce PBHs much larger than 103 $M_{\odot}$ assuming that universe has been a normal radiation dominated universe for $T <\sim 3$ MeV to be compatible with Big-Bang Nucleosynthesis. Curiously, one finds MPBH $\approx M_{\odot}$ if it formed at the QCD phase transition T $\approx$ 100 MeV [55]. limit from diffuse gamma ray background implies MPBH $> 10^{16} M_{\odot}$. How do we look for such invisible objects? Interestingly, it is not impossible using the gravitational microlensing effects [37]. The idea is simple. You keep monitoring millions of stars in nearby satellite galaxies such as Large Magellanic Cloud (LMC). Meanwhile MACHOs are zooming around in the halo of our galaxy at v $\approx$ 220 km/s. By pure chance, one of them may pass very close along the line of sight towards one of the stars you are monitoring. Then the gravity would focus light around the MACHO, effectively making the MACHO a lens. You typically don't have a resolution to observe distortion of the image or multiple images, but the focusing of light makes the star appear temporarily brighter. This is called microlensing. By looking for such microlensing events, you can infer the amount of MACHOs in our galactic halo.
The bottom line is that you may expect the microlensing event at the rate of

$$rate \approx 5 \cdot 10^{-6} years \left(\frac{M_{\odot}}{M_{MACHOS}}\right)^{1/2} \tag{2.14}$$

towards the LMC, with the duration of

$$duration \approx 6 \cdot 10^{6} sec \left(\frac{M_{MACHOS}}{M_{\odot}}\right)^{1/2} \left(\frac{\sqrt{(d_1 d_2)}}{25kpc}\right) \tag{2.15}$$

where $d1(d2)$ is the distance between the MACHO and us (the lensed star).
Two collaborations, the MACHO collaboration and the EROS collaboration, have looked for microlensing events. The basic conclusion is that MACHOs of mass $10^{-7}30M_{\odot}$ cannot make up 100% of our galactic halo (Fig. 2.7). See also [38,39].

FIGURE 2.7: Limit on the halo fraction f of MACHOs from the EROS collaboration [38]. The spherical isothermal model of halo predicts the optical depth towards the LMC of $\tau = 4.7 \cdot 10^7$. For more details, see the paper.

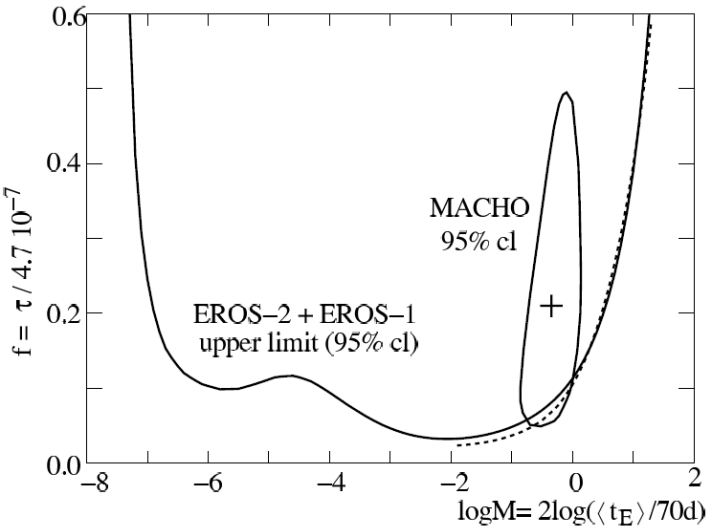

Even though the possibility of MACHO dark matter may not be completely closed, it now appears quite unlikely. The main paradigm for the dark matter of the universe has shifted from MACHOs to WIMPs.

2.5.1.2 Neutrinos

Having discovered neutrinos have finite mass from the oscillation experiments, it is also natural to consider neutrinos to be dark matter candidate. As a matter of fact, neutrinos are a component of dark matter, contributing

$$\Omega_{\nu}h^2 = \frac{\sum_i m_{\nu_i}}{94eV} \tag{2.16}$$

It is an attractive possibility if the particles which we already know to exist could serve as the required non-baryonic dark matter.
However neutrinos are not good candidates for the bulk of dark matter for several reasons. First, there is an upper limit on neutrino mass from laboratory experiments (tritium beta decay) $m < 2eV$ [40]. Combined with the smallness of mass-squared differences $\Delta m^2_{\odot} = 8 \cdot 10^{-5}eV^2 and \Delta m^2_{\oplus} = 2.5 \cdot 10^{-3}eV^2$, electron-volt scale neutrinos should be nearly degenerate. Then the maximum contribution to the matter density is $\Omega_{\nu}h^2 < (3 \cdot 2/94) < 0.064$. This is not enough.
Second, even if the laboratory upper limit on the neutrino mass turned out to be not

correct, there is a famous Tremaine-Gunn argument [41]. For the neutrinos to dominate the halo of dwarf galaxies, you need to pack them so much that you would violate Pauli exclusion principle. To avoid this, you need to make neutrinos quite massive $>\sim 500$ eV so that you dont need so many of them [42]. This obviously contradicts the requirement that $\Omega_\nu < 1$. Third, neutrinos are so light that they are still moving at speed of light (Hot Dark Matter) at the time when the structure started to form, and erase structure at small scales. Detailed study of large scale structure shows such a hot component of dark matter must be quite limited. The precise limit depends on the exact method of analyses. A relatively conservative limit says

$\sum_i m_{\nu_i} < 0.62$ eV [62]

while a more aggressive limit goes down to 0.17 eV [63]. Either way, neutrinos cannot saturate what is needed for non-baryonic dark matter.
In fact, what we want is Cold Dark Matter, which is already non-relativistic and slowly moving at the time of matter-radiation equality T $\sim$ 1 eV. Naively a light (sub-electronvolt) particle would not fit the bill.
A less conservative hypothesis may be to postulate that there is a new heavy neutrino (4^{th} generation). This is a prototype for WIMPs that will be discussed later. It turns out, however, that the direct detection experiments and the abundance do not have a compatible mass range. Namely the neutrinos are too strongly coupled to be the dark matter.

2.6 WIMP Dark Matter

WIMP, or Weakly Interactive Massive Particle, is the main current paradigm for explaining dark matter of the universe. With MACHOs pretty much gone, it is indeed attractive to make a complete shift from astronomical objects as heavy as $M_\odot 10^{57}$ GeV to 'heavy' elementary particles of mass $\sim$ 102 GeV. I will discuss why this mass scale is particularly interesting.

2.6.1 WIMP

The idea of WIMP is very simple. It is a relatively heavy elementary particle so that accelerator experiments so far did not have enough energy to create them, namely $m_\chi >\sim 102$ GeV. On the other hand, the Big Bang did once have enough energy to make them. Let us follow the history from when $T >\sim m_\chi$. WIMPs were created as much as any other particles. Once the temperature dropped below m_χ, even the universe stopped creating them. If they are stable, whatever amount that was produced was there, and the only way to get rid of them was to get them annihilating each other into more mundane particles (e.g., quarks, leptons, gauge bosons). However, the universe expanded and there were fewer and fewer WIMPs in a given volume, and at some point WIMPs stopped finding each other. Then they could not annihilate any more and hence their numbers become fixed ('freezeout'). This way, the universe could still be left with a certain abundance of WIMPs. This mechanism of getting dark matter is called 'thermal relics2.
Under the hypothesis that WIMPS are the main component of the dark matter, these particles should fill the galactic halos and explain the flat rotation curves which are

observed in spiral galaxies. The detection of such particles could be attempted both by means of direct and indirect methods. The direct detection of WIMPs relies on the measurement of their elastic scattering off the target nuclei of a suitable detector [43]. The non relativistic and heavy (GeV - TeV) WIMPs could hit a detector nucleus producing a nuclear recoil of a few keV. Because of the small WIMP-matter interaction cross sections the rate is extremely low. In the case of SUSY WIMPs, most of the cross section predictions encompass a range of values several orders of magnitude (the so-called scatter plots) providing rates ranging from 1 $c/kg/day$ down to $10^{-5} c/kg/day$ according to the particular SUSY model.
It is well known that the predicted signal for the WIMP elastic scattering has an exponentially decaying energy dependence, hardly distinguishable from the background recorded in the detector. The simple comparison of the theoretical WIMP spectrum with the one experimentally obtained, provides an exclusion curve (at a given confidence level), as dark matter component of the halo, of those WIMPs with masses (m) and cross sections on nucleons (σ) which yield spectra above the measured experimental rate. To claim a positive identification of the WIMP, however, a distinctive signature is needed. The only identification signals of the WIMP explored up to now are provided by the features of the Earths motion with respect to the dark matter halo.
In particular, the annual modulation [44] is originated by the combination of the motion of the solar system in the galactic rest frame and the rotation of the Earth around the Sun. Due to this effect, the incoming WIMP velocities in the detector rest frame change continuously during the year, having a maximum in summer and a minimum in winter in the northern hemisphere. Therefore the total WIMP rate changes in time with an oscillating frequency which corresponds to an annual period and a maximum around the beginning of June.
The relative annual variation of the signal is small (a few percent) so in order to detect it one needs large detector masses to increase statistics and several periods of exposure to minimize systematics.

2.7 Double beta decay

Neutrinoless double beta decay $\beta\beta 0\nu$ is a process sensitive to lepton number violation as predicted by gauge theories beyond the standard model and it is expected to give important information on the nature of the nutrinos and the weak interaction.

There has been a growing interest in nuclear double-beta decay in recent years.
This is the process in which an atomic nucleus with Z protons decays to another one with two more (or less) protons and the same mass number A, by emitting two electrons (or positrons) and, usually, other light particles such as neutrinos:

$$(A, Z) + (A, Z + 2) + 2e^{\pm} + anything \tag{2.17}$$

In order to study $\beta\beta$ decay, it is necessary to choose those nuclei in which other decay modes, especially single β decay and electron capture, are energetically forbidden or strongly suppressed by selection rules. There are some thirty even-even nuclei which satisfy this condition for $\beta^-\beta^-$ (electron emitting $\beta\beta$) decay, and several candidate

nuclei for $\beta^+\beta^+$ decay (table below). A typical case of $\beta\beta$ is the decay $^{76}Ge - ^{76}Se$ is illustrated in fig. 8.

FIGURE 2.8: $\beta\beta$ decay of ^{76}Ge. This is expected to take place as successive virtual β transitions via excited states in the intermediate oddcdd nucleus ^{76}As to the ground (0^+) or excited (2^+) state in ^{76}Ge. (Adapted from Ledererand Shirley 1978.)

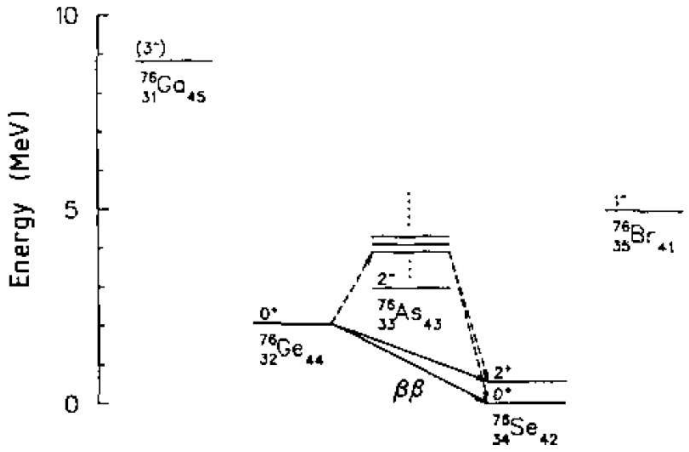

The principal current interest in $\beta\beta$ decay originates in its ability to test the symmetry properties of the standard model of the electroweak interaction (Glashow 1961, Weinberg 1967, Salam 1968) such as lepton number conservation, masslessness of the neutrinos and non-existence of right-handed weak currents. In many gauge theories beyond the standard model, however, none of these symmetries are exact and they are violated to some degree depending on the model. Double beta decay is expected to yield information on the degree of violation and to set important constraints on the models. Double beta decay can be classified into various modes according to the light particles besides the electrons associated with the decay. Independently of the possible violation of the above symmetries, the 2ν (two neutrinos) mode

$$(A, Z) + (A, Z + 2) + 2e^- + 2\bar{\nu}. \tag{2.18}$$

is expected to be observed for those nuclei previously mentioned. This decay mode was considered first by Goeppert-Mayer (1935) shortly after Fermi's theory (1934) of β decay appeared. We note that the neutrino emitted in the process (2.18) is an (electron-)anti-neutrino which is defined as the neutral lepton accompanying the neutron β decay.

$$n \rightarrow p + e^- + \bar{\nu} \tag{2.19}$$

According to our standard knowledge, this particle is different (Davis 1955) from an (electron-)antineutrino which is defined as the particle that causes inverse β decay

$$n + \nu \rightarrow p + e^- \tag{2.20}$$

However, due to the maximal violation of parity in weak interaction (Lee and Yang 1956, Wu el al 1957) it is actually the (almost) opposite helicity of $\bar{\nu}$. with respect to Y that is responsible for the absence of the reaction (2.19) by an incident ν. A more detailed discussion of neutrino properties will be made in the next chapter. [3]

$\beta\beta0\nu$ has been studied in the past by several authors [45, 46, 48, 49, 50]. What is new is the fact that positive observation of neutrino oscillations in atmospheric [53, 54, 55, 56, 57], solar [58, 59, 60, 61], reactor [62, 63] and accelerator [64] neutrinos gives new motivation for more sensitive searches. In fact, recently published constraints on the mixing angles of the neutrino-mixing matrix [21, 22, 23, 24, 25] make a strong case that if neutrinos are Majorana particles, there are many scenarios in which next generation double-beta decay experiments should be able to observe the phenomenon and measure the effective Majorana mass of the electron neutrino, $| < m_\nu > |$, which would provide a measure of the neutrino mass scale m.

2.8 Electron stability

One of the possible tests of fundamental physics is that of charge conservation. This is a QED test, more than a Standad Model test.
In the context of gauge field theories, the invariance of the Lagrangian under a given gauge transformation corresponds to the conservation of some specific type of conserved charge. In some grand unified theories, for example, terms appear in the Lagrangian which break the global gauge invariance associated with baryonic charge leading to proton decay at some level.
In the electroweak sector the gauge invariance of the Lagrangian, corresponding to the equations of quantum electrodynamics, dictates strict electric charge conservation and a massless photon. According to this class of theories we do not expect electrons to decay, because there is no lighter charged lepton, and the decay into photons and/or neutrinos requires the violation of charge conservation. No conservation of the electric charge will only be possible if the Lagrangian of QED contains terms which destroy global as well as local gauge invariance.
Just as proton would decay, among other particles, to a positron and a neutral pion (if the constraint imposed by baryon number conservation is removed), so would the electron decay into a photon and a neutrino (also to a neutrino and neutrino-antineutrino pair) if electric charge conservation is not respected. Such decay of the electron in closed shells of atoms would cause vacancy giving rise to emission of X-rays and Auger electrons.
The most important theoretical consideration is that the search for charge violating decays is in fact a search for such radically *new physics*. In particular, we could consider CV (Charge Violating) effects, in connection with violations of energy-momentum conservation. In fact, charge and momentum are closely related in Kaluza-Klein or superstring models.
There are two possible signatures for the electron decaying : the search for the 255.5 keV γ rays coming from the decay $e^- \rightarrow \gamma + \nu_e$, and looking for the decay $e \rightarrow \nu_e + \nu_e + \overline{\nu_e}$. The latter is the so-called *disappearance* approach and it is used to search for all electron

[3] Since $\beta^+\beta+$ decay is unfavourable because of the Coulomb repulsion of the positrons by the nudeus. we concentrate in this discussion on the electron emitting case.

decay modes, in which the decay particles escape the detector without depositing energy. The best limits for these channels are:

- $\tau > 4.6 \cdot 10^{26}$ yr 90% C.L for CTF Borexino [1].
- $\tau > 3.7 \cdot 10^{24}$ yr 90% C.L for DAMA collaboration [2].

The search for the rare electron decay requires a detector with ultralow background, not to loose the expected weak signal of the expected 255.5 keV -line of the decay in the background radiation.
The described process will be largely discussed in the 6^{th} chapter.

Chapter 3

The Nuclear Matix Elements role

3.1 Introduction

As discussed in the previous chapter, rare physics event is playing a significant role in Fundemental Interaction physics, Particle Physics, Astrophysics and Cosmology.
The experimental achievements accomplished during the last decade in the field of ultra-low background detectors have led to sensitivities capable of searching for such rare events.

Several theoretical speculations point toward a mass generation mechanism that implies a Majorana character of neutrinos, and that indicates the $\beta\beta0\nu$ process as the unique tool with a discovery potential. The CUORE experiment, an array of 988, 750 g TeO_2 bolometers, is one of the best approaches presently available.
The CUORE project originates as a natural extension of the succesfull MiDBD and CUORICINO ^{130}Te experiments, where for the first time large arrays of bolometers were used to search for $\beta\beta0\nu$ - decay. The good results obtained so far proved that the bolometric technique is competitive and alternative to the *traditional* calorimetric Ge technique. The pertinent details of the detectors of the CUORE array and its operation at temperature of $\sim$ 10 mK, as well as the background issues, will be discussed in the next chaper.

3.2 The CUORE physics

As discussed briefly in the previous chapter, the main goal of the CUORE experiment is the observation of neutrinoless double beta decay ($\beta\beta0\nu$).

In the previous chapeter both the allowed (by the Standad Model) mode and the forbidden mode were briefly illustrated, respectively the $\beta\beta2\nu$ and the $\beta\beta0\nu$ decays. The latter one is a process in which the neutrino emitted by a neutron is absorbed by another in the nucleus (neutrinoless mode, fig.ure 3.1 (b)) and violates the lepton number conservation law by two units.

FIGURE 3.1: Two-nucleon mechanism for (a) tw-neutrino and (b) neutrinoless $\beta\beta$ decay as well as (c) neutrinoless $\beta\beta$decay with Majoron emission.

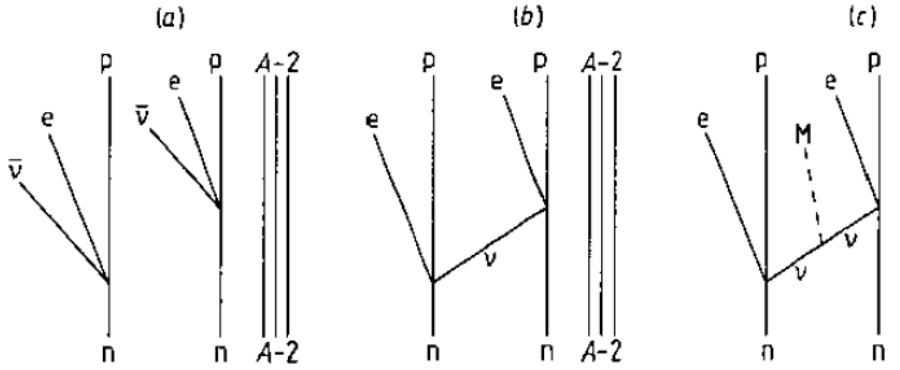

It is clear from the previous argument that the helicity mismatching between the emitted and absorbed neutrinos should be incomplete for this mode to occur. This is realized if

- the neutrino has a **non-vanishing mass**; and/or
- the neutrino together with the electron can form a **right-handed** leptonic charged current and couple weakly to the hadronic current.

In the standard model of the electroweak interactions, the neutrinos are regarded as massless Dirac particles (or more precisely, Weyl particles) with *only left-handed coupling*. This is, however, an *input* rather than a prediction of the model. In order to understand many input assumptions of the standard model which seem to be rather arbitrary, grand unified theories have been developed. In the simplest theory based on the group SU(5) (Georgi and Glashow 1974) the neutrinos are predicted to have the same property as in the standard model. Since B-L (baryon number minus lepton number) is an exact global symmetry of the SU(5) model, the neutrinos cannot have Majorana masses and $\beta\beta0\nu$ decay is forbidden.
In grand unified theories, based on larger groups SO(10), (Georgi 1975, Fritzsch and Minkowski 1975), E(6) (Giirsey el a/ 1976), etc , B-L is a local symmetry and can be broken spontaneously. The neutrinos are predicted to be Majorana particles in order to avoid acquiring masses comparable with those of quarks or charged leptons (Yanagida 1979, Gell-Mann et a1 1979, Witten 1980). These theories predict neutrino masses roughly in the range of $10^{-5} - 1$ eV and also the existence of right-handed currents.
There is also a possibility that B-L is a global symmetry broken spontaneously in the low energy regime (Chikashige el ol 1980, 1981, Gelmini and Roncadelli 1981). In such a case, not only the neutrinos acquire Majorana masses but also a massless Nambu-Goldstone boson appears (called a Majoron). This couples to the Majorana neutrinos and gives rise to a $\beta\beta0\nu$ decay accompanied by Majoron emission $\beta\beta0\nu M$.

$$(A, Z) - (A, Z + 2) + 2e^- + M^0 \tag{3.1}$$

shown in figure 3.1(c) (Georgi et al 1981). In the orginal formulation of this model which includes a Majoron there was the possibility of having even four neutrinos family; in the

most recent models, which account for the results of LEP on the Z^0, there are only 3 neutrino families.
Since the $\beta\beta0\nu$ decay amplitude is proportional to the Majorana neutrino mass or the coupling constants of the right-handed leptonic current, experimental information on 0ν decay is expected to be useful for judging which specific gauge model is correct. In particular for the question whether the neutrino is a Majorana or a Dirac particle, neutrinoless double beta decay is considered to be the most sensitive way of distinguishing between these two possibilities.
For a reliable deduction of the neutrino mass or right-handed current admixtures from experimental data, it is necessary to examine critically various approximations, both in the derivation of the *transition operators* and in their evaluation using *specific nuclear models*.
The description of the several nuclear models nowadays in use will be performed later in this chapter.
Experimental methods for detecting $\beta\beta$ decay fall into three categories:

- direct detection of electron or positron pairs associated with $\beta\beta$ decay;
- geochemical measurement of the amount of daughter nuclei accumulated in a geologically old ore; and
- radiochemical measurement of the amount of daughter nuclei accumulated under laboratory conditions.

Kinematic data on the electrons or positrons obtained by the first method provide information on the mechanisms of $\beta\beta$ decay. With the sum energy spectrum of electrons, one can distinguish among various modes ($\beta\beta0\nu$, $\beta\beta2\nu$, $\beta\beta0\nu M$ etc). With the single-electron energy spectrum and the angular correlation of two electrons one can distinguish (see figure 18 in section 5.1) between $\beta\beta0\nu$ decays due to a finite Majorana mass and the right-handed leptonic current, and in the latter case, between decays due to its coupling to the left-handed and right-handed hadronic currents. Clearly one can only determine the total $\beta\beta$ decay rate by the second and the third methods.

Since the first attempt by Fireman (1948), strenuous efforts have been made by many experimentalists to observe $\beta\beta$ decay. Reflecting the long history and the importance of the field, many review articles have been published which partly or extensively deal with $\beta\beta$ decay (Primakoff and Rosen 1959, 1981, Fiorini 1972, Bryman and Picciotto 1978, Zdesenko 1980, Kirsten 1983, Boehm and Vogel 1984, Haxton and Stephenson 1984, Doi el al 1985, Vergados 1986, Avignone and Brodzinski 1988, Caldwell 1988, Faessler 1988, Lazarenko 1966, Muto and Klapdor 1988b).

3.3 Majorana neutrinos

In this section the basic properties of Majorana neutrinos and their relation to Dirac and pseudo Dirac neutrinos are summarized.

FIGURE 3.2: (a) Single-electron Spectrum for $\beta\beta$ decay of ^{82}Se. The full curve was calculated by integration except ϵ_1 in (3.28) and normalized to the central value of the experimental 2ν half-life (Elliott el D I 1987a) $1.1 \cdot 10^{20}$ y. The broken curve shows the result of an analogous calculation using (3.94) for $\beta\beta 0\nu$ decay with Majoron emission with a normalization to the experimental bound (Moe et ai 1988) $\tau_{1/2}^{0\nu M}$ y and magnified by a factor 10. (b) Sum energy spectra of the two emitted electrons for $\beta\beta 2\nu$, $0\nu\beta\beta M$ and $\beta\beta 0\nu$ decay of ^{82}Se. The differential rates dW/dT_{sum} with $T_{sum} = \epsilon_1\epsilon_2 - 2m_ec^2$ for the first two modes were calculated analogously to (G). The vertical line at $Q_{\beta\beta} = 2.995$ MeV indicates the position of an expected peak for $\beta\beta 0\nu$ decay

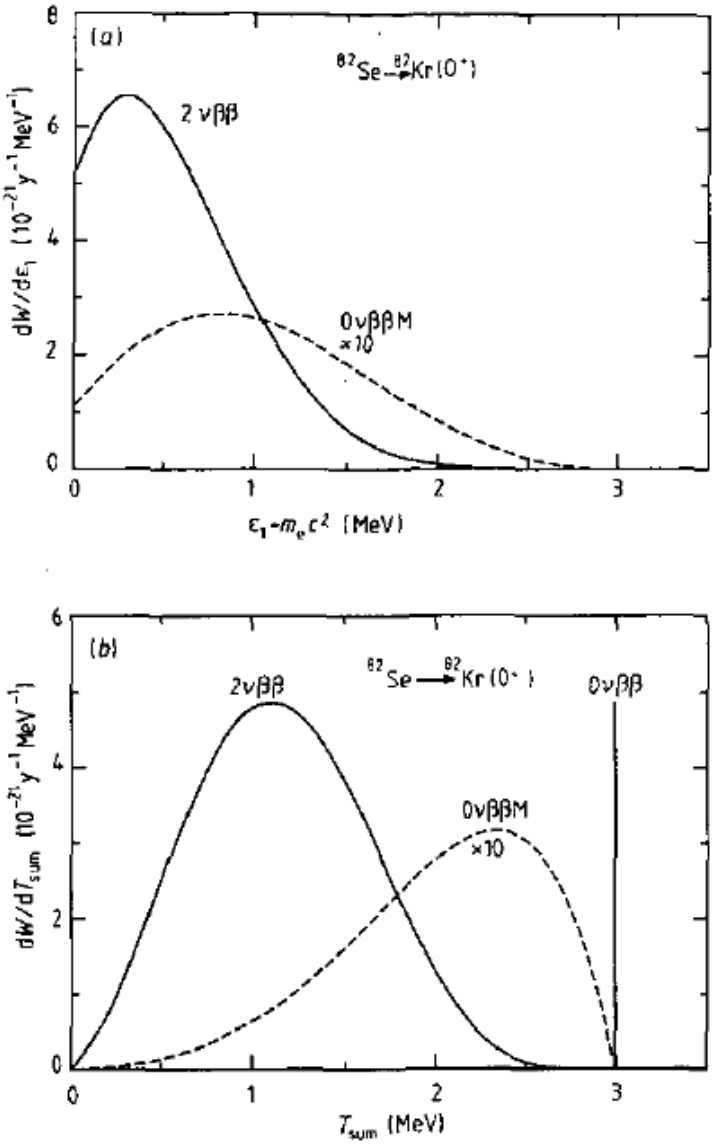

3.3.1 Majorana neutrinos and their CP properties

Let us assume that there are n generations of charged leptons as well as left- and right-handed neutrinos:

$$l = \begin{pmatrix} e \\ \mu \\ \tau \\ . \\ . \end{pmatrix} \nu_l = \begin{pmatrix} \nu_e \\ \nu_\mu \\ \nu_\tau \\ . \\ . \end{pmatrix} \nu_R^{'} = \begin{pmatrix} \nu_{eR}^{'} \\ \nu_{\mu R}^{'} \\ \nu_{\tau R}^{'} \\ . \\ . \end{pmatrix} \tag{3.2}$$

and that their charged current weak interaction is given by

$$L_{cc}(x) = \frac{g}{2\sqrt{2}}[\bar{l}\gamma^\mu(1-\gamma^5)\nu_L W_{L\mu}^- + \bar{l}\gamma^\mu(1+\gamma^5)\nu_L W_{R\mu}^-] + HC \tag{3.3}$$

where $W_{L\mu}^-$ and $W_{R\mu}^-$ are the gauge boson fields which mediate left- and right-handed interactions. We assume that the $n \times n$ mass matrix for the charged leptons has already been diagonalized. Choosing the phases of the charged lepton fields appropriately, and assuming CP invariance of the Lagrangian we obtain the uniform CP transformation property for all the components of ν_L and ν_R. The most general mass term for the neutrinos has the form

$$L_m(x) = -\frac{1}{2}((\bar{\nu_L^c})\bar{\nu_R^{'}})\mathbf{M}^0 + \begin{pmatrix} \nu_L \\ (\nu_{\mu R}^{'})^c \end{pmatrix} + HC \tag{3.4}$$

with the $2n \times 2n$ mass matrix $\mathbf{M}^0$ which can be assumed to be symmetric without loss of generality

$$\mathbf{M}_0 = \begin{pmatrix} \mathbf{M}_L^0 & \mathbf{M}_D^{0\,\mathbf{T}} \\ \mathbf{M}_D^0 & \mathbf{M}_R^0 \end{pmatrix} \tag{3.5}$$

Here the $n \times n$ submatrix $\mathbf{M}_k$ gives Dirac mass terms which conserve lepton number, whereas $\mathbf{M}_L^0$ and $\mathbf{M}_R^0$ are responsible for Majorana mass terms which violate lepton number conservation. Assuming CP invariance also for $L_m(x)$, we obtain $\mathbf{M}^{0\dagger} = \mathbf{M}^0$ from (3.4). Together with$\mathbf{M}^{0T} = \mathbf{M}^0$, it means that $\mathbf{M}^0$ is a real symmetric matrix. We can diagonalize $\mathbf{M}^0$with a real orthogonal matrix $\mathbf{O}_\nu$,

$$\mathbf{M}^0 = \mathbf{O}_\nu^T \mathbf{M} \mathbf{S} \mathbf{O}_\nu \tag{3.6}$$

where $M_{jk} = \delta_{jk} m_j$, $S_{jk} = \delta_{jk} S_j$ with $m_j > 0$ and $S_j = \pm 1$. The Lagrangian L_m now takes the form

$$L_m = -\frac{1}{2}\bar{N}\mathbf{M}N \tag{3.7}$$

with the Majorana neutrino field N given by

$$N = \Lambda \left[\mathbf{O}_\nu \begin{pmatrix} \nu_L \\ \nu_R^{'c} \end{pmatrix} + \mathbf{SO}_\nu \begin{pmatrix} (\nu_L)^c \\ \nu_R^{'} \end{pmatrix} \right] \tag{3.8}$$

where Λ is a diagonal matrix of arbitrary phases $\Lambda_k = \delta_{jk}\lambda_j$, $|\lambda_j| = 1$. The N field satisfies the majorana condition, i.e., it is identical to his charge-coniugate field, up to a phase. The field N_j can he expanded in terms of plane wave solutions of the Dirac equation.
The current neutrinos ν_L and $\nu_R^{'}$ appearing in L_{cc},, are related to the Majoranan neutrino N by:

$$\nu_L = \mathbf{U}N_L \qquad \nu_R^{'} = \mathbf{V}N_R \tag{3.9}$$

where $N_{L,R} = P_{L,R}N$

Previously we assumed only CP invariance so that the mass matrix was a general real symmetric matrix. Now let us turn to a few special cases.
If $\mathbf{M}_L = \mathbf{M}_L = 0$ the mass matrix becomes antidiagonal

$$\mathbf{M}^0 = \begin{pmatrix} 0 & \mathbf{M}_D^{0\,T} \\ \mathbf{M}_D^0 & 0 \end{pmatrix} \tag{3.10}$$

and we have the so called the Dirac and pseudo Dirac neutrinos, i.e., we have obtained pairwise degenerate Majorana neutrinos with opposite CP parity. We can introduce a field which is a linear combination of the degenerate Majorana neutrinos N_I and N_{II}

$$\psi = \frac{1}{\sqrt{2}}(\Lambda_I^* N_I + \Lambda_{II}^* N_{II}) \tag{3.11}$$

With this field we can write the lagrangian:

$$L_m = -\bar{\psi}\mathbf{M}_I\psi \tag{3.12}$$

We see this field ψ represents a Dirac neutrino with mass m_j and that it is formed from two degenerate Majorana neutrinos with opposite CP parity. The contributions from these two Majorana neutrinos cancel each other exactly in the propagator of the lepton number violating type. i.e. the *total lepton number is conserved*.
A Dirac neutrino can also he formed by a combination of ν_L and $(\nu_L)^c$, instead of ν_L and $\nu_R^{'}$ (Konopinski and Mahmoud 1953).
A pair of Majorana neutrinos with opposite CP parity is called a *pseudo Dirac* neutrino when their masses are approximately but *not* exactly degenerate (Wolfenstein 1981a, Petcov 1982, Valle 1983, Doi et al 1983b). In this case their contribution to the lepton-violating number propagator is non-vanishing hut strongly suppressed..

3.3.2 The seesaw mechanism

For simplicity let us consider the one-generation case in which $\mathbf{M}^0$ is assumed to be given by

$$\mathbf{M}^0 = \begin{pmatrix} 0 & m_D \\ m_D & m_R \end{pmatrix} \tag{3.13}$$

with $m_R \gg m_D$. This $\mathbf{M}^0$ can be diagonalized with

$$\mathbf{O}_\nu = \begin{pmatrix} cos\theta & -sin\theta \\ sin\theta & cos\theta \end{pmatrix} \qquad \frac{1}{2}tan2\theta = \frac{m_D}{m_R} \tag{3.14}$$

yielding

$$\mathbf{M} \approx \begin{pmatrix} (\frac{m_D^2}{m_R}) & 0 \\ 0 & m_R + (\frac{m_D^2}{m_R}) \end{pmatrix} \qquad \mathbf{S} = \begin{pmatrix} -1 & 0 \\ 0 & 1 \end{pmatrix} \tag{3.15}$$

The current neutrinos are expressed in terms of mass eigenstate neutrinos as

$$\nu_L = \lambda_1^* cos\theta N_{1L} + \lambda_2^* sin\theta N_{2L} \qquad \nu_R^{'} = \lambda_1^* cos\theta N_{1R} + \lambda_2^* sin\theta N_{2R} \tag{3.16}$$

In left-right symmetric grand unified theories such as those based on the group representations SO(10), the neutrinos are treated on the same footing as other fermions. Consequently under minimal assumptions, a neutrino would acquire a Dirac mass of the same order as those of other fermions, which clearly contradicts the experimental limits on the neutrino masses.

A mass matrix of the type (3.10) was introduced as a remedy for such a situation. The left-handed neutrino ν_L of equation (3.16) consists mainly of the Majorana neutrino N_1 with mass $m_1 \approx m_L/m_R$. As m_R becomes larger, m_L becomes correspondingly smaller (called a seesaw mechanism, Yanagida 1979, Gell-Mahn et a/ 1979). One would get m_L - 1 eV for $m_D \sim 1 - 10^3$ MeV and $m_R \sim 10^3 - 10^9$ GeV.
Actually more recent models contemplate lighter m_R ($\sim keV$).

3.4 Theoretical description of $\beta\beta$ decay

3.4.1 The effective Hamiltonian

In the previous section we assumed the charged current interaction for leptons of the form (3.3). The relevant part for decay can he written as :

$$L_{cc}(x) = \frac{g}{2\sqrt{2}}[j_L^\mu W_{L\mu}^- + j_R^\mu W_{R\mu}^-] + HC \tag{3.17}$$

where the left- and right-handed leptonic currents are given by

$$j_L^\mu = \bar{e}\gamma^\mu(1-\gamma^5)\nu_{eL} \qquad j_R^\mu = \bar{e}\gamma^\mu(1+\gamma^5)\nu_{eR} \tag{3.18}$$

with the electron field e and the current electron-neutrino fields

$$\nu_{eL} = \sum_{i=1}^{2n} U_{ei} N_{iL} \qquad \nu_{eR} = \sum_{i=1}^{2n} U_{ei} N_{iR} \tag{3.19}$$

Here N_i is a Majorana neutrino field with mass m_i. One should remember that a Dirac neutrino can also be expressed as a superposition of Majorana neutrinos. In the following we adopt one particular convention for the choice of the arbitrary phases λ_i,whihc is (Schechter and Valle 1980, Doi et a1 1981a)

$$\mathbf{\Lambda}^2\mathbf{S} = 1 \qquad \lambda_i = \begin{array}{ll} 1 & S_i = 1 \\ i & S_i = -1 \end{array} \tag{3.20}$$

The gauge bosons W_L and W_R are related to the mass eigenstates W_1 and W_2, (with masses M_1 and M_2) by

$$\begin{pmatrix} W_L^- \\ W_R^- \end{pmatrix} = \begin{pmatrix} cos\zeta & sin\zeta \\ -sin\zeta & cos\zeta \end{pmatrix} \begin{pmatrix} W_1^- \\ W_2^- \end{pmatrix} \tag{3.21}$$

and in general $\zeta \neq 0$. Adding left- and right-handed nuclear currents $J^\mu_{L,R} cos\theta_c$ the leptonic counterparts $J^\mu_{L,R}$ in (3.17), where θ_c is the Cabibbo-Kobayashi-Maskawa angle, we can write the effective weak interaction Hamiltonian for decay due to W boson exchange in the form (Bhg *et a*l 1977, Doi *et al* 1983a)

$$H_W = (Gcos\theta_c\sqrt{2})(j_{L,\mu}J_L^{\mu\dagger} + \kappa j_{L,\mu}J_R^{\mu\dagger} + \eta j_{R,\mu}J_L^{\mu\dagger} + \lambda j_{R,\mu}J_R^{\mu\dagger}) \tag{3.22}$$

We regard the coupling constants κ, η and λ as small parameters (≤ 1). Assuming that the nucleons in a nucleus behave in the same way as free nucleons (*impulse approximation*), we write the nuclear currents in terms of a nucleon field $\psi = \begin{pmatrix} p \\ n \end{pmatrix}$ as

$$\begin{aligned} J_L^{\mu\dagger} &= \bar{\psi}(x)\tau^+(g_V\gamma^\mu - ig_W\sigma^{\mu\nu}q_\nu - g_A\gamma^\mu\gamma^5 + g_P\gamma^5 + g_P\gamma^5 q^\mu)\psi(x) \\ J_R^{\mu\dagger} &= \bar{\psi}(x)\tau^+(g_V\gamma^\mu - ig_W\sigma^{\mu\nu}q_\nu - g_A\gamma^\mu\gamma^5 + g_P\gamma^5 - g_P\gamma^5 q^\mu)\psi(x) \end{aligned} \tag{3.23}$$

where $\tau^+ = \frac{1}{2}(\tau_1 + i\tau_2)$ converts a neutron into a proton, $q_\mu = p_\mu - p'_\mu = \partial_\mu - \partial'_\mu$ is the 4-momentum transfer, and g_V, g_A, g_W and g_P are the vector, axial vector, weak magnetism and pseudoscalar form factors (see e.g. Commins and Bucksbaum 1983). The first two of these at $q^2 = 0$ are

$$\begin{aligned} g_V(0) &= 1 \\ g_A(0) &= 1.254 \end{aligned} \tag{3.24}$$

Later in this chapter I will focus on th fact the second form factor has not a universal value for all the nuclear models nowadays in use; this fact leads to some difficulties in the comparison between all the result on Nuclear Matrix Element (NME) for the neutrinoless double beta decay and thus to the use of the quantitity $F_N \cdot |M^{0\nu}|^2$ as a factor of merit for the By the Foldy-Wouthuysen transformation (1950), the nuclear currents (3.23) are reduced to the nou-relativistic form (Rose and Osborn 1954, Riar 1966):

$$J_L^{\mu\dagger} = \sum_{n=1}^{A} \tau_n^+ \delta(x - r_n) \sum_{k=0,1..} [g_V V^{(k)\mu} + g_W W^{(k)\mu} - g_A A^{(k)\mu} - g_P P^{(k)\mu}]_n \tag{3.25}$$

For $J_R^{\mu\dagger}$ the expression is almost the same, save for the sign of g_A and g_P.

where k indicates the order in $1/M$. The terms of the order $1/M^2$ are here omitted, for semplicity.
The momenta p_n and $p_n^{'}$ should be interpreted as $-i\partial/\partial_{\mathbf{r}_n}$, standing to the right and left, respectively, of $\delta(\mathbf{x}-\mathbf{r}_n)$ in equation (3.25). It follows in the case of small energy transfer $|q_n^0| \ll \Lambda$ that

$$\delta(\mathbf{x}-\mathbf{r}_n) g_V(q^2) \approx \frac{\Lambda^3}{8\pi} e^{-|\mathbf{x}-\mathbf{r}_n|} \tag{3.26}$$

and so on. The length Λ^{-1} represents the finite extension of the nucleon.
The momentum transfer q at a weak interaction vertex is equal to the sum of the momenta of the electron and the neutrino leaving the vertex. In In the case of $\beta\beta2\nu$ decay the momenta of both the electrons and neutrinos are restricted by the Q-value, and they are typically of the order of 1 MeV. Consequently one has to take into account only the leading terms $V^{(0)0} = 1$ and $A^{(0)} = \sigma$.
In the case of $\beta\beta0\nu$ decay, however, the neutrino emitted by one nucleon is absorbed by another. Its typical momentum p is estimated to be of order $\sim 1/\mathbf{r}_{NN} \sim 100$ MeV, where $\mathbf{r}_{NN} - 2$ fm is the mean internucleon distance, so that the recoil terms in (3.12) become much larger than in the case of single β or $\beta\beta2\nu$ decay. Substituting the estimates

$$\begin{aligned} &|q| \sim |\mathbf{Q}| \sim \bar{p} \sim 100 MeV \\ &|q|^0 \sim \bar{E} \sim p^2/2M \sim 10 MeV \\ &|\sigma| \sim 1 \\ &g_A \sim 1 \end{aligned} \tag{3.27}$$

into the various terms of equation (3.25) we can obtain the estimates for all the form factors.
The recoil terms of order q/M or Q/M compared to the leading terms $V^{(0)0} = 1$ and $A(0) = \sigma$, these terms have a different property under parity transformation, and consequently they enter into $\beta\beta0\nu$ decay amplitudes in a different manner.
These terms lead to corrections to the decay amplituted not negligible sometimes: for example a particular recoil term (usually called the **D** term, $\sim [\mathbf{p}_n + \mathbf{p}_n^{'} - i\mu_\beta \sigma_n \times (\mathbf{p}_n - \mathbf{p}_n^{'})]/2M$, not simply gives a correction of about 25% to the decay amplitudes, but it gives the *dominant* contribution to the $0^+ \to 0^+ \beta\beta0\nu$ decay due to the interaction proportional to η in (3.22), which represents the coupling of the right-handed leptonic current to the left-handed nuclear current. The finite extension of the nucleon represented by the q^2 dependence of the form factors will also be neglected unless the effective two nucleon transition operators for $\beta\beta0\nu$ decay become short-ranged: the details for the **SRC** (Short Range Correlations) will be discussed later in this chapter.

3.5 $\beta\beta2\nu$ decay

Here I briefly summarize what this decay is, for completeness of the discussion.
The $\beta\beta2\nu$ decay is as a second-order process in the effective weak interaction (3.22). Since those processes which involve only left-handed currents clearly give the dominant contribution, it is possible neglect right-handed currents in the case of $\beta\beta2\nu$ decay.
The differential decay rate $dW_{2\nu}$ accounts for the presence in the final state of two electrons and two neutrinos. In particular, there are not unknown parameters in the leptonic current. The $\beta\beta2\nu$ decay can be considered as a test for the veridivcity of

the current nuclear models. Using the perturbation theory, at the second order in the hamiltonian, to have the matrix element T_{fi}, which connects the initial and final states f, i we have:

$$(2\pi)^4\delta^4(\mathbf{p}_f - \mathbf{p_i})T_{fi} = - < f|\int \mathbf{H}_\beta \, d^4x|i > + \frac{i}{2} < f|\int T[\mathbf{H}_\beta(\mathbf{x}'), \mathbf{H}_\beta(\mathbf{x}'')]d^4x' d^4x''|i > \tag{3.28}$$

where the T-product accounts for the non linear terms.
The summation $\sum_{spin}$ is taken over the spin projections of the electrons, the neutrinos and the final nuclear state, and taken over those light neutrino species the emission of which is kinematically allowed. We assume in the following that the masses of these light neutrinos are all much smaller than the Q-value of the $\beta\beta$ decay:

$$Q_{\beta\beta} = E_i - E_f - 2m_e$$

We expand the electron and neutrino wavefunctions in terms of the solutions of the Dirac equation in spherical coordinates and consider only S-wave states for the *four* emitted leptons since they have by far the largest amplitudes near the nuclear surface. The radial wavefunctions are then expanded in powers of r and the leading constant terms are retained (Doi *et al* 1983a). The error in such an approximation is - $\sim (p_{eff}R)^2$ and can safely he neglected, where R is the nuclear radius and p_{eff} the 'effective' momentum of the leptons at the nuclear surface ($p_{eff} - 3Z\alpha/2R$ for electrons and $p_{eff} = k - 1$ MeV for neutrinos). The total angular momentum of four S-wave leptons can be 0, 1 or 2, and is on the other hand equal to the angular momentum transfer from the nucleus. Therefore both $0^+ \to 0^+$ and $0^+ \to 2^+$ decays of practical interestt can be treated under the present assumptions.
For the nuclear current J_L we take into account only the dominant terms $V^{(0)0} = 1$ and $A^{(0)} = 0$ (see previous section). Combined with the assumption of S-wave leptons, they yield operators which describe virtual Fermi or Gamow-Teller transitions. Since the isospin of the final nuclear state differs from that of the initial nucleus by two for any $\beta\beta$ decay of practical interest, the contribution of successive Fermi transitions, which comes only from isospin mixing effect, can be safely neglected.
Regarding the channel $0^+ \to 0^+$ The differential rate is given by (Primakoff and Rosen 1959, Konopinski 1966, Doi el a/ 1981b, 1983a, Haxton el a/ 1982a):

$$\omega_{2\nu} = \frac{g_A G cos\theta_c}{64\pi^7}\omega_1^2\omega_2^2 p_1 p_2 \epsilon_1 \epsilon_2 \delta(\epsilon_1 + \epsilon_2 + \omega_1 + \omega_2 + E_F - E_I)$$

Since the typical nuclear excitation energy $E_N - E_I$ (~ 10 MeV) due to the Gamow-Teller operator $\tau^+\sigma$ is usually much larger than the lepton energies (~ 1 MeV), the intermediate energies can be replaced with the average energy $< E_N >$ in the calculation, leading to the expression for the half-life in the factorized form (Doi et a/ 1985):

$$[\tau_{1/2}^{2\nu}(0^+ \to 0^+)]^{-1} = \frac{W_{2\nu}}{ln2} \approx F_{2\nu}|M_{2\nu}|^2 \tag{3.29}$$

where $M_{2\nu}$ is the nuclear transition amplitude and $F_{2\nu}$ the lepton phase space integral. $F_{2\nu}$ is not very sensitive to the choice of the actual value of $< E_N >$.
If E_N is replaced by the average value, the summation over the intermediate nuclear

states can be completed to give (Primakoff and Rosen 1959)

$$M_{2\nu} \sim \frac{2M_{GT}^{2\nu}}{1/2W_0 + < E_N > - E_I} \qquad M_{GT}^{2\nu} = < \sigma_{\mathbf{1}} \cdot \sigma_{\mathbf{1}} > \tag{3.30}$$

This closure approximation has been used frequently in the literature. In practice it is rather difficult to estimate E_N correctly without precise knowledge about the value of $M_{2\nu}$, which is just the quantity to be calculated.

3.6 $\beta\beta 0\nu$

Since the first formulation by Furry (1939), the theory of $\beta\beta 0\nu$ decay has been developed (Primakoff and Rosen 1959, Molina and Pascual 1977, Doi el al 1981c, 1983a, Haxton and Stephenson 1984, Tomoda *et al.* 01 1986) in accordance with the progress in our understanding of the weak interaction.
Here we follow mainly the notation adopted by Tomoda *et al* (1986). First we rewrite the Hamiltonian density into the following form:

$$H_W = (Gcos\theta_c/\sqrt{2}) \sum_{i=1}^{2n} [j_{Li\mu} J_{Li}^{\mu\dagger} + \lambda_{Ri\mu} J_{Ri}^{\mu\dagger}] + HC \tag{3.31}$$

where $J_{L,Ri}$ are the left- and right-handed leptonic currents formed out of the electron and mass eigenstate neutrino fields e and N_i

$$j_{L,Ri\mu} = \bar{e}\gamma^{\mu}(1 \mp \gamma^5) N_{iL,R} \tag{3.32}$$

and $J_{L,Ri}^{\mu\dagger}$ are the nuclear currents coupled to these leptonic currents:

$$\begin{aligned} J_{L,i}^{\mu\dagger} &= U_{e,i}(J_L^{\mu\dagger} + \kappa J_R^{\mu\dagger}) \\ J_{r,i}^{\mu\dagger} &= V_{e,i}(\lambda J_R^{\mu\dagger} + \eta J_L^{\mu\dagger}) \end{aligned} \tag{3.33}$$

The term $\kappa J_R^{\mu\dagger}$ will be neglected in the following since κ enters into $\beta\beta$ decay amplitudes always in the combination $1 \pm \kappa$ and we expect $\kappa \ll 1$. The differential $\beta\beta 0\nu$ decay rate is given by:

$$dW_{0\nu} = 2\pi \sum_{spin} |R_{0\nu}|^2 \delta(\epsilon_1 + \epsilon_2 + E_F - E_I) \frac{d\mathbf{p_1}}{2\pi^3} \frac{d\mathbf{p_2}}{2\pi^3} \tag{3.34}$$

where $R_{0\nu}$ is a factor wich contains the summation $\sum_{spin}$ which is taken over the spin projections of the electrons $s_1^{'} s_2^{'}$ and the final nuclear state.
The summation in the factor $R_{0\nu}$ neutrino spin yields to :

$$P_{\beta}(\omega\gamma^0 - \kappa \cdot \gamma + m_i) P_{\alpha} = \begin{array}{ll} m_i P_{\alpha} & \alpha = \beta \\ (\omega\gamma^0 - \kappa \cdot \gamma) P_{\alpha} & \alpha \neq \beta \end{array} \tag{3.35}$$

where $P_{\alpha,\beta}$ is the projection operator.
This equation shows that the $\beta\beta 0\nu$ decay amplitude contains a factor proportional to

- the neutrino mass for the processes involving only the left- or right-handed leptonic current ($(\alpha\beta) = (LL)$ or (RR))
- the neutrino energy or momentum for those involving both the left- and right-handed leptonic currents ($(\alpha\beta) = (LR)$ or (RL)).

The contribution from the processes exclusively due to the right-handed leptonic current ($(\alpha\beta) = (RR)$ will be neglected in the following since it is of second order in the small coupling constants λ and η.
In contrast to the case of $\beta\beta0\nu$ decay, the neutrinos in $\beta\beta0\nu$ decay are virtual particles exchanged between nucleons and their typical energy is much larger than the typical excitation energy of the intermediate nuclear states ($\omega \sim 10MeV$).
Replacing E_N by an 'average'F $< E_N >$, and using the closure relation $\sum_N |N >< N| = 1$, we can complete the summation over the intermediate nuclear states.
For the electron wavefunctions for the first approximation is enough to consider the $S_{1/2}$ and $P_{1/2}$ wavefunction for $0^+ \to 0^+$ and the nuclear recoil term.

3.6.0.1 $0^+ \to 0^+$ channel

I will discuss only the decay to the ground state, even if there are several mechanisms trough wihch the decay can happen (involving Higgs bosons, heavy neutrinos, right handed currents...etc.).
The differential rate for this channel decay with the energy of the *first* electron ϵ_1 and the angle between the two emitted electrons $\theta_{1,2}$ is given by (Doi *el al* 1983a, Tomoda et nl 1986)

$$\frac{d^2\omega_{0\nu}}{d\epsilon_1 dcos\theta_{1,2}} = (a^{(0)} + a^{(1)}cos\theta_{1,2})\omega_{0\nu} \tag{3.36}$$

where

$$\omega_{0\nu}$$

where

$$\begin{aligned} \omega_{0\nu} &= \frac{(g_A G cos\theta_C)^4 m_e^5}{16\pi^5} p_1 p_2 \epsilon_1 \epsilon_2 \\ \epsilon_1 + \epsilon_2 + E_F &= E_I \\ a^{(i)} &= \sum_{j,k=1}^{6} f_{j,k}^{(i)} Re[X_j X_K^*] \qquad\qquad i = 0, 1 \end{aligned} \tag{3.37}$$

The phase-space factors $f_{j,k}^{(i)}$ are the products of electron radial wavefunctions and X_i are the combinations of nuclear matrix elements:

$$\begin{aligned} X_1 &= \left(\frac{< m_\nu >}{m_e}\right)(X_F - 1)M_{GT}^{(0\nu)} \\ X_3 &= (\lambda\grave{\chi}_- - \eta\grave{\chi})\, M_{GT}^{(0\nu)} \\ X_4 &= \left(\lambda\chi_-^{'} - \eta\chi_+^{'}\right) M_{GT}^{(0\nu)} \\ X_5 &=< \eta > \chi_P^{'} M_{GT}^{(0\nu)} \\ X_6 &=< \eta > \chi_R^{'} M_{GT}^{(0\nu)} \end{aligned} \tag{3.38}$$

with

$$\begin{aligned} < m_\nu > &= \sum_i m_i U_{ei}^2 \\ < \lambda > &= \lambda \sum_i U_{ei} V_{ei} \\ < \eta > &= \eta \sum_i U_{ei} V_{ei} \end{aligned} \tag{3.39}$$

The other X_i represents different contribution to the amplitude (like, for example, X_2 is the contribution from right handed leptonic current and can be here neglected).
The summation in equation (3.37) should be taken over those light neutrinos ($m_i \ll 100$ MeV) for which the approximation $\omega \sim |k|$ holds. Since for heavier neutrinos the dependence of the propagation functions $H(r)$ etc on the mass m_i cannot be neglected, it is impossible to factor out these from the summation over neutrino species in equation.
We assume *CP* invariance so that λ and η and are real. Then are also $< m_\nu >$, $< \lambda >$ and $< \eta >$ real since U_{ei} and V_{ei} ' are both real or both pure imaginary depending on the *CP* parity of the mass-eigenstate neutrino N_i.

If all the neutrinos are massless, we clearly have $< m_\nu >= 0$ and also $< \lambda >=< \eta >= 0$, so that there will he no $\beta\beta 0\nu$ decay, regardless which mechanism we assume.

It should be also noticed, however, that even if $m_i \neq 0$ for any i, the effective electron-neutrino mass m_ν can be much smaller than any m_i when the contributions of neutrinos with opposite CP parity cancel each other. On the other hand, if $< \lambda >\neq 0$ and/or $< \eta >\neq 0$, there will be a finite probability for $\beta\beta 0\nu$ decay, and this in turn induces a finite mass $< m_\nu >$ even if $< m_\nu >= 0$ at a tree level (Schechter and Valle 1982, Nieves 1984, Takasugi 1984).
However, since the 0ν decay rate can still be expressed in terms of $< m_\nu >$, $< \lambda >$ and $< \eta >$ we consider these as independent parameters in the following.

For the specific expression of nuclear matrixelements χ, see TomodaRP54. Insofar as we restrict ourselves to the case where at least one of the electrons is emitted in an $S_{1/2}$ wave, there is no contribution which is first-order in the other recoil term to $O^+ \to O^+$ decay, under the present assumption of the closure approximation. Integrating th equation 3.37 in ϵ_1 and $cos\theta_{12}$ we obtain:

$$\begin{aligned}
&\frac{dW_{0\nu}}{cos\theta_{12}} = \frac{ln2}{2}(A^{(0)} + A^{(1)}cos\theta_{12}) \\
&A^{(i)} = \frac{2}{ln2}\int a^i \omega_{0\nu} d\epsilon_1 \\
&\tau^{0\nu}_{1/2}(0^+ \to 0^+)^{-1} = \frac{W_{0\nu}}{ln2} = A^{(0)}
\end{aligned} \tag{3.40}$$

Rearranging the $a^{()}$ with respect to $< m_\nu >$, λ and η we obtain:

$$\begin{aligned}
A^{(i)} &= C^{(i)}_{mm}(\frac{< m_\nu >}{m_e})^2 + C^{(i)}_{\lambda\lambda} < \lambda >^2 \\
&+ C^{(i)}_{\eta\eta} < \eta >^2 + 2C^{(i)}_{m\lambda}(\frac{< m_\nu >}{m_e}) < \lambda > \\
&+ 2C^{(i)}_{m\eta}(\frac{< m_\nu >}{m_e}) < \eta > + 2C_{\lambda\eta} < \lambda >< \eta >
\end{aligned} \tag{3.41}$$

where $i = 0, 1$. $C^{(i)}_{mm}$ is for example, $(M^{(0\nu)}_{GT})^2 F^i_{11}(X_F - 1)^2$, with $F^i_{jk}\frac{2}{ln2} = \int f^i_{jk}\omega_{0\nu}d\epsilon_1$ are the phase space factors which will be discussed later in this chapter.

3.7 Nuclear structure calculations: Nuclear Matrix Elemnts-NME-

This section deals with the formal aspects of nuclear structure calculations for the $\beta\beta0\nu$ transition matrix elements.

3.7.1 Closure Approximation

The closure approximation was used frequently in the literature. It facilitates numerical calculcations considerably since in this approximation one needs only the wavefunctions of the initial and final nuclear states of $\beta\beta$ decay. While it is expected to be good in the case of $\beta\beta0\nu$ decay , its validity is not trivial in the case of 2ν decay.
Formally the approximation is always valid if $< E_N >$ is defined by equating the right-han sides of equations

$$\begin{aligned}
&\frac{1}{\frac{1}{2}W_0 + < E_N > - E_I}\sum_N < 0^+_F||\tau^+\sigma||1^+_N >< 1^+_N||\tau^+\sigma||0^+_I >= \\
&\sum_N \frac{< 0^+_F||\tau^+\sigma||1^+_N >< 1^+_N||\tau^+\sigma||0^+_I >}{\frac{1}{2}W_0 + E_N - E_I}
\end{aligned} \tag{3.42}$$

If it is possible to calculate the right-hand side of this equation, which is just the decay amplitude $M_{2\nu}$, there is actually no need to invoke the closure approximation. In

practice, however, it may be technically difficult to perform an explicit summation especially in the case of a large-scale calculation. Then it becomes necessary to estimate the energy $< E_N >$ which satisfies (3.42) as well as possible. Vergados (1976) estimated it as the energy expectation value for the Gamow-Teller collective state $N\tau^+\sigma|0_I^+ >$, where N is a normalization constant. It can be calculated relatively easily but tends to overestimate the correct value of the closure energy because of the larger weight for higher-lying states.
To improve upon this method Haxton and Stephenson (1984).estimated $< E_N >$ from ta kind of weighted sum and instead of performing a shell-model calculation, which is just as difficult as the calculation of the right-hand side of (3.42), they used the parametrization of Gamow- Teller (GT) strength distribution made in statistical studies of 13 decay by the Waseda group (Takahashi and Yamada 1969, Koyama e l al 1970, Takahashi 1971).

3.7.2 Short-range correlations

Nuclear models employed in $\beta\beta$ decay calculations are usually based on the independent particle picture. While long-range correlations are taken into account by mixing of hasis states within their model spaces, the short-range *repulsive* correlations due to the nucleon hard core are absent in the model wavefunctions. Their effect is especially important for the calculation of matrix elements where the range of the relevant operators is of the order of the hard core radius.

Thus the average exchanged momentum is large, of the order of 100 MeV, so that the two neutrons tend to overlap. To prevent this a Jastrow type of correlation function, $f(r)$, has been introduced, in an ad-hoc manner, into the $\beta\beta0\nu$ calculations. As a form of *f(r)*, a simple *step function* with the hard core radius (Halpriu el al 1976, Vergados 1981) or a more realistic one (Miller and Spencer 1976):

$$\begin{aligned} f(r) &= 1 - e^{ar^2}(1 - br^2) \\ a &= 1.1fm^{-2}b = 0.68fm{-}2 \end{aligned} \tag{3.43}$$

can be assumed.

An approximate way to correct for this is to multiply two-nucleon wavefunctions by a correlation function $f(|\mathbf{r_1} - \mathbf{r_2}|)$ when we calculate transition matrix elements. This amounts to the replacement:

$$< ppJ_p||O^J||nn^{'}J_n >=< ppJ_pf||O^J||fnn^{'}J_n > \tag{3.44}$$

An approximate way to correct for this is to multiply two-nucleon wavefunctions by a correlation function $f(|\mathbf{r_1} - \mathbf{r_2}|)$ when we calculate transition matrix elements. This amounts to the replacement:

$$< ppJ_p||O^J||nn^{'}J_n >=< ppJ_pf||O^J||fnn^{'}J_n > \tag{3.45}$$

As a form of *f(r)*, a simple *step function* with the hard core radius (Halpriu el al 1976, Vergados 1981) or a more realistic one (Miller and Spencer 1976)

This way of using the Jastrow procedure is a very rudimentary way to introduce short-range correlations into many-nucleon systems. A more sophisticated microscopic approach for the inclusion of short-range correlations is the unitary correlation operator method (UCOM)[ref. 71].
In the UCOM one obtains the correlated many-particle state from the uncorrelated one by a *unitary* transformation and thus the norm of the correlated state is conserved and no amplitude is lost in the relative wave function. In [72, 73, 74] it was demonstrated that the Jastrow procedure leads to the excessive reduction of 25% - 40% in the magnitudes of $\beta\beta0\nu$ nuclear matrix elements. At the same time the UCOM reduces the magnitudes of the matrix elements only by 4% to 16%.
A fully consistent use of the UCOM method requires to treat not only the wave functions but the Hamiltonian, as well.

Nowadays the several Nuclear Models use to calculate $M_{0\nu}$ use different SRC: it doesn't exist a unique approach for this computational problem. Thus the results need to be compared in a consisten way, paying attention to the kind of SRC assumed, in order to avoid misunderstandings.

3.7.3 Phase Space factors

As already mentioned, the Phase Space Factors, or kinematical factor, used are fundamental and not unique for all the nuclear models.
In order to evaluate the relativistic function in the decay the Dirac equation for an electron in an electrostatic field generated by a total charge Z distributed uniformly in a sphere of the nuclear radius $R = r_0 A^{1/3}$ with $r_0 = 1.2fm$ (but not always this value is used!) must be solved. The wavefunction $\psi_{ps}(\epsilon, \mathbf{r})$ of an electron with (asymptotic) momentum p and spin projection s (normalized) can be expanded in terms of spherical waves:

$$\psi(\epsilon, \mathbf{r}) = \psi_s^{S_{1/2}}(\mathbf{r})(\epsilon, \mathbf{r}) + \psi_s^{P_{1/2}}(\epsilon, \mathbf{r}) + \psi_s^{P_{3/2}}(\epsilon, \mathbf{r}) \cdots \tag{3.46}$$

where, for example,

$$\psi_s^{s1/2} = \sqrt{F_0(Z_f, \epsilon)}\sqrt{\epsilon + m_e} \begin{pmatrix} \chi_s \\ \frac{\sigma \cdot \mathbf{p}}{\epsilon + m_e}\chi_s \end{pmatrix}$$

The leptonic currents are obtained integrating this wavefunctions.
If we consider the leading term for the $\beta\beta0\nu$ expression, it can be written as:

$$(T_{1/2}^{0\nu})^{-1} = |M^{(0\nu)}|^2 \cdot G_{01} \left(\frac{< m_{\nu e} >}{m_e} \right)^2 \tag{3.47}$$

where $|M^{(0\nu)}|$ is the NME, Nuclear Matrix Element, $< m_{\nu e} >$ is the effective neutrino mass, m_e is the electron mass and G_{01} is the phase space factor It is defined as:

$$G_{01} = \frac{a_{01}}{m_e^2 ln2} \int d\omega_{0\nu} F_0(Z, \epsilon_1) F_0(Z, \epsilon_2) \tag{3.48}$$

where.

$$a_{0\nu} = \frac{(Gg_A)^4 m_e^9}{64\pi^5}$$
$$d\omega_{0\nu} = m_e^{-5} p_1 p_2 \epsilon_1 \epsilon_2 \delta(\epsilon_1 + \epsilon_2 + E_f - E_i) d\epsilon_1 d\epsilon_2 d(\mathbf{p_1} \cdot \mathbf{p_2}) \tag{3.49}$$

We have assumed $S = 0$ electron wave functions with no r dependence. The Fermi functions, $F_0(Z, \epsilon)$, depend upon the charge of the daughter nucleus, Z, and the energy of the i^{th} electron, ϵ_i . In the early $\beta\beta0\nu$ calculations, the NME and kinematic factor were defined as above. The NME were given in units of fm^{-1} and the kinematic factors in units of $yr^{-1}fm^2$ (for example, [79]). In the mid-eighties, a scaling factor was introduced into the $\beta\beta0\nu$ theory. The ν potential (induced by the virtual ν exchange)

$$H_K(r, E_a) = \frac{1}{2\pi^2} \int \frac{dq}{\omega} \frac{1}{\omega + A_K} e^{i\mathbf{qr}} \tag{3.50}$$

where the pedix a indicates the intermediate states (and A_K is a combination of the initial, final and electron energies), is scaled by a factor of $R = r_0 A^{1/3}$ such that the NME are dimensionless.
The scaling factor, R, in is compensated for by introducing $1/R^2$ into the definition of the kinematic factor

$$G_{01}^S(R) = \frac{a_{01}}{(m_e R)^2 ln2} \int d\omega_{0\nu} F_0(Z, \epsilon_1) F_0(Z, \epsilon_2) \tag{3.51}$$

The $G_{01}^S(R)$ have been calculated by many authors; for example, [80] using $R = 1.2A^{1/3}$ and [81] using $R = 1.1A^{1/3}$.

As illustrated, the parameters g_A and r_0 are fundamental for the final evaluation of the decay rate.
The fact the different nuclear models use different values for these parameters introduces difficulties in the comparison between the different results for $|M^{(0\nu)}|$. The work of organization and comprehension of the different approaches I made includes all these details.

3.8 Nuclear Models

3.8.1 Shell Model

The nuclear shell model has a nice feature that it can provide us with microscopic wave-functions which have a given set of quantum numbers such as parity, angular momentum and isospin corresponding to the symmetry properties of the Hamiltonian. These wave-functions automatically include any correlations caused by the interaction part of the Hamiltonian provided that the model space is taken to he large enough. This last condition, however, is often difficult to satisfy.
In the case of $\beta\beta$ decay, ^{48}Ca is probably the only nucleus which can be treated in the conventional shell model reasonably well. As one goes to heavier nuclei the number

of basis states increases explosively.Although it is not conceivable that all of these are equally important, it is difficult to select important ones without the knowledge about *true* wavefunctions. An assumption of weak coupling between the proton and neutron systems gives a possible way to *truncate* the huge model space to a tractable one.

The nuclear shell model (SM) was introduced [75], [76] some 55 years ago to explain the regularities of the nuclear properties associated with magic numbers. Its authors proposed an independent particle model, assuming that the main effect of the two body nucleon - nucleon interaction was to generate a *mean field*.
They modelled this mean field as the sum of a harmonic oscillator potential plus a spin-orbit force:

$$h(r) = \frac{1}{2}m\omega^2 r^2 - C\bar{l}\bar{s} \tag{3.52}$$

The success of the independent particle model strongly suggests that the very singular free NN interaction can be regularized in the nuclear medium. Starting with a regularized interaction, the exact solution of the secular problem, in the (infinite) Hilbert space, built on the mean field orbits, is approximated in the large scale shell model calculations by the solution of the Schrodinger equation in the valence space, using an effective interaction such that:

$$H\psi = E\psi \rightarrow H_{eff}\psi_{eff} = E\psi_{eff} \tag{3.53}$$

In general, effective operators have to be introduced to account for the restrictions of the Hilbert space

$$< \psi|\mathbf{O}|\psi > = < \psi_{eff}|\mathbf{O}_{eff}|\psi_{eff} > \tag{3.54}$$

The fundamental advantage of the SM is the theoretical possibility of describing simultaneously all the spectroscopic properties of the low-lying states either of collective or single-particle nature for a large domain of nuclei. The limitations come from the fact that sometimes the tractable valence spaces are too small to encompass the desired properties of a nucleus. To carry out an SM study it is necessary [77]

- To define a valence space (inert core, active shells).
- To derive an effective interaction.
- To build and diagonalize the Hamiltonian matrix.

The latest Shell Model calculations contemplates SRC corrections. The point is that the theoretical physicists present their results *without* assuming a clear position respect to the kind of SRC to be used. There are results obtained with JASTROW as well with UCOM corrections.
Another source of *uncertainity*, or better, of difficulty in order to compare the different NME results, is the use of different values of g_A. In the case of Shell Model the value used is $g_A(0) = 1.25$, with $g_V(0) = 1$. In order to compare the results, the central value is used. The Phase Space Fator to be used wiht SM calculation is that `PR300(1998)`.

FIGURE 3.3: Shell model and experimental level schemes for $N = 126$ isotones in the $r5i$ space.

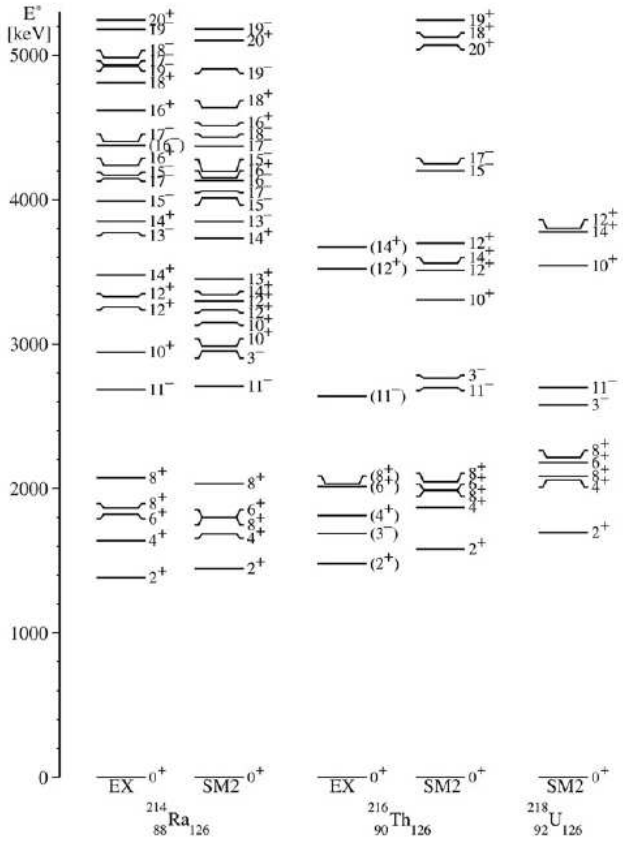

3.8.1.1 Valence space

The choice of the valence space is strongly conditioned by the problem of the diagonalization of the energy matrix. The dimension of the matrices increases exponentially with the number of single particle states in the valence space and with the number of particles (holes) in it (valence particles). Another important remark is that a valence space can be adequate to describe some properties and completely inadequate for others.

Light nuclei have been extensively studied in the framework of the SM:

- $2 \leq N,\ Z \leq 8p$ shell nuclei valence space: $0p_{3/2}$, $0p_{1/2}$.
- $8 \leq N,\ Z \leq 20sd$ shell nuclei valence space: $0d_{5/2}$, $0d_{3/2}$, $1s_{1/2}$

The next step is the *pf* shell which has also been extensively studied [78] at least for nuclei with $20 \leq N,\ Z \leq 32$.

3.8.2 Interactive Boson Model - IBM

The IBM is a relatively new model, its purpose is threefold:

- (i) to provide an independent calculation and investigate the sensitivity of the results to assumptions made concerning the single-particle energies and strengths of interactions;
- (ii) to make use of wave functions of initial and final nuclei which are as much as possible realistic, i.e., that describe accurately the known properties of those nuclei; and
- (iii) to extract simple features, if any, of the otherwise complex calculation.

The matrix elements which are studied by the model are that of the F (Fermi), GT (Gamow-Teller), and T (Tensor) operators.
IBM-2 model considers matrix elements of the fermionic operators in the collective SD subspace formed by pair states with $J^P = 0^+$ and $J^P = 2^+$ of identical nucleons. The pair operators that create these states are written introducing creation and annihilation operators for single particle states, $c^\dagger_{nljm}$:

$$\begin{aligned} S^\dagger &= \sum_j \alpha_i \sqrt{\frac{\Omega_j}{2}} (c^\dagger_j \times c^\dagger_j)^{(0)} \\ D^\dagger &= \sum_{j \le j'} \beta_{j,j'} \frac{1}{\sqrt{1+\delta_{jj'}}} (c^\dagger_j \times c^\dagger_j)^{(2)} \end{aligned} \tag{3.55}$$

with $\Omega = j + \frac{1}{2}$. Several methods have been used to determine the structure coefficients α_i and $_{jj'}$.
The Shell Model states in the SD subspace are constructed as:

$$|n, v, J >= \eta^{-1}_{nvJ} (S^\dagger)^{\frac{n-v}{2}} |n, v, j > \tag{3.56}$$

where all labels other than seniority v and total angular momentum J have been omitted. η^{-1}_{nvJ} is a normalization constant. Thus, in this seniority general scheme, matrix elements of the fermion operator can be calculated. These general results are needed for the calculation of matrix elements in the *interacting boson model*. In the 'generalized seniority scheme (GS), in which the wave functions of ground state of nuclei have $v = 0$, the double-β decay matrix elements depend only on the structure coefficients, α_i.

In the microscopic IBM [85], the shell-model SD pair states are mapped onto sd boson states with $J^P = 0^+$ and $J^P = 2^+$. Fermionic operators are similarly mapped into bosonic operators by the Otsuka, Arima, and Iachello (OAI) method [86]. Using this method one is assured that the matrix elements between fermionic states in the collective subspace are identical to the matrix elements in the bosonic space.

Because in the IBM particles (p) are considered in the first half of a major shell, and holes (h) in the second half, the mapping must respect particle-hole conjugation.

Thus:

- The INTERACTING BOSON MODEL is a model of even-even nuclei in terms of correlated pairs of protons and neutrons with angular momentum $J = 0, 2$ treated as bosons , called IBM-2 [82].

- The INTERACTING BOSON FERMION MODEL is a model of odd-even or odd-odd nuclei in terms of correlated pairs (bosons) and unpaired particles, (fermions), called IBFM-2.

The logic of the method is:

- Choose the operator, T, whose matrix element one wants to calculate.
- Map this operator onto the bosonic space by the OAI method [84]
- Determine realistic wave functions by comparison with experimental data on energies and electromagnetic transition rates.
- Calculate matrix elements of the boson image of T with realistic wave functions.

The different contribution to the matrix element are well summarized by the following expression:

$$M^{(0\nu)} = M^{(0\nu)}_{GT} - \left(\frac{g_V}{g_A}\right)^2 \cdot M^{(0\nu)}_F + M^{(0\nu)}_T \tag{3.57}$$

The sensitivity to operator assumption requires particular attention. IBM-2 uses the definition

$$V = \frac{1}{2}\sum_{n,n'} \tau^\dagger_n \tau^\dagger_{n'} V_{n,n'} \tag{3.58}$$

and the matrix elements are calculated in units of fm^{-1} . For comparison with SM and QRPA (which will be discussed in the next section) with operator

$$V = \sum_{n,n'} \tau^\dagger_n \tau^\dagger_{n'} V_{n,n'} \tag{3.59}$$

and matrix elements expressed in dimensionless units, IBM.-2 method needs the matrix elements to be multiplied in fm^{-1} by $2R$ with $R = 1.2A^{1/3}$fm. This point, i.e. which operator is used in which calculation, should be clarified.
If the factor of $1/2$ is not included in V, a factor of $1/4$ should be included in the kinematical factor when calculating the half-life,

$$\left[T^{0\nu}_{1/2}(0^+ \to 0^+)\right]^{-1} = \frac{1}{4} F^{(0)}_{11} |M^{(0\nu)}|^2 \left(\frac{< m_\nu >}{m_e}\right)^2$$

where $F^{(0)}_{11}$ is in $y^{-1} \cdot fm^2$ units and $|M^{(0\nu)}|^2$ is in fm^{-2}

The sensitivity of 5% is estimated by comparing the matrix elements in the Tomoda formulation of V_{nn} with those in the formulation of Šimkovic et al., disregarding the factor 1/2.
The parameters used in IBM-2 are:

- $g_A = 1.25$
- $r_0 = 1.2$ fm

The SRC corrections are taken into account by multiplying the potential $H(r)$ by the Jastrow function squared, $f(r)^2$. For the sake of comparison to other calculations, the phase convention of Tomoda [87] with $g_V = 1$, $g_A = 1.25$ and $r_0 = 1.2$.

As illustrated, even if the model is a relatively new one, it is pretty similar to the shell model from some technical aspects; at least it is need to say that the SM is the starting point of IBM-2.

3.8.3 RPA

The Hartree Fock model which is the starting point of the Shell Model includes long-range interactions (*p-h* interactiond). In order to obtain p-p correlations it is need to introduce a kind of short range correlations (*p-p* interactions) and thus the *quasiparticles*. There are several experimental evidences of the pairing effect, like:

- **Even-odd effect**: The *pd* nuclei binding energy is not the simple average between *pp* and *dd* nuclei energies. levels (up to 1.5 MeV)
- **Deformations** Shell Model doesn't explain the sudden deformations for semi-full shells.

The angular momentum I is different fot N_{pp} and N_{pd}, for the first kind of nuclei the ground state is 0^+, while in the second case I is determined by the last *odd*-nucleon. The pairing force is: an actractive force, between two nucleons, a short range force because it s such that the coupling of two nucleons in a given shell j is energetically favoured in the channel $I = 0$ (which means that the nucleons have the same —**m**—). Thus a new potential, a pairing potential, nedds to be introduced, besides the usual average potential $< V >$ which rules the interactions between nuclei (the SM-Hartree Fock potential). The most fundamental difference respect to the seniority scheme is that the numbers of particles (couples) is *not* conserved, because of the introduction of probability amplitudes for the occupancies (or vacancies) of a particular state. The theory inherits from the *BCS* (Barden-Cooper-Schrieffer) theory for semiconductors.

Thus a new kind of fermions is introduced: the quasiparticles, created by the QP-operators, whihc mix the usual II-quantization operators of creation and annihilation:

$$\begin{aligned}
&\alpha_k = u_k a_k^\dagger - v_k a_{\tilde{k}} \\
&\alpha_{\tilde{k}} = u_k a_{\tilde{k}}^\dagger - v_k a_k \\
&\left\{\alpha_k, \alpha_{k'}\right\} = 0 \qquad \left\{\alpha_k, \alpha_k^\dagger\right\} = \delta_{k,k'} \\
&|BCS> \approx \prod_k \alpha_k |- >
\end{aligned} \tag{3.60}$$

where u_k and v_k are the probability amplitude for the occupancy or vacancy of a particular state k, a_k and $a_k^\dagger$ are the usual fermion creation and annihilation operators, which satisfy the Poisson Algebra, by definition.
The quasiparticles have some peculiar properties:

- above the Fermi surface $v^2 \ll 1$ (there are only particles), while
- below the Fermi surface $u^2 \ll 1$ (there are almost only holes).

Thus, yet with the linear Bogoliugov trasformations, we have a GS (Ground State) of interacting particles in a gas of not-interacting quasiparticles, with the difference respet to the seniority scheme that the total number of particles is not conservated (there is the introduction of probability amplitude and a mixture of creation and annihilation operators).
The most important result for the BCS theory is that it predicts a corret GS value.

To summarize all the Microscopic structure theories presented up to now and to be presented later, we have:

- **SM** : it is based on the Hartree Fock theory to build the states, the particles are in a mean field $< V > \rightarrow \Gamma$ (which accounts for long-range interactions), but if the shells are not full some correlations (pairing effects) need to be introduced.
- **BCS** theory explain this interactions introducing $V_{pairing} \rightarrow \Delta$ (wich is the sum of short-range correlations), and quasiparticles ideas.

HFB (Hartree Fock Bogoliugov) therory unifies the two models: the states are the product of *indipendent qusiparticles* and it includes both the Γ as well the Δ potential .

The fundamental idea is to represent the GS as vaccum respect to the QP (Quasi Particles) which are the lowest possible excitation. The previous idea of this kind was that formulated by Landau-Midgal. Thus :

- QP vacuum comes from a variational priciple (it needs $u = v = 0$, which are themselves derived from the energy expectation value minimization) and thus it is an extension of the BCS theory.

- The model has a *linear* connection with the bare particles.

The new operators mix again the creations and annihilation fermionic operators and are invertibles:

$$\beta_k = \sum_l U_{lk} c_l^\dagger + V_{lk} c_l \tag{3.61}$$

The linear trasformations are:

$$\begin{pmatrix} \beta \\ \beta^\dagger \end{pmatrix} = \begin{pmatrix} U^\dagger & V^\dagger \\ V^T & V^T \end{pmatrix} \begin{pmatrix} c \\ c^\dagger \end{pmatrix} = W \begin{pmatrix} c \\ c^\dagger \end{pmatrix} \tag{3.62}$$

where. W is a unitary transformation, β and $\beta^\dagger$ obeys the fermionic rules and the GS is such that $\beta^\dagger|\psi>=0\ \forall k$. Thus the RPA in its original form comes from this ideas.

The **RPA** nuclear model doesn't come from variational priciples.

- a complete set of H eigenstates is used.
- a collective *ph* operator, Q_v, is defined.

the operator is such that $Q_v|0>=0$, $v>=Q_v^\dagger|0>$, $Q_v^\dagger = \sum_{mi} C_{mi}^v a_m^\dagger a_i$. The latter is the most general creation (and vibration) operator. The GS is generalizaed: *ph* pairs are created and annihilateed.

$$Q_V^\dagger = \sum_{mi} \mathbf{X}_{mi}^v a_m^\dagger a_i - \sum_{mi} \mathbf{Y}_{mi}^v a_i^\dagger a_m \qquad\qquad Q_V|RPA>=0 \tag{3.63}$$

The two matrices, $\mathbf{X}$ and $\mathbf{Y}$, describe the two possible kind of variations: $a_m^\dagger a_i$, $a_i^\dagger a_m$.

This is the quasi-boson approximation

$$<RPA|a_i^\dagger a_m, a_n^\dagger a_j|RPA>=<HF|a_i^\dagger a_m, a_n^\dagger a_j|HF>=\delta_{ij}\delta_{mn} \tag{3.64}$$

The quasi-boson approximation would be an *exact* relation if the operators were boson-operators. The usual fermionic operators $(a_m^\dagger, a_i)$ are now *replaced* with the *ph* operators $(B_{mi}^\dagger, B_{mi}^\dagger)$ which obey:

$$\left[B_{mi}, B_{m'i'}^\dagger\right] = \delta_{i,i'}\delta_{m,m'}$$

But the Quasi-Boson approximation contemplates a *truncation* in the fermionic operators expansion into bosonic operators, thus the relation can't be exact and it is, as it is called, an approximation. The meaning of $\mathbf{X}$ and $\mathbf{Y}$ matrices is that they represent the probability of finding $a_m^\dagger a_i|0>$ and $a_i^\dagger a_m|0>$ in a excitated state ν:

$$\begin{aligned}\rho^{\nu}_{im} &=< 0|a^{\dagger}_i a_m|\nu >= \mathbf{X}\nu_{mi} \\ \rho^{\nu}_{im} &=< 0|a^{\dagger}_m a_i|\nu >= \mathbf{Y}\nu_{mi}\end{aligned} \tag{3.65}$$

The RPA equations are.

$$\begin{pmatrix} A & B \\ B^* & A^* \end{pmatrix} \begin{pmatrix} \mathbf{X}^{\nu} \\ \mathbf{Y}^{\nu} \end{pmatrix} = \hbar\Omega_{\nu} \begin{pmatrix} 1 & 0 \\ 0 & -1 \end{pmatrix} \begin{pmatrix} \mathbf{X}^{\nu} \\ \mathbf{Y}^{\nu} \end{pmatrix} \tag{3.66}$$

Moreover ortonormality conditions are imposed: even the *excited* states are orthonormal to each other

$$\delta_{\nu\nu'} = \sum_{mi} \mathbf{X}^*_{mi}\mathbf{X}_{mi}\mathbf{Y}^*_{mi}\mathbf{Y}_{mi} \tag{3.67}$$

Thus the final RPA Hamiltonina is

$$H = E_{RPA} + \sum_{\nu} \Omega_{\nu}\hbar\mathbf{O}^{\dagger}_{\nu}\mathbf{O}_{\nu} \tag{3.68}$$

Ai it is clear the equation (3.67) is armonic oscillator Hamiltonian, RPA is defined *armonic approximation*. The H_B eigenfunction are the RPA ground state; the ground state energy is such that

$$E_{HF} - E_{RPA} \geq 0$$

the eigenfunctions are expressed with the genralized oscillator coordinates.

$$\begin{aligned}Q_{\nu} &= \sqrt{\frac{\hbar}{2M\Omega_{\nu}}}(O_{\nu} + O^{\dagger}_{\nu}) \\ P_{\nu} &= \frac{1}{i}\sqrt{\frac{\hbar}{2M\Omega_{\nu}}}(O_{\nu} - O^{\dagger}_{\nu})\end{aligned}$$

3.8.4 QRPA: theory of linear response

Away from the closed shells, pair correlations become so important that the *feedback* of these correlations on single-particle motion cannot be neglected any more. HF, BCS and HFB ground states are inappropriate in such cases. It turns out that ph and pp may be encapsulated into one equation.

In calculating collective excitations of the nuclear system, so far the stationary Schrödinger equation has been used and the Hamiltonian has been diagonalized in some approximation. The innovative starting point of RPA an QRPA is the influence of an external time dependent field *F(t)*, which is a one-body operator:

$$\begin{aligned}F(t) &= fe^{-i\omega t} + f^{\dagger}e^{+i\omega t} \\ F(t) &= \sum_{kl} f_{kl}a^{\dagger}_k a_l\end{aligned} \tag{3.69}$$

is investigated. It is weak and introduces small changes of the nuclear density, which can be treated in linear order. Thus the nuclear density ρ oscillates with this external field and there are resonances whenever the frequency ω is close to an excitation of the system.

$$\delta\rho(t) = \delta\rho e^{-i\omega t} + \delta\rho^{\dagger} e^{+i\omega t} \tag{3.70}$$

In this way the RPA excited states derive directly from the equations for $< 0|a_i^{\dagger} a_m|\nu >$.

FIGURE 3.4: graphical rappresentation of the matrix elements $< ph^{-1}|and|0 >$ and $< hp^{-1}|and|0 >$.

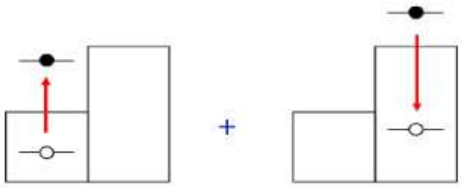

The motion eqaution becomes:

$$i\hbar\delta r\dot{h}o = \left[h^{(0)}, \delta\rho\right] + \left[\frac{\delta h}{\delta\rho}, \rho(0)\right] + [f, \delta\rho] \tag{3.71}$$

Thus the external field $f(t)$ introduces oncillations of small amplitude about the stationary states $\rho^{(0)}$.
The eigenvalue eqution can be written in terms of paticles-holes variations, $\delta\rho_{ph}$,

$$\begin{aligned} \hbar\omega\delta\rho_{ph} &= (\epsilon_p - \epsilon_h)\delta\rho_{ph} \\ &+ \sum_{p'h'} < ph^{-1}|\frac{\delta h}{\delta\rho}|p^{'}h^{'-1} > \delta\rho_{p'h'} \\ &+ \sum_{p'h'} < ph^{-1}|\frac{\delta h}{\delta\rho}|h^{'}p^{'-1} > \delta\rho_{p'h'} \end{aligned} \tag{3.72}$$

if

$$\delta\rho_{ph} = \mathbf{X}_{ph} \qquad\qquad \delta\rho_{hp} = \mathbf{Y}_{hp} \tag{3.73}$$

the states become

$$|n >= \sum_{ph} \mathbf{X}_{ph}|ph^{-1} > + \mathbf{Y}_{hp}|hp^{-1} > \tag{3.74}$$

Thus the QRPA is, in very synthetic words, like RPA, but with quasiparticles. Particles and holes are finally mixed and new matrix elements appear, which correlate particles-particles *pp*, as holes-holes *hh* and particles-holes *ph*.

$$\begin{pmatrix} A & B \\ B^* & A^* \end{pmatrix} \begin{pmatrix} \mathbf{X} \\ \mathbf{Y} \end{pmatrix} \hbar\Omega_\nu = \begin{pmatrix} 1 & 0 \\ 0 & -1 \end{pmatrix} \begin{pmatrix} \mathbf{X} \\ \mathbf{Y} \end{pmatrix} \tag{3.75}$$

where

$$\begin{aligned} A_{ph,p'h'} &= \delta_{pp'hh'}(\epsilon_p - \epsilon_h) + \frac{\delta^2\epsilon}{\delta_{ph}\delta_{p'h'}} \\ B_{ph,p'h'} &= \frac{\delta^2\epsilon}{\delta_{ph}\delta_{p'h'}} \end{aligned} \tag{3.76}$$

contain two typs of matrix elements: pp-matrix elements (which are close to pp or hh matrix elements) and ph-matrix elements.

The QRPA nuclear model introduces a generlized density R, in terms of which it is possible to describe the motion equations.

$$i\hbar\delta\dot{R} = \left[H^{(0)}, \delta R\right] + \left[\frac{\delta H}{\delta R}\delta R, R^{(0)}\right] + [f, \delta R] \tag{3.77}$$

with R which describes the *pp*, *ph*, *hh* creations.

$$R = \begin{pmatrix} < \phi|a^\dagger_{l'}a_l|\phi > & < \phi|a_{l'}a_l|\phi > \\ < \phi|a^\dagger_{l'}a^\dagger_l|\phi > & < \phi|a_{l'}a^\dagger_l|\phi > \end{pmatrix} \tag{3.78}$$

Once solved the QRPA equations, the states are expressed ina new basis $|n>$

$$|n>= \sum_{k,k'} \mathbf{X}_{k,k'}\beta^\dagger_k\beta^\dagger_{k'}|0> + + \mathbf{Y}_{k,k'}\beta_k\beta_{k'}|0> \tag{3.79}$$

3.9 NME comparison

As illustrated in the previous sections, there are two fundamental variables which determine the final nuclear contribution to the $\beta\beta0\nu$ half life:

- The $G^{0\nu}$ factors, which should be univocal for all the nuclear models, but they are *not*, given different input parameters are used to calculate them (r_0, g_A...).
- The $M^{0\nu}$ which depends on the nuclear model used and on the initial an final states J^P.

Thus the comparison between different results need to be made carefully, considering the $M^{0\nu}$'s are not directly comparable.

FIGURE 3.5: $|M|^{(0\nu)}$'s comparison for several nuclei. This kind of represantation is meaningless, it is not possible to appreciate the *trend* of all the nuclear models to converge to the same result.

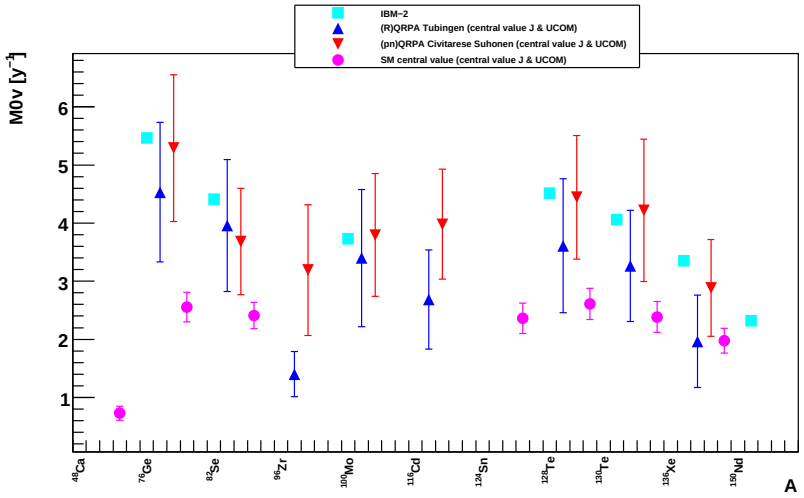

FIGURE 3.6: $|M|^{(0\nu)}$ comparison in log-scale

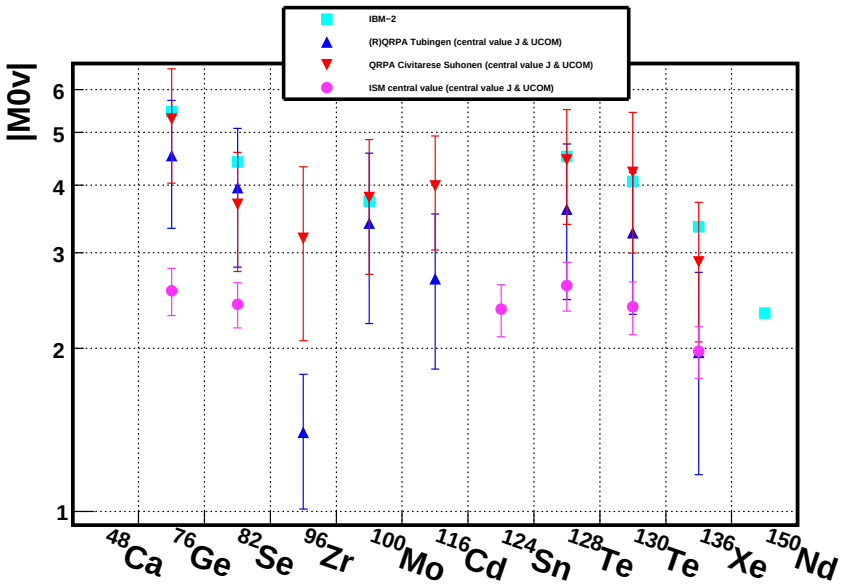

Another factor should be compared instead of the mere matrix elements, i.e,, the nuclear factor of merit $F_N = G_{0\nu}|M^{0\nu}|^2$. In caculating this quantity much attention need to be payed in order to combine properly the factors.
As already mentioned in the previous sections, some nuclear models declare the kind of Phase Space Factors used, while others do *not*, but it is possible to perform its calculation from the NME and τ given in the papers.

From the F_N comparison it is possible to appreciate the results convergence. The weird fact is that the nuclear models differ among them, neverthless their results coverge.

FIGURE 3.7:

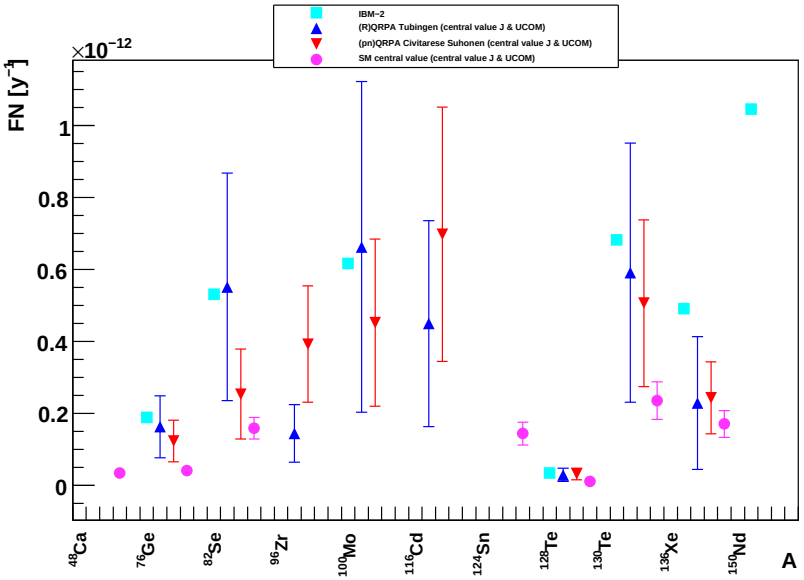

FIGURE 3.8:

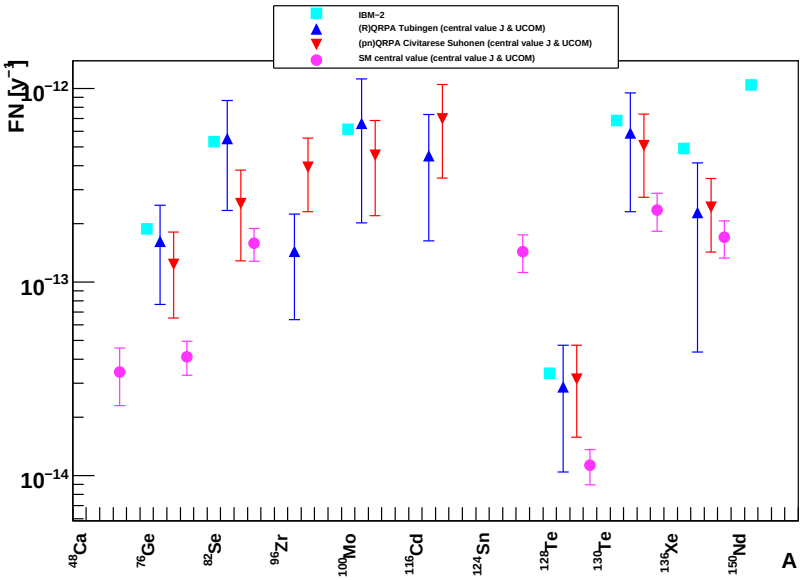

All the reavant informations were collected and organized in a databse, in order to have a reliable comparison between different nuclear models and thus between different experiment sensitivities. All the informations relative to

- the kind of SRC used, JASTROW or UCOM.
- g_A and g_V values used.
- the value of r_0.
- the Phase Space Factors used in each nuclear model.

All the references are pointed out. With all these variables the calculations for neutrinoless double beta decay τ for $m_{ee} = 10, 50$ meV are performed.

isotope	R$[fm]$	R$[fm]$	[88], [89] Simkovic	[90] Suhonen	[91]Suhonen$'$	[92]Tomoda
$r_0[fm]$	1.1	1.2	1.1	1.2	*1.2	1.2
g_A			1.25	1.25	1.00	1.25
^{48}Ca	3.989	4.361	$8.00 \cdot 10^{-14}$	$6.400 \cdot 10^{-14}$	$\cdots$	$4.906 \cdot 10^{-12}$
^{76}Ge	4.659	5.083	$8.00 \cdot 10^{-15}$	$6.00 \cdot 10^{-15}$	$3.000 \cdot 10^{-15}$	$6.700 \cdot 10^{-13}$
^{82}Se	4.779	5.213	$3.500 \cdot 10^{-14}$	$2.700 \cdot 10^{-14}$	$1.000 \cdot 10^{-14}$	$3.063 \cdot 10^{-12}$
^{86}Zr	5.037	5.495	$7.000 \cdot 10^{-14}$	$5.700 \cdot 10^{-14}$	$2.4 \cdot 10^{-14}$	$\cdots$
^{100}Mo	5.106	5.569	$5.700 \cdot 10^{-14}$	$4.400 \cdot 10^{-14}$	$1.800 \cdot 10^{-14}$	$5.760 \cdot 10^{-12}$
^{116}Cd	5.365	5.852	$6.200 \cdot 10^{-14}$	$4.700 \cdot 10^{-14}$	$1.900 \cdot 10^{-14}$	$\cdots$
^{128}Te	5.544	6.048	$2.000 \cdot 10^{-15}$	$2.000 \cdot 10^{-15}$	$1.000 \cdot 10^{-15}$	$2.700 \cdot 10^{-13}$
^{130}Te	5.572	6.079	$5.500 \cdot 10^{-14}$	$4.100 \cdot 10^{-14}$	$1.700 \cdot 10^{-14}$	$6.640 \cdot 10^{-12}$
^{136}Xe	5.657	6.171	$5.900 \cdot 10^{-14}$	$4.400 \cdot 10^{-14}$	$1.700 \cdot 10^{-14}$	$7.279 \cdot 10^{-12}$
^{150}Nd	5.845	6.276	$2.690 \cdot 10^{-13}$	$1.940 \cdot 10^{-13}$	$\cdots$	$3.452 \cdot 10^{-11}$
^{154}Sm	5.896	6.432	$\cdots$	$\cdots$	$\cdots$	$\cdots$
^{124}Sn	5.485	5.984	$\cdots$	$2.600 \cdot 10^{-14}$	$\cdots$	$\cdots$

TABLE 3.1: $G_{0\nu}$ in y^{-1}, save for the last column, where they are expressed in $[y^{-1} \cdot fm^2]$. * the $G_{o\nu}$ is calculated from $\tau_{1/2}$ in *JoP: Conference series 173 (2009) 012012*. When "$\cdots$" is found it means no value is available.

From the table 3.1 is possible to appreciate the discrepancies between the Phase Space Factors used, which differ among them of an average factor of 5.
The first three columns refers to the *pn* (Suohnen) and *r* (Simkovic) **QRPA** nuclear schools. The difference between them is, from a technical point of view, the kind of g_{pp} (particle-particle interaction) used.

Regarding the Simkovic *pn-QRPA* school [93] (4^{st} column are the are the $G^{0\nu}$'s used by this model):

- The minimun and maximun $|M^{0\nu}|$ are presented (obtained for $\tau(m_{\beta\beta}) = 50meV$), which are the results of 24 different calculations
- the parameters which are made to fluctuate are g_{pp}, g_A and the SRC used (Jastrow or UCOM). The g_{pp} used is such that the calculation for $\beta\beta 2\nu$ are reproduced.

- Though it is impossible to discriminate which is the $M^{0\nu}$ to be used, the central value is presented.

Regarding the Suohnen [94] *r-QRPA* school (5^{th} and 6^{th} columns are the $G^{0\nu}$'s used by this model):

- The details are illustrated, the $!M^{0\nu}$ are explicitly indicated, and it is clear which values of g_{pp} and g_A are used.
- Also the obtained τ (for $m_{ee} = 1meV$) are illustrated.
- The information given were used to ricalculate the Phase Space Factors of *PR300*; this let to find an error in the ^{100}Mo $G^{0\nu}$ tabulated.
- Even in this case the central value is presented for comparison.

Regarding the Shell Model [95] (in the 7^{th} column there are the $G^{0\nu}$'s used by this model):

- The calculations include SRC and HOC (High Order Corrections) correction.
- The SRC used are the usual JASTROW and UCOM, but there is not a clear indication of which is to be used. Also the $\tau^{0\nu}$ is presented. This allowed to recalculate the PR300 $G^{0\nu}$' s.
- the central value is represented, for comparison.

Regarding the IBM-2 model [96]:

- the $|M^{0\nu}|$ are obtainde using the Miller-Spencer JASTROW SRC.and the g_A value used is 1.25. An unique value is presented.
- the NLO (Next to Leading Order) corrections are omitted, since they are negligible for all the A.
- The results (the $|M^{0\nu}|$'s) are can be combined in different ways.When they are adimensional, the PR 300 $G^{0\nu}$'s can be used directly, and those are the most recent calculated. But, if the $|M^{0\nu}|$'s are divided for a factor *2R* (with $r_0 = 1.2fm$), the $G^{0\nu}$'s from the old formulation (RPP 54) can be used. The final result, the F_N factor, must be the same.
- the strange and interesting fact is that IBM-2 model does not totally agree with the SM, even if the two models should agree at least for spherical nuclei.

In the following two tables (3.2 and 3.3) I report the data for ^{130}Te, which is the isotope under study for the CUORE experiment. The two tables are to be read tohgeter.

model	$\mathbf{g_{PP}}$	$\mathbf{g_A}$	**s.r.c**	$\mathbf{G^{0\nu}}$
rQRPA	$\beta\beta2\nu$	1.25&1	**J**	Simkovic ($r_0 = 1.1$)
rQRPA	$\beta\beta2\nu$	1.25&1	**J**	Simkovic ($r_0 = 1.1$)
r(QRPA)	$\beta\beta2\nu$	1.254&1.0	**J**	Simkovic ($r_0 = 1.1$)
r(QRPA)	$\beta\beta2\nu$	1.254&1.0	**U**	Simkovic ($r_0 = 1.1$)
r(QRPA)	$\beta\beta2\nu$	1.254&1.0	**U**	Simkovic ($r_0 = 1.1$)
r(QRPA)	$\beta\beta2\nu$	1.254&1.0	**U**	Simkovic ($r_0 = 1.1$)
r(QRPA)	$\beta\beta2\nu$	1.254&1.0	**U+J**	Simkovic ($r_0 = 1.1$)
IBM-2	$\cdots$	1.254	**J**	Suhonen *PR300* ($r_0 = 1.2$)
IBM-2	$\cdots$	1.254	**J**	Tomoda ($r_0 = 1.2$)
pn(QRPA)	0.84	1.000	**J**	Suhonen-from $\tau_{1/2}$ ($r_0 = 1.2$)
pn(QRPA)	0.84	1.000	**U**	Suhonen-from $\tau_{1/2}$ ($r_0 = 1.2$)
pn(QRPA)	0.90	1.254	**J**	Suhonen-from $\tau_{1/2}$ ($r_0 = 1.2$)
pn(QRPA)	0.90	1.254	**U**	Suhonen-from $\tau_{1/2}$ ($r_0 = 1.2$)
pn(QRPA)	$\cdots$	$\cdots$	**J**	central F_N **J** s.r.c.
pn(QRPA)	$\cdots$	$\cdots$	**U**	central F_N **U** s.r.c
pn(QRPA)	$\cdots$	$\cdots$	**J+U**	central F_N **J+U** s.r.c.
ISM	-	1.254	**J**	Suhonen ($r_0 = 1.2$)
ISM	-	1.254	**U**	Suhonen ($r_0 = 1.2$)
ISM	-	1.254	**J+U**	Suhonen ($r_0 = 1.2$)

TABLE 3.2: see text.

NME	$\mathbf{\lvert M^{0\nu}\rvert}$	$\mathbf{F_N}$	$\tau(\mathbf{1meV})$	$\tau(\mathbf{50meV})$
MIN NME-J	2.270	$2.83 \cdot 10^{-13}$	$9.21 \cdot 10^{23}$	$3.69 \cdot 10^{26}$
MAX NME-J	3.380	$6.28 \cdot 10^{-13}$	$4.16 \cdot 10^{23}$	$1.66 \cdot 10^{26}$
central value NME-J	2.825	$4.389 \cdot 10^{-13}$	$5.95E \cdot 10^{23}$	$2.38 \cdot 10^{26}$
central value NME-J	2.840	$4.436 \cdot 10^{-13}$	$5.89 \cdot 10^{23}$	$2.35 \cdot 10^{26}$
MIN value for NME-U	4.260	$9.981 \cdot 10^{-13}$	$2.62 \cdot 10^{23}$	$1.05 \cdot 10^{26}$
MAX value for NME-U	3.550	$6.931 \cdot 10^{-13}$	$3.77 \cdot 10^{23}$	$1.51 \cdot 10^{26}$
central value for NME-U s.r.c	3.265	$5.863 \cdot 10^{-13}$	$4.45 \cdot 10^{23}$	$1.78 \cdot 10^{26}$
$\lvert M^{0\nu}\rvert$	4.059	$6.755 \cdot 10^{-13}$	$3.87E \cdot 10^{23}$	$1.55 \cdot 10^{26}$
$\lvert M^{0\nu}\rvert/2R$	0.334	$7.401 \cdot 10^{-13}$	$3.53 \cdot 10^{23}$	$1.41 \cdot 10^{26}$
NME-J	-4.061	$2.804 \cdot 10^{-13}$	$9.31 \cdot 10^{23}$	$3.73 \cdot 10^{26}$
NME-U	-5.442	$5.035 \cdot 10^{-13}$	$5.19 \cdot 10^{23}$	$2.07 \cdot 10^{26}$
NME-J	-2.993	$3.673 \cdot 10^{-13}$	$7.11 \cdot 10^{23}$	$2.84 \cdot 10^{26}$
NME-U	-4.221	$7.305 \cdot 10^{-13}$	$3.57 \cdot 10^{23}$	$1.43 \cdot 10^{26}$
-		$3.238 \cdot 10^{-13}$	$8.06 \cdot 10^{23}$	$3.23 \cdot 10^{26}$
-		$5.054 \cdot 10^{-13}$	$5.17 \cdot 10^{23}$	$2.07 \cdot 10^{26}$
NME **J**	2.120	$1.843 \cdot 10^{-13}$	$1.42 \cdot 10^{24}$	$5.67 \cdot 10^{26}$
NME **U**	2.650	$2.879 \cdot 10^{-13}$	$9.07E + 023 \cdot 10^{23}$	$3.63 \cdot 10^{26}$
central value for NME **J+U** s.r.c.	2.385	$2.332 \cdot 10^{-13}$	$1.12 \cdot 10^{24}$	$4.48 \cdot 10^{26}$

TABLE 3.3: see text.

The Nuclear Matrix Elements are crucial in order to correctly translate the experimental result into a value for $< m_\nu >$.
The experimental technique will be illustrated in the next chapter.

Chapter 4

The CUORE and CUORICINO experiments

4.1 Introduction : the bolometric technique

A bolometer is a solid state detector that measures the energy of an incident particle by the induced rise in temperature of the detector. Small energy depositions result in measurable temperature changes because at low temperature the heat capacity, C, of a dielectric and diamagnetic crystal of mass m and molar mass M behaves according to the Debye law as:

$$C = \frac{m}{M}\frac{12}{5}\pi^4 N_A k_B \left(\frac{T}{\Theta_D}\right)^3 \tag{4.1}$$

where Θ_D is the Debye temperature, which depends on the material [97]. The temperature change, given by $\Delta T = E/C$ for an energy deposition E, becomes large enough to be measured with high precision when C is made sufficiently small by cooling the detector to a very low temperature on the order of 10 mK.
Since most of the energy transferred from a particle to a detector is eventually converted into heat, a bolometer has a higher intrinsic resolution than other types of nuclear radiation detectors that measure the component of a particle's energy that goes into ionization or excitation of atomic electrons.
Aside from the possibility of energy loss due to excitation of metastable states in the lattice, the theoretical resolution of a bolometer is limited only by fluctuations in the *number* of phonons exchanged with the heat sink that maintains the bolometer's base temperature. An estimate of this thermodynamic and statistic limit on the resolution of a bolometer may be obtained by considering that the elementary excitation, the energy required to create one phonon, is about $\epsilon = k_B T$ so that the number of phonons in a bolometer with energy $E = CT$ is $N = E/\epsilon = CT/k_B T$. Assuming this number of phonons fluctuates according Poisson statistics, the variation in the energy is

$$\Delta E = \sqrt{N} \cdot \epsilon = \sqrt{k_B C T^2} \tag{4.2}$$

a quantity that is independent of energy. Plugging in typical values for CUORE bolometers ($C \approx 1MeV = 0.1$ mK and $T \approx 10mK$) yields an energy fluctuation. of $\Delta E \approx 10$ eV. While this value is impressive, roughly two orders of magnitude better than conventional detectors, it should be stressed that this is merely the thermodynamic and statistical limit on the detector technology. In a real detector, the energy resolution is degraded due to extrinsic sources of noise, and the contribution of Eq. (2.8) is negligible.

4.1.1 The CUORE bolometer module

CUORE and its predecessor experiments, including CUORICINO (about which I will discuss later in this chapter) and the Three Towers Test, are arrays of independent bolometer modules. A bolometer module consists of three essential parts: an energy *absorber*, a temperature *sensor*, and a Joule heater.

4.1.2 Energy absorber: TeO_2 crystal

The energy absorber is a TeO_2 crystal, which is also the source of double beta decaying ^{130}Te. For CUORE each crystal will be $5 \times 5 \times 5$ cm^3 with a mass of 750 g. The CUORICINO crystals were of two types: 44 were slightly larger with an average mass of about 790 g, and 18 were smaller, $3 \times 3 \times 6$ cm^3 and 330 g. A photograph of four $5 \times 5 \times 5$ cm^3 of the CUORICINO crystals is shown in Fig.2. The Debye temperature of TeO_2 is (232 ± 7) K [98].

FIGURE 4.1: Absorber in CUORICINO experiment, four $5 \times 5 \times 5$ cm^3 of the CUORICINO crystals

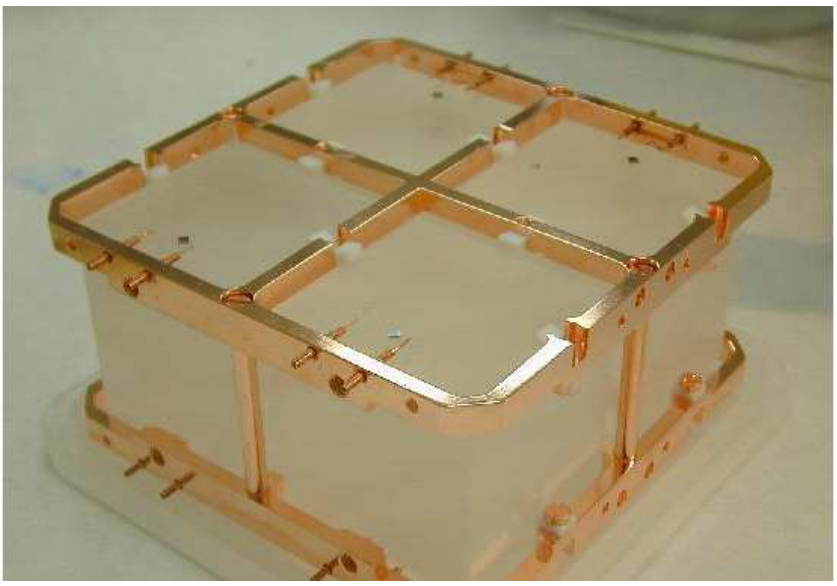

Crystals of tellurium dioxide are preferred over pure tellurium crystals because of their thermal and mechanical properties. Pure tellurium was tested as a bolometer, but the mechanical stress of thermal contraction caused excessive damage to the crystal [[99]]. Tellurium dioxide crystals, on the other hand, can undergo repeated thermal cycling

with no observable damage or decrease in performance as bolometers. Moreover, TeO_2 crystals have a higher Debye temperature than pure tellurium crystals, yielding a lower heat capacity and therefore larger pulse amplitudes at the same working temperature. Tellurium dioxide crystals are also advantageous because they are readily available from experienced commercial manufacturers due to their use as acousto-optic materials in industrial applications. The TeO_2 crystals for CUORICINO and CUORE were grown by the Shanghai Institute of Ceramics, Chinese Academy of Sciences (SICCAS).

4.1.3 Temperature sensor: NTD Ge thermistor

The temperature sensor that converts the thermal variation into an electrical signal is a neutron transmutation doped (NTD) germanium semiconductor thermistor. A semiconductor thermistor is a high resistance semiconductor with a doping density below the metal-insulator transition [[100]]. Conduction occurs when charges tunnel across the potential barrier between impurity sites. Different impurity sites have different energy levels, and the charges acquire or give up the necessary energy difference by absorbing or emitting a phonon. At low temperatures, with few high energy phonons available, charges may tunnel, or "hop" not only to nearest neighbor sites but over longer ranges in order to find a site with an energy difference matched to an available phonon. This conduction regime is known as *variable range hopping*. The resistivity of a semiconductor thermistor in the variable range hopping regime depends on its temperature as

$$\rho = \rho_0 e^{(T_0/T)^\gamma} \tag{4.3}$$

with $\gamma = 1/2$. The parameters ρ_0 and T_0 must be determined experimentally.
The NTD technique produces germanium thermistors with highly homogeneous concentrations of dopants and good reproducibility [[101]]. To produce an NTD Ge thermistor, a wafer of natural germanium (Fig. 2.10) is exposed to the thermal neutron flux from a nuclear reactor. Neutron capture reactions on the stable germanium isotopes create unstable germanium isotopes that subsequently decay to the desired dopant elements.

The nuclear processes that take place are:

$$\begin{aligned} &^{70}Ge(21\%) + n \rightarrow {}^{71}Ge(\sigma_T = 3.43 \pm 0.17b, \sigma_R = 1.5b) \\ &^{71}Ge \rightarrow {}^{41}Ga(\tau_{1/2} = 11.4d)Acceptor \end{aligned} \tag{4.4}$$

$$\begin{aligned} &^{74}Ge(36\%) + n \rightarrow {}^{75}Ge(\sigma_T = 0.51 \pm 0.08b, \sigma_R = 1 \pm 0.2b) \\ &^{75}Ge \rightarrow {}^{75}As(\tau_{1/2} = 83min)Donor \end{aligned} \tag{4.5}$$

$$\begin{aligned} &^{76}Ge(a.i7.4\%) + n \rightarrow {}^{77}Ge + \gamma(\sigma_T = 0.16 \pm 0.01b, \sigma_R = 2.0 \pm 0.35b) \\ &^{77}Ge \rightarrow {}^{77}As + e^- + \bar{\nu_e}(\tau_{1/2} = 11.3h)Donor \\ &^{77}As \rightarrow {}^{77}Se + e^- + \bar{\nu_e}(\tau_{1/2} = 38.8h) \end{aligned} \tag{4.6}$$

FIGURE 4.2: Germanium wafers used to make NTD Ge thermistors.

where σ_T and σ_R are the thermal and epithermal neutron capture cross sections, respectively. Since the neutron interaction probability is low, the entire volume of germanium is exposed to a nearly uniform neutron flux, leading to *very uniform* doping levels. The thermistors for CUORICINO were irradiated at the Missouri University Research Reactor (MURR), and the thermistors for CUORE were irradiated at the MIT Nuclear Reactor Laboratory (MIT-NRL).
After a waiting period of at least six months for the activity of the ^{71}Ge in the sample to decay to an acceptable level, the germanium wafers are cut into pieces to make individual thermistors. From Eq. (2.81) the resistance of a thermistor at temperature T is given by

$$R = R_0 e^{(T_0/T)^\gamma} \tag{4.7}$$

with $R_0 = \rho_0 l/A$ where l and A are the thermistor's length and cross sectional area, respectively. The thermistors are characterized by measuring their resistance as a function of temperature by gluing the thermistor to a low temperature heat sink with a high thermal conductivity epoxy. The temperature of the heat sink is varied and monitored with a calibrated thermometer. From a fit to the $R(T)$ data points, the parameters R_0 and T_0 are obtained. Characteristic values for CUORE thermistors are $R_0 = 1.15\Omega$ and $T_0 = 3.35$ K, corresponding to a resistance of approximately 100 M at 10 mK. A parameter quantifying the performance of a thermistor is the logarithmic sensitivity, η, defined by

$$\eta = |\frac{dlnR(T)}{dlnT}| \tag{4.8}$$

Using Eq. (2.81), the logarithmic sensitivity of a CUORE thermistor is given by

$$\eta = \gamma \left(\frac{T_0}{T}\right)^{\gamma} \tag{4.9}$$

which usually is in the range $2 - 10$.
The NTD Ge thermistor is glued to a TeO_2 crystal with Araldit Rapid epoxy. The glue is applied in nine spots, arranged in a 3×3 grid, of 0.5 mm diameter. The spacing between the thermistor and the crystal is 50 μm. Compared with a single large glue spot, this arrangement of nine glue spots reduces the mechanical stress on the thermistor due to differences in thermal contraction between the thermistor and the crystal. Mechanical stresses can affect the resistance of the thermistor and degrade its performance as a thermometer.

4.1.4 Joule heater

The third element of a CUORE bolometer module is a silicon resistor, glued to the TeO_2 crystal with the same Araldit Rapid epoxy used to bond the thermistor. The resistor is used as a Joule heater to inject a constant energy into the bolometer at regular intervals, usually once every 5 minutes. The resistor, typically $50 - 100$ k , is very stable with temperature and is pulsed with an ultrastable pulser [102]. The heat is injected over a very short time compared with the response time of the detector, simulating the energy deposition of a particle interaction. The heater pulses are used to obtain frequent calibrations of the gain of the detector, which varies with temperature. Using the heater pulses, the gain is stabilized as part of the offine analysis [103].

4.1.5 Bolometer operation

To read out the signal from the NTD Ge thermistor, the thermistor is biased with the circuit shown in Fig. 3.3. The biasing circuit consists of a voltage source

and two load resistors in series with the thermistor. The total resistance of the load resistors is chosen to be much greater than the resistance of the thermistor at the working temperature so that an approximately constant current $I = V_{bias}/R_L + R_{th}) \approx V_{bias}/R_L$ flows through the thermistor. The voltage across the thermistor, $V_{th} = IR_{th} \approx V_{bias}R_{th}/RL$, is proportional to the thermistor resistance. The thermal information contained in the thermistor resistance is read out by recording the voltage across the thermistor.
The optimal bias voltage is determined independently for each bolometer. As the bias voltage is increased from zero and current flows through the thermistor, power $P = IV_{th}$ is dissipated as heat in the thermistor. The Joule heating of the thermistor increases its temperature and decreases its resistance, a phenomenon known as electrothermal feedback. The $I - V$ relationship, or load curve (Fig.2.12), for the thermistor begins approximately linearly at low bias voltages where electrothermal feedback is negligible. As

FIGURE 4.3: Biasing circuit for an NTD Ge thermistor. and

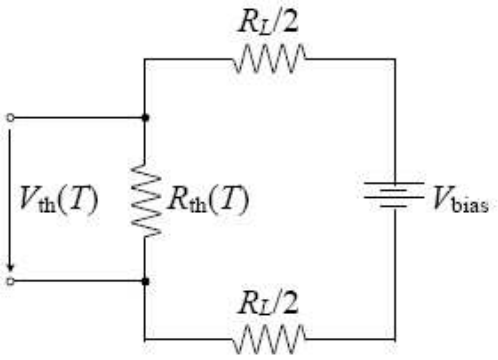

the bias voltage increases, the slope of the I-V curve increases until reaching the inversion point where the thermistor voltage is maximal. At higher bias voltages, the curve reverses direction, and the thermistor voltage decreases while the current in the biasing circuit continues to increase. The working point of the thermistor is a particular point on the load curve set by the bias voltage. The optimal working point is the one where the ratio of signal amplitude to noise level is maximized. Energy released in the crystal from particle interactions is dissipated as heat through a copper mounting structure, which is thermally linked to the mixing chamber of a dilution refrigerator. Since the crystals are large and the connection between the crystal and the copper frame has low thermal conductivity, the heat generated in a crystal by a particle interaction dissipates slowly, resulting in a temperature pulse with a characteristic decay time on the order of 1 second.

FIGURE 4.4: On the left, the load curve for an NTD Ge thermistor. On the right, measurements illustrating electrothermal feedback: As the power dissipated in the thermistor increases, the resistance of the thermistor decreases. The different curves were obtained at different base temperatures, i.e. the temperature at $P = 0$.

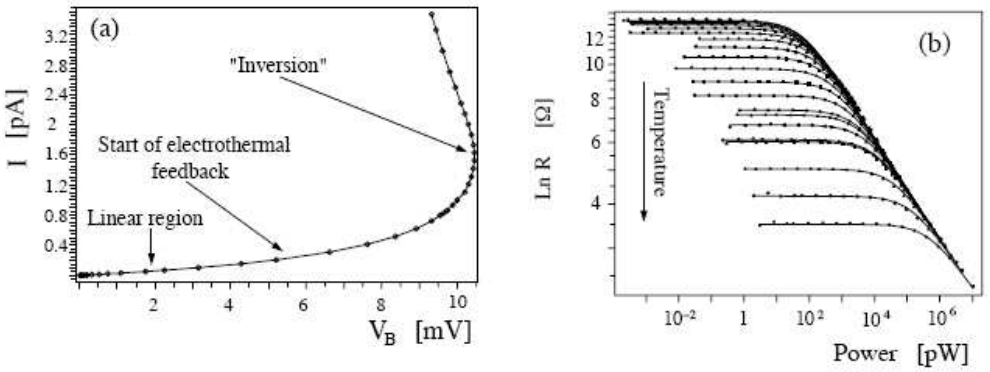

FIGURE 4.5: Superimposed on the load curve is the signal pulse height of a constant energy input from the heater as a function of the bias voltage for the NTD Ge thermistor. The bias voltage is optimized by choosing the value that maximizes the signal pulse height

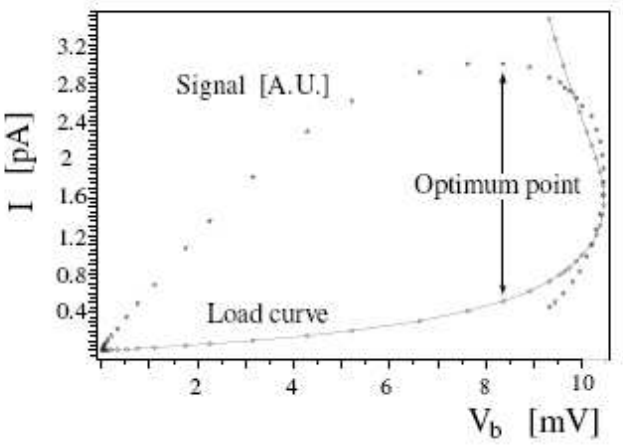

4.2 Bolometric experiments for neutrinoless double beta decay searches

Since Fiorini and Niinikoski first proposed the use of bolometers for rare decay searches in 1984 [104], members of the CUORE Collaboration have operated a series of $\beta\beta$ decay experiments based on the bolometric technique. Starting with a single crystal bolometer [105] , the detectors were increased in size to arrays of 4, 8, and 20 crystals [106], [107] , leading up to the recently completed 62−crystal CUORICINO experiment [108] Based on this experience, the CUORE Collaboration is currently engaged in constructing a much larger array, CUORE, which will consist of 988 crystals. In addition to the long-running experiments aimed at producing physics results, many short-time-frame *R&D* experiments have been performed with the primary goal of *reducing backgrounds from radioactive contaminations*.

4.2.1 CUORE

The CUORE experiment is a next generation ^{130}Te $\beta\beta0\nu$ decay experiment based on the experience with CUORICINO which will be discusse later in this chapter. It is funded by the INFN of Italy, the United States Department of Energy, and National Science Foundation of the United States. Infrastructure for CUORE is currently under construction in Hall A at LNGS next to the CUORICINO building, and components for CUORE are being manufactured around the world. The CUORE detector will be a tightly packed array of 988 TeO2 bolometer modules, each $5 \times 5 \times 5$ cm^3 and 750 g, for a total mass of 741 kg of TeO_2.
The bolometer modules will be arranged in 19 towers of 13 floors each, with 4 crystals per floor.

Each of the 19 towers is pretty similar to CUORICINO in size and arrangement.
The CUORE detector will be housed in a specially built cryostat and cooled to ≈ 10 mK by a pulse-tube-assisted dilution refrigerator (fig.2.14 (b)).

FIGURE 4.6: (a) the CUORE detector array and (b) the CUORE cryostat with the detector array inside.

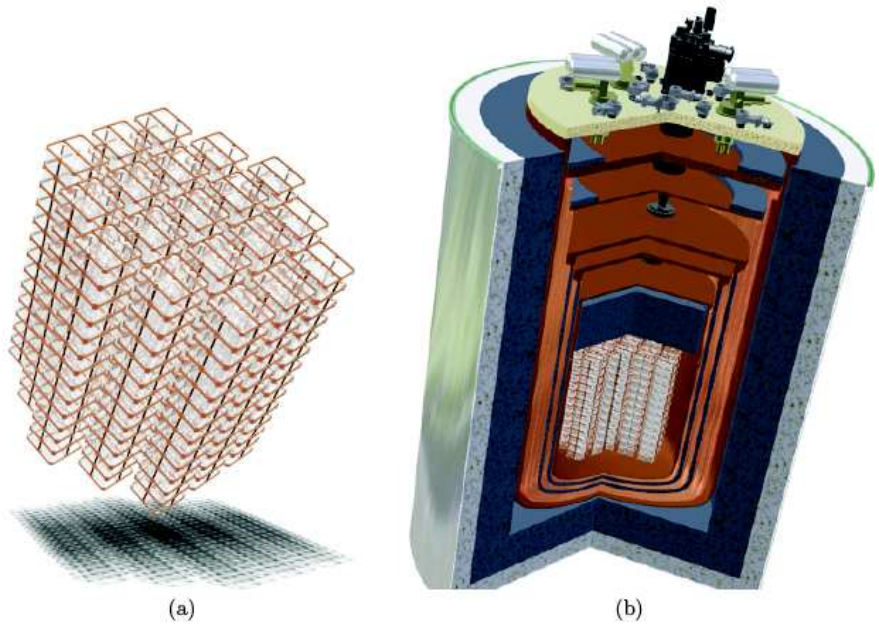

CUORE aims for a sensitivity of the order of 10^{26} y for the half-life for $\beta\beta0\nu$ decay of ^{130}Te in 5 years of running.

Collaboration has made an intense effort to understand and control the *sources of backgrounds* in CUORICINO and other cryogenic bolometer *R&D* experiments.

Improvements in the cleanling of materials and detector shielding lead to an expected background level for CUORE of 0.01 $counts/(keV \cdot kg \cdot y)$ in the region of interest around 2527.5 keV, which is the Q-value for the $\beta\beta0\nu$ decay. The main sources of backgrounds in CUORE are expected to be surface contaminations of the copper materials facing the crystals, bulk and surface contaminations of the TeO_2 crystals, and ^{232}Th contaminations in the copper radiation shields of the cryostat. External gamma, neutron, and muon induced backgrounds are estimated by simulations to contribute less than 0.01 $counts/(keV \cdot kg \cdot y)$. [109], [110]. Copper surface contaminations will be reduced by the *TECM* procedure, which is a cleaning technique tested and used at the LNL (Laboratori Nazionali di Legnaro. The production of radiopure TeO_2 [111] crystals has been the subject of extensive research and development by CUORE collaborators [111] . Dedicated production lines were set up at SICCAS for the growth and surface processing of CUORE crystals. Raw materials, reactants, consumables, ancillaries, and intermediate products used in the production of the crystals are screened for radioactive contaminations. The crystals are shipped from SICCAS to Italy by sea to minimize exposure to cosmic rays, and upon arrival at Gran Sasso, the crystals are immediately

stored underground. As a final quality control procedure, four crystals are randomly selected from each production batch (of approximately 60 crystals) to undergo a bolometric test in the CUORE *R&D* cryostat in Hall C of LNGS (Laboratori Nazionali del Gran Sasso). In the bolometric test, which lasts for a few weeks and is known as a CUORE Crystal Validation Run (CCVR), the crystals are operated as bolometers as they will be for CUORE and used to count their own radioactive contaminations. The bulk contamination levels of ^{238}U and ^{232}Th are measured (or upper limits set), and the bolometric performance is evaluated in terms of the energy resolution. All crystals tested up to now have met the CUORE specifications.
The CUORE detectors will be shielded from environmental radioactivity and radioactive contaminations of the dilution refrigerator by several layers of lead shielding both inside and outside the cryostat, with Roman lead constituting the innermost layer [111]. The cryostat radiation shields will be built from high purity copper that has been stored underground at LNGS to prevent cosmogenic activation; the copper material will be brought to the surface just in time for the construction of the cryostat. The cryostat and lead shielding will be enclosed within a neutron shield made of 10 cm thick borated polyethylene, which will be continuously flushed with dry nitrogen to exclude radon from the space near the detectors.
The geometry of the CUORE bolometer array provides an intrinsic advantage over a single tower like CUORICINO for rejecting backgrounds that deposit energy in multiple crystals. Many backgrounds, such as alpha decays near the surface of a crystal and Compton-scattered gammas, cause interactions in multiple crystals that are effectively simultaneous. An anti-coincidence cut will be highly effective at suppressing these backgrounds in CUORE. Furthermore, the inner crystals are shielded by the outer crystals.

Other advances in the CUORE design relate to the mechanical structure and assembly. The tower design has been optimized to reduce the amount of copper near the crystals. The NTD thermistors feature a new design for the electrical contacts, which will make the assembly of the bolometer modules much easier. The NTD thermistors for CUORICINO had electrical contacts on the sides, requiring the 50 μm signal wires to be bonded to a thermistor before the thermistor was glued onto a crystal. The fragile connections of the signal wires to the thermistors were prone to break during the procedure of gluing a thermistor to a crystal. For CUORE the electrical contacts wrap around from the sides onto the top of the thermistors, which allows a thermistor to be glued to the crystal first and the signal wires to be bonded to the top of the thermistor already attached to the crystal. The detector assembly will be carried out in a dedicated cleanroom in the underground laboratory. The bolometer modules and towers will be assembled in custom glove boxes flushed with nitrogen so that the crystals and other components of the towers do not come into contact with air. The final installation of the towers in the cryostat requires too large a space to be performed within a nitrogen environment and therefore will be performed in a section of the CUORE cleanroom containing nearly radon-free air supplied by an activated charcoal filtration system.
The CUORE goal for the energy resolution is 5 keV FWHM, which is a modest improvement over the 7 keV average for the CUORICINO $5 \times 5 \times 5$ cm^3 crystals. The improvement is due mainly to minimization of mechanical vibrations of the crystals. The CUORE crystals have more stringent tolerances on their dimensions than the CUORICINO crystals in order to ensure they fit snuggly in their holders, and the detector will be mechanically decoupled from the building structure, pumps, and cryocoolers by a carefully designed suspension system in order to suppress the propagation of vibrations

to the crystals. In addition to improving the average energy resolution, these improvements in crystal uniformity and mechanical vibrations are expected to lead to much less variation in energy resolution between different detectors compared with CUORICINO.

4.2.2 CUORICINO

Operated in the Laboratori Nazionali del Gran Sasso in the years $2003-2008$, CUORICINO was composed by a tower of 62 TeO_2 bolometers. The experiment was able to set a lower limit of $2.8 \cdot 10^{24}$ y for the $\beta\beta0\nu$ half life of ^{130}Te ($m_{\beta\beta}$ in the range $300-710$ meV). At present the CUORICINO results represent one of the most competitive limits for the effective Majorana mass, comparable with the ones obtained with Germanium detectors [112], [113]. Furthermore, it has been a unique test bench for the next generation CUORE experiment. The excellent performance obtained with CUORICINO demonstrates the feasibility of a ton scale bolometric experiment aiming at the investigation of $m_{\beta\beta}$ in the inverted mass hierarchy range.
In this section the experimental set-up, the analysis procedures, the detector performance and the physics results obtained by CUORICINO will be presented.

FIGURE 4.7: Typical energy spectra obtained in a few days calibration in CUORICINO. The top figure represents the spectrum for the $5 \times 5 \times 5$ cm^3 crystals while the bottom one is for the $3 \times 3 \times 6$ cm^3 crystals.

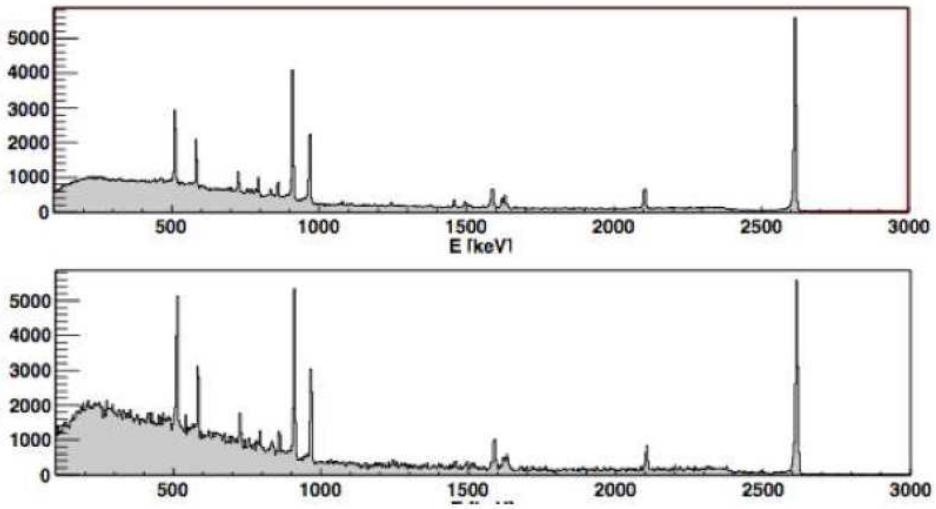

4.2.3 Experimental setup

CUORICINO is an array of 62 TeO_2 bolometers arranged in a tower of 13 floors (fig. 2.15). Eleven floors are made of four $5 \times 5 \times$ cm^3 crystals each , while the two remaining floors are composed by nine crystals $3 \times 3 \times 6$ cm^3 crystals each (fig. 2.15). All crystals have natural abundance of ^{130}Te (34%), apart for four $3 \times 3 \times 6$ cm^3 crystals: two of them are enriched in ^{130}Te (82%) and the other two are enriched in ^{128}Te (75%). The mass of the big crystals is of about 790 g, while the mass of the small crystals is 330 g.

The total detector mass is 40.8 kg (11.8 kg in 1^{30}Te).

The mechanical structure of the tower is made of OFHC Copper, and the crystals are fixed to it by mean of Teflon supports. The thermal pulses are read by neutron transmutation doped (NTD) thermistors, thermally coupled to each energy absorber. Since thermal drifts would induce variations in the response of the detectors, the tower is maintained at a constant temperature by a feedback stabilization circuit, fed by the signal of a thermometer that is attached on the mechanical structure of the detector [116]. Fine gain drift corrections are applied offline by exploiting the fixed energy thermal pulses that are injected every few minutes in the crystals [117]. These stabilization signals are generated by dissipating an electrical pulse of fixed energy on a Si resistor attached to each energy absorber. They have a time duration much shorter than the typical thermal response of the detector, and the produced signals have a shape that is almost indistinguishable from the ones produced by particle interactions. These signals, usually called heater pulses, are flagged by the data acquisition system and are used offline to correct gain fluctuations induced by temperature drifts.
About once per month a few days energy calibration is performed by inserting ^{232}Th sources between the cryostat and the external lead shields. Typical energy spectra obtained in calibration measurements are reported in fig. 2.16

All the materials used to construct the CUORICINO tower were selected after rigorous radioactivity checks and dedicated procedures were developed to clean them. The crystals were grown using previously tested low radioactivity powders by the Shanghai Institute of Ceramics (SICCAS) and were shipped to Italy by boat and stored underground to minimize activation by cosmic ray interactions. The cleaning procedures, as well as the detector assembly, were performed in a N2 atmosphere using glove boxes to minimize surface recontaminations.
The CUORICINO tower is hosted in a dilution refrigerator that allows to operate the detectors at a temperature of ≈ 8 mK. To avoid heating due to vibrations the tower is mechanically decoupled from the cryogenic apparatus using a stainless steel spring.
Several shields are used to minimize the background. The tower is surrounded by a 1.2 cm low activity Roman lead layer (^{210}Pb activity ≤ 4 mBq/Kg [118]) maintained at 600 mK to minimize the radioactive background coming from the cryostat radiation shields. The thickness of the Roman lead layer is increased to 10 cm on top of the detector in order to protect it from contaminations in the dilution unit. The cryostat is surrounded externally by two 10 cm thick lead shields. The background due to environmental neutrons is reduced by a 10 cm thick borated polyethylene shield. The cryostat is also surrounded by a box continuously flushed with clean N_2 to reduce Radon contaminations, and it is enclosed in a Faraday cage to avoid electromagnetic interference.

4.2.4 The single module

The CUORICINO detector has a modular structure, where the basic element is represented by a single floor. The design of the single module must satisfy stringent requirements concerning mechanical properties, thermal performances and radioactivity constraints. Thermal coupling between the crystals and the heat sink, as well as the ones with the NTD sensors, must guarantee a good performance of the detector.
At the same time the geometry of the various parts of the single module must be properly designed, preventing the differential thermal contractions from breaking the crystals. All

FIGURE 4.8: Photographs of the CUORICINO tower and two of the individual floors. On the top right is a floor of $5 \times 5 \times 5$ cm^3 crystals, and on the bottom right is a floor of $3 \times 3 \times 6$ cm^3 crystals.

.

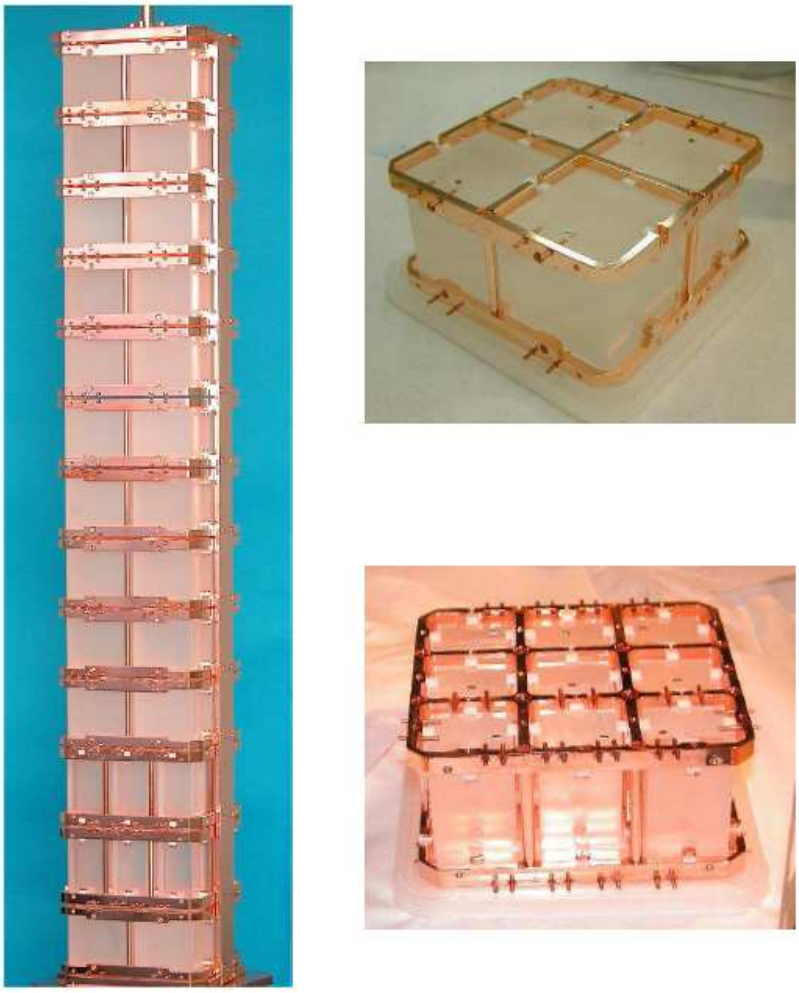

these requirements have to be met by using only those materials that were measured to have low enough radioactive contaminations. A detail of the CUORICINO single module is shown in fig. 2.18. It is composed by four $5 \times 5 \times 5$ cm^3 (or nine $3 \times 3 \times 6$ cm^3) crystals enclosed in a pair of OFHC copper frames which serve both as mechanical supports and thermal bath for the detectors. The two frames are connected to each other by four small columns, also made of copper.

The crystals are connected to the copper frames by small Teflon supports The NTD sensors are attached to the crystals using Araldit Rapid, Ciba Geigy epoxy glue.
The thermal conductance of the glue spots was measured experimentally and the phenomenological relation revealed to be $G \sim 2.6 \times 10^4 T^3$ $[W/K/spot]$ [119] , where T is in K. The same gluing technique is used to apply on each detector the Si resistor used to feed the crystal with heater pulses. Electrical connections for both the NTD sensor and the Si resistor are made with two 50 μm diameter gold wires, bonded to metalized

FIGURE 4.9: Sketch of the CUORICINO apparatus showing the tower hanging from the mixing chamber of the dilution refrigerator and the detector shieldings.

.

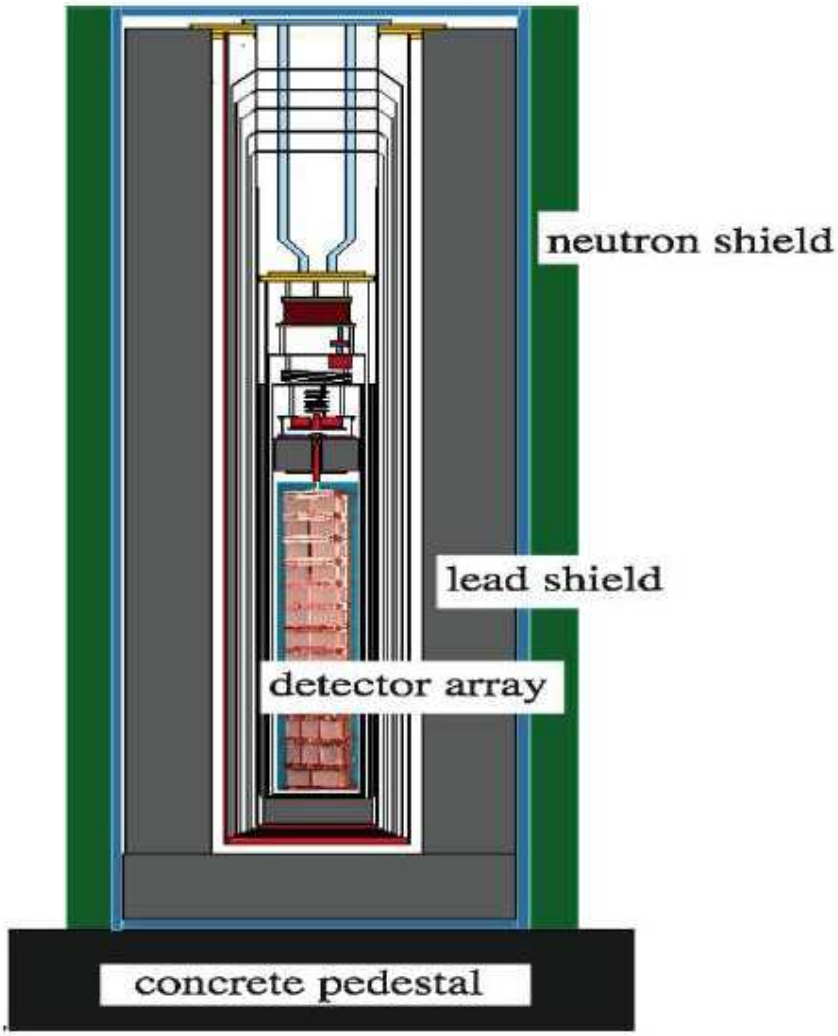

surface of the two chips. The wires are crimped on the opposite side into copper pins that pass through the mechanical structure of the single module.

4.2.5 CUORICINO background and $\beta\beta0\nu$ results

The CUORICINO data analysis proceeds through two steps. First level analysis aims at determining the energy and several pulse shape parameters associated to each raw pulse waveform recorded by the data acquisition system. Starting from these quantities, second level analysis allows to extract the physical informations that are relevant for the scientific goals of the CUORICINO experiment. I will discuss later on second level analysis.

FIGURE 4.10: Detail of the CUORICINO single module. The crystal is hold by OFHC copper frames which also represent the thermal bath for the detectors. In the picture the Teflon holders and the NTD sensor are also visible.

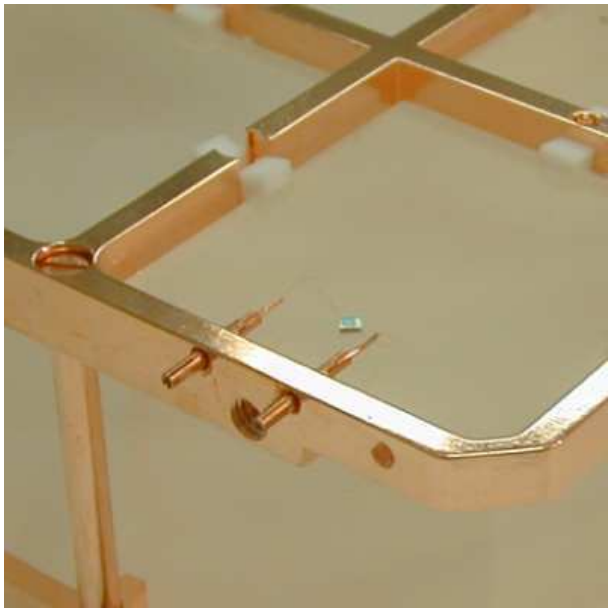

Second level analysis can proceed through different steps, depending on the physics goal of the analysis being performed. One could search for events contained in a single crystal, using all other detectors as active *veto*, or could search for coincident events in neighbor crystals; relative intensities of different γ peaks, or continuum counting rate in a given energy window can be studied to characterize different background sources. Here the attention will be focused on the search of neutrinoless double beta decay and the study of the background in the energy range where the signal is expected.

4.2.6 Data taking and detector performance

CUORICINO first data taking started in march 2003. Several wiring connection broke during the detector cool down procedure, so that only signals from 32 over 44 $5 \times 5 \times 5$ cm^3 crystals and 17 over 18 336 cm^3 crystals could be acquired. Since the active mass was anyway quite large ($\approx$ 30 kg of TeO_2) and the detector performance was satisfactory, data taking continued for few months. In November 2003 the tower was warmed up at room temperature to perform maintenance operations and to recover lost connections. Data taking restarted in may 2004 with the full operation of all detectors. This interruption set a marking point dividing the data taking in Run1 (prior to November 2003) and Run2 (from April 2004 to June 2008).
The performance of the detectors in the two runs was excellent. The best detectors had a resolution of 5 keV. Energy resolution was evaluated as the FWHM of the 2615 keV ^{208}Tl gamma peak observed in calibration measurements. Similar energy resolution was obtained from the ^{208}Tl line that was visible also in background measurements summed over long time periods. Excluding the interruptions for the maintenance of the cryogenic apparatus, the live time of the experiment was evaluated to be $\approx$ 70%.

FIGURE 4.11: Comparison between energy spectra before (dashed line) and after (continuous line) gain instability corrections. The two visible lines in the stabilized spectrum are due to γ's from the ^{232}Th calibration source.

.

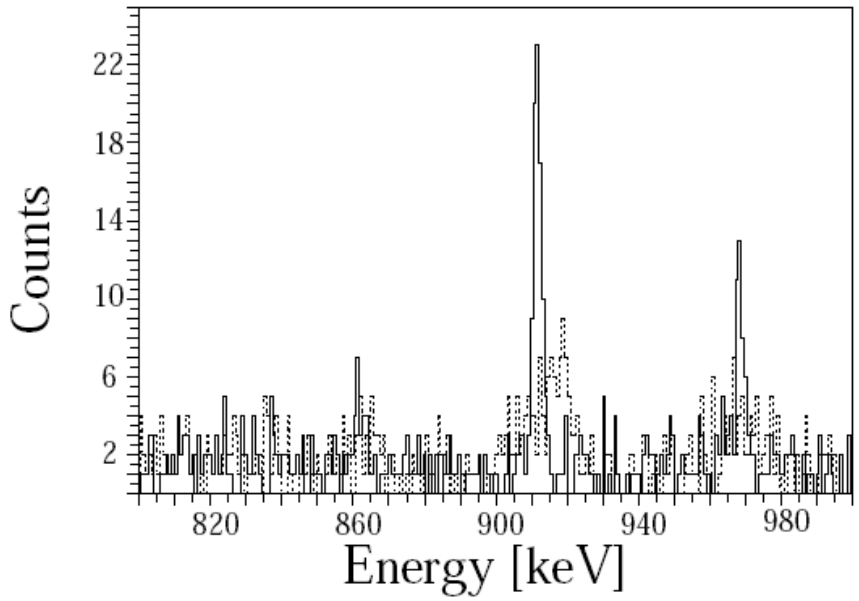

4.2.7 Background analysis

The background observed by CUORICINO can be grouped in two categories, depending on whether it comes from *outside* the detector (external background) or from the *detector itself* and the *passive materials* that surround it (internal background). External background is produced by neutrons, muons, and natural radioactivity in the underground laboratories. It can be reduced to a negligible level by proper detector shielding, as already discussed.
Internal background comes from the radioactive contaminations in the cryostat radiation shields, the mechanical structure of the tower and the crystals themselves. Apart for the most external cryostat radiation shields, from which the crystals are protected by a low radioactivity Roman lead layer, there is no way to protect the detector from the internal background sources.

The only available solution is to eliminate them by proper material selection and cleaning.

This is one of the guidelines of the *R&D* activity for the CUORE experiment. Figure 3.9 shows the background measured by the $5 \times 5 \times 5$ cm^3 crystals in CUORICINO. It was obtained by summing the single crystal energy spectra over the whole data taking of the experiment. The three histograms represent the single hit, double hit and total energy spectra. Single hit spectrum was obtained using the detector array as a veto, thus selecting events in which only one crystal was hit within a coincidence time window of ≈ 100 ms. Double hit spectrum was obtained from the requirement that two crystals

were hit in the same coincidence time window. The $\beta\beta0\nu$ detection efficiency has been evaluated using Monte Carlo simulations: in 86% of the cases the two emitted electrons are fully contained in the crystal where the decay occur. Therefore the $\beta\beta0\nu$ signal should appear as a peak at 2527.518 ± 0.013 in the single hit spectrum. Thus, the capability of operating the detectors in anti-coincidence allows to reduce the background. Due to the way in which the crystals are arranged, this reduction is not much effective for CUORICINO, but it will play a fundamental role in the tight-packed structure of CUORE.
Even in CUORICINO, by studying the differences between coincidence and anti-coincidence spectra it is possible to extract important informations concerning the nature and the location of background sources.

Source	^{208}Tl	$\beta\beta0\nu$	$3-4$ MeV
TeO_2 ^{238}U and ^{232}Th surf. cont.	–	$10 \pm 5\%$	$20 \pm 10\%$
Cu ^{238}U and ^{232}Th surf. cont.	15%	$50 \pm 20\%$	$80 \pm 10\%$
^{232}Th cont. in cryostat Cu shields	$85 \pm$ %	$30 \pm 10\%$	–

TABLE 4.1: Main contributions to the CUORICINO background. The values refer to the background in the $\beta\beta0\nu$ region, in the ^{208}Tl peak and in the region between 3 and 4 MeV.

FIGURE 4.12: CUORICINO background. The black histogram represents the total energy spectrum; the orange filled histogram is the anti-coincidence spectrum (a single hit in a coincidence window of ≈ 100 ms) and the blue filled histogram is the double hit spectrum (two events occurred in the same ≈ 100 ms time window).

.

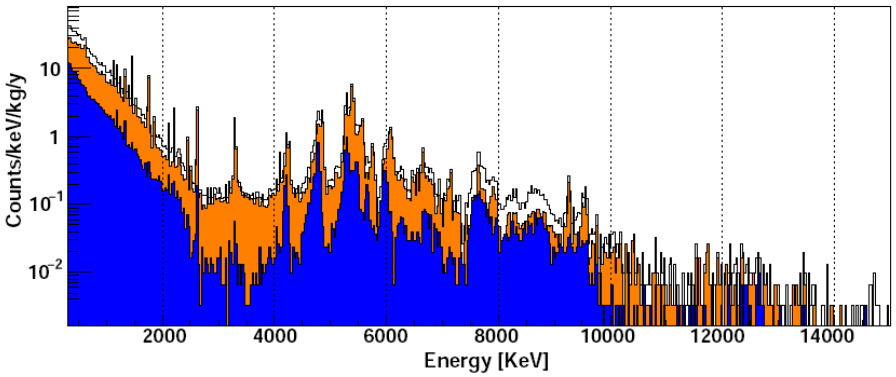

As shown in fig.2.20 the background differs by about 30%on the two side of the 2615 keV ^{208}Tl line. This line, from the ^{232}Th decay chain, is the highest γ line produced by environmental contaminations and is the only possible contribution (through Compton events) to the $\beta\beta0\nu$ background. The other two peaks appearing in the spectrum shown in fig. 2.20 are the 2448 keV line from ^{214}Bi, and the 2505 keV sum line produced by the interaction in the same crystal of the two γ's emitted in ^{60}Co β decay. Given the good energy resolution, events from these two peaks produce a negligible contribution to the $\beta\beta0\nu$ background.
By comparing the intensities of the ^{208}Tl gamma line with other lower energy γ's from the ^{232}Th chain it is possible to evince that the contamination is located relatively far from the detector, probably in some external cryostat thermal shield. Based on

$\beta\beta0\nu$ this guess on the source position, the contribution from the ^{208}Tl line to the background reported in tab. 2.4 was extrapolated using Monte Carlo simulations. The background counts measured by CUORICINO above, in energy, respect to the ^{208}Tl peak are produced mainly by degraded α particles from U and Th contaminations that are presumably located on the crystals and on the passive materials surrounding them. They produce a continuum in the energy spectrum that extends below the ^{208}Tl peak and thus contributes to the background in the $\beta\beta0\nu$ region. As shown in fig. 2.20, α peaks can be easily identified in the CUORICINO energy spectrum. From the study of their position and shape it is possible to extract informations on the location of the radioactive contaminants.
If the source is located within the crystals, both the α particle and the associated nuclear recoil release their energy inside the crystal and a sharp Gaussian peak is produced in the spectrum. In case the contamination is located on a very thin layer in the vicinity of the surface of the crystals or the passive materials, the α particle can escape retaining almost all its energy and can hit another crystal. Even in this case a Gaussian peak is produced, whose position is given by the energy of the α particle only (no recoil). If instead the surface contaminations are deep enough, even a part of the α energy is released in the material where the radioactive decay occurs. In case it is a crystal, a peak with an asymmetric long energy tail is produced.

FIGURE 4.13: CUORICINO background in the $\beta\beta0\nu$region. The black histogram is the single hit spectrum, while the blue filled histogram is the double hit spectrum. The $\beta\beta0\nu$ signal should appear as a peak at 2530 keV.

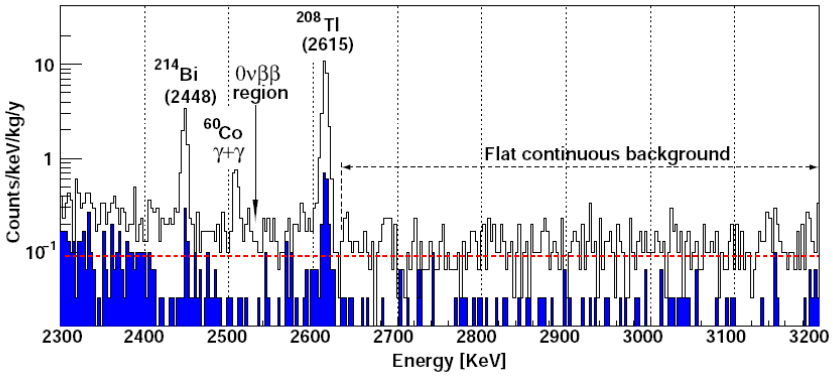

If instead the decay occurs on a passive material, only a flat continuum will appear in the energy spectrum. Besides the analysis of spectral shapes, further informations on the location of the contaminants can be extracted from the study of coincident events. In case they are located on crystal surfaces, there is a non negligible probability that the escaped particle is detected by a neighbor crystal. This would result in two detectors recording a signal at the same time and whose sum energy is equal to the total transition energy of the decay (α+ recoil). Obviously this feature is not present if the contaminant is located in the passive materials, as the fraction of energy that has been released in them cannot be detected. Examples of the characteristic features resulting from the different location of the contamination are shown in fig. 2.23.
In CUORICINO most of the α peaks in the region above 4 MeV are produced by U and Th surface contaminations. Some α peaks need dedicated attention:

- the α peak at 3200 keV is produced by an internal ^{190}Pt contamination of the crystals: the shape of the peak is Gaussian and no peak appears in the coincidence spectrum. The contamination is probably due to inclusions of fragments of the Pt crucible used in the crystal growth procedure;

- the α peak at 4080 keV, growing on the low energy tail of the 4270 peak, is attributed to a bulk contamination in Th, as was demonstrated by dedicated tests aiming at the reduction of the crystal surface contaminations;

- the α peak at 5300keV could be produced either by a contamination in ^{210}Pb or ^{210}Po. While ^{210}Po has a rather short half life ($\tau \approx 138$days), the half life of ^{210}Pb is much longer ($\tau \approx 22$ years). Therefore, since a decrease of the peak intensity was not observed in few years, this peak was attributed to ^{210}Pb. The position of the peak (it is centered at the energy of the α, and not α+ recoil) indicates that the contamination has to be on a very thin layer either on the crystal surface or on the passive materials surface. From the coincidence spectra and scatter plots it is then possible to conclude that at least part of the peak is produced by a contamination of the crystal surfaces.

- the α peak at 5400 keV was observed to decrease with time, in agreement with ^{210}Po half-life. Usually observed in recently grown TeO_2 crystals, this peak is produced by bulk contaminations, as it produces no events in the double hit spectrum. However part of the peak is a consequence of the U and ^{210}Pb surface contamination discussed above: when CUORICINO was started this peak was by far dominated by the bulk ^{210}Po contaminations, while now the peak has a much reduced intensity and the surface contamination seems to dominate.
  While the origin of the α peaks is rather understood, it is quite a complex task to characterize the continuous background that extends down to the $\beta\beta$ region. It is difficult to associate it to a particular α peak and to identify the corresponding contaminant. Based on measurements made before the construction of CUORICINO, and on several dedicated tests performed on the *R&D* apparatus, major contributions from neutrons and from the small parts of the detector can be excluded.
  Therefore most of the flat background measured by CUORICINO between 3 and 4 MeV should come from crystal and copper surfaces contaminations. Given the amount of events in the double hit spectrum in the $3-4$ MeV range, it is possible to conclude that a non negligible fraction of the flat continuum has its source outside the crystals.

FIGURE 4.14: CUORICINO background in the α region: single hit (black) and double hit spectrum (blue filled).

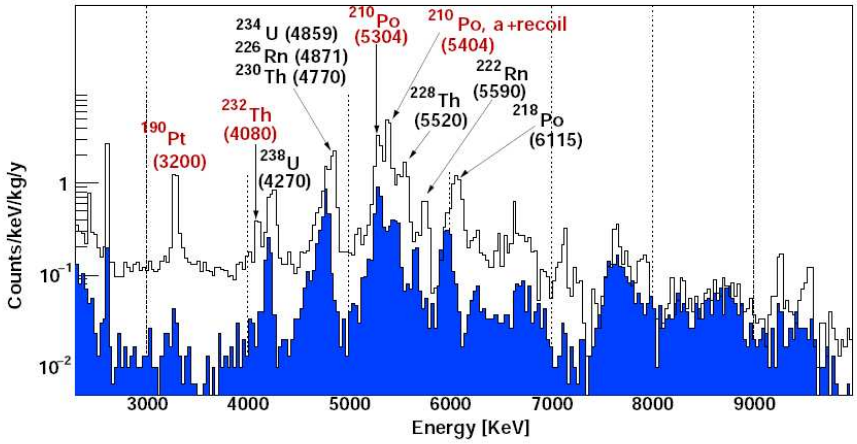

FIGURE 4.15: Alpha contaminations in CUORICINO. The top picture shows the Monte Carlo simulation of the single hit spectrum produced in CUORICINO by ^{238}U contaminations in the crystal bulk (black line), crystal surfaces (orange filled) and copper mounting surfaces (blue filled). Surface contaminations have been simulated with an exponentially decaying density profile and 1m thickness. The bottom left picture shows the possible α patterns in CUORICINO. The bottom right picture shows a scatter plot of coincident events for the crystal surface contaminations.

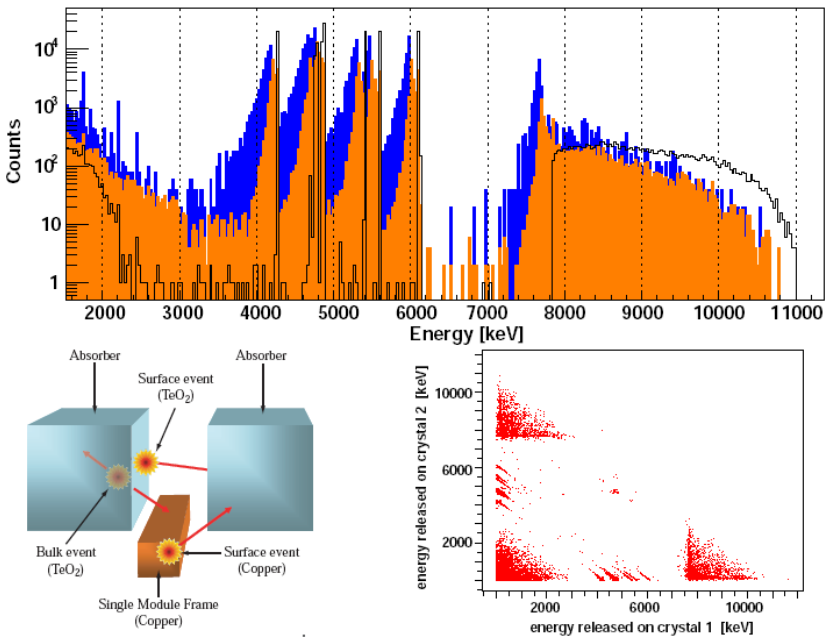

Chapter 5

The radioactive background study with Silicon Barrier Detectors

5.1 Introduction

In this chapter a complementary approach to the bolometric technique, to keep under control the radioactive level of the materials used to build the CUORE experiment, will be illustrated.
In particular the problem of α contaminations, which are potential candidates for the continuum background observed between 3-4 MeV region, will be discussed.

5.2 Alpha surface contamination

5.2.1 Radioactivity

Radionuclides in our environment are of three general types:

- primordial: these radioisotopes have lifetimes as long as the earths life ($4.5 \cdot 10^9$ y) and can belong to the natural decay chains of ^{238}U , ^{232}Th and ^{235}U Fig(5.1) and Fig(5.3) or be single isotopes as K and Rb.
- cosmogenic: by the interaction of the Cosmic Rays with terrestrial atmosphere and matter. Examples of cosmogenic isotopes are ^{3}H and ^{14}C.
- anthropogenic.

Of all the known isotopes only a few are stable and can be plotted as A (mass number) vs. Z (number of protons) as shown in Fig(5.2). All the unstable isotopes go through nuclear decays in order to reach a more stable configuration. There are three main decay channels: alpha, beta and gamma decay. I will discuss in the next section only α decay, which is under study trhough the device of Silicon Barrier Detectors (SBD).

FIGURE 5.1: ^{232}Th chain

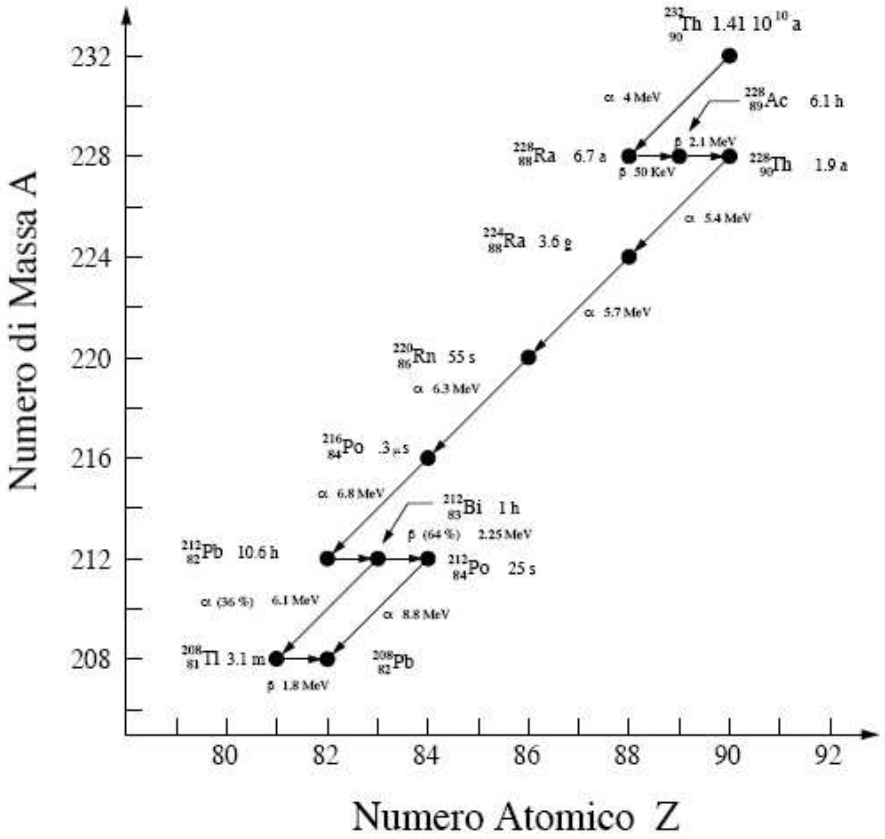

Many heavy nuclei are energetically unstable against the spontaneous emission of an alpha particle:

$$(A, Z) \rightarrow (A - 4, Z - 2) + \alpha \tag{5.1}$$

The alpha particles appear in one or more energy groups which are monoenergetic. For each distinct transition between initial and final nucleus a fixed energy difference or Q-value characterizes the decay. This energy is shared between the alpha particle and the nuclear recoil in a unique way, so that each alpha particle appears with the same energy given approximatively by $Q(A-4)/A$.

Alpha particles and the corresponding nuclear recoils loose energy rapidly in materials and stop in few microns. If the decaying nucleus is on a very thin layer near the surface of the material, the alpha particle (or the corresponding nuclear recoil) can be emitted from the surface and hit a faced material, with a *continuum energy spectrum* that extends down to low energies. For this reason surface contaminations of the materials facing a bolometric detector can be a very dangerous source of background.

FIGURE 5.2: Plot of the stable isotopes.

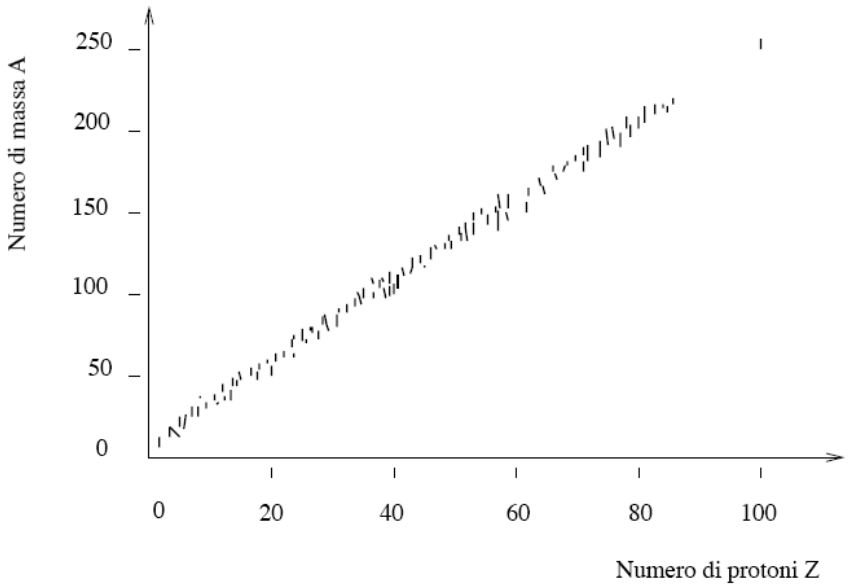

5.2.2 Alpha contaminations measurements

Even if most of the background observed in CUORICINO is rather understood, the continuum background above 3 MeV is not fully figured out.
One potential responsible, which can contribute to the unwanted counts, are alpha surface contaminations of the detectors or of the materials directly faced to them.
Unlike other solid-state detectors, bolometers are not ionization but phonon (or thermal) detectors. As a consequence, they are almost equally sensitive to any kind of particle interaction despite the way the energy is released. This means electrons, alpha-particles and nuclear recoils, depositing in the detector the same amount of energy, produce a pulse with the *pratically* same amplitude (and shape). The origin of some of the α peaks is rather understood, it is quite a complex task to characterize the continuous background that extends down to the $\beta\beta0\nu$ region. It is difficult to associate it to a particular α peak and to identify the corresponding contaminant. In this context the dedicated mesurements with Silicon Barrier Detectors (SBD) play a complementary role respect to the bolometers measurements; they give the opportunity of isolating the alpha contaminations contribution to the observed background, of ruling out some detector components as responsible of the continuous background and thus of *screenig* and *selecting* the materials which will be used to realize the experimental CUORE facility.

5.3 Silicon Barrier Detectors

At the Radioactivy Laboratory of the Univesity of Milano Bicocca, dedicated measurements with SBD were perfomed, to investigate the origin of the flat background measured

FIGURE 5.3: ^{238}U chain

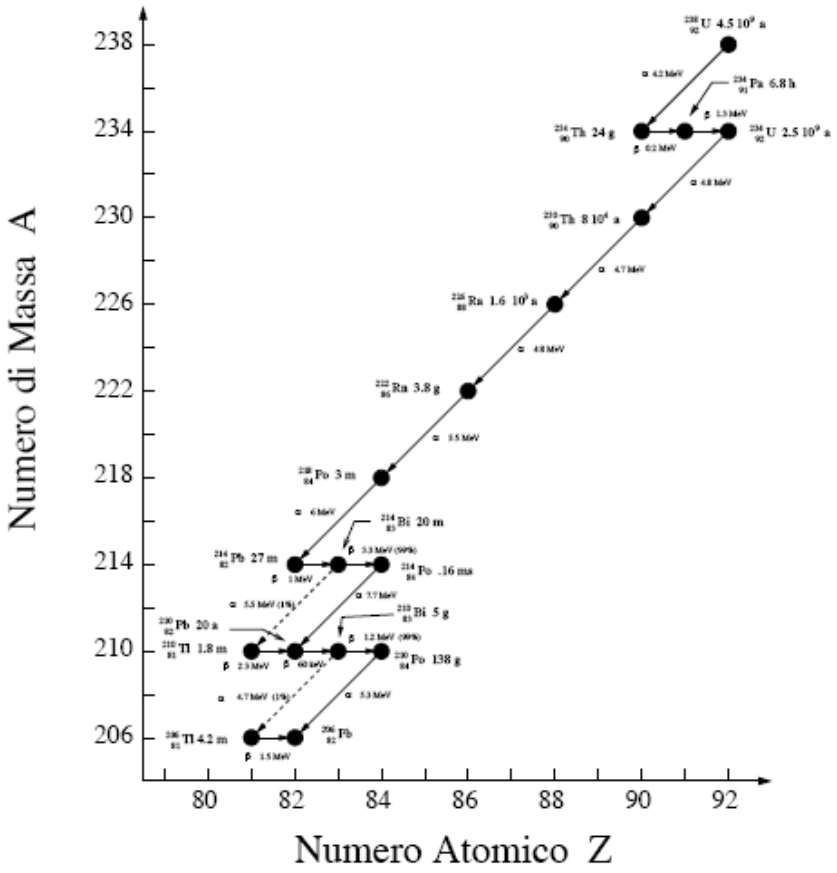

by CUORICINO. Silicon Barrier Detectors are semiconductor detectors. In this kind of material the main charge carriers are electron-holes pairs created along the path of charged particles (primary or secondary radiation) in the detector: their motion, in an applied electric field, generates a current in the detector related to the *energy* released. The SBD are suitable for heavy charged particle (like α's) spettroscopy, given they have a thin entrance window (50 nm) which lets the incoming particle to reach the active detector's volume with few energy loss in the dead layer.
A potential disadvantage of these detectors is their sensibility to light: the thin entrance windows are transparent to photons striking the detector which can reach the active volume. The energy of visible light ($2 - 4$ eV) is larger than most of bangap semiconductor, and electron-hole pairs can be produced by photons interactions.
A high level of noise may have generated from the normal artificial light indoors, but the detector's closure in vacuum chambers, needed for many applications with charged particles (and hence α spectroscopy), reduces the light-induced noise to negligible level.

FIGURE 5.4: Plot of the stable isotopes.

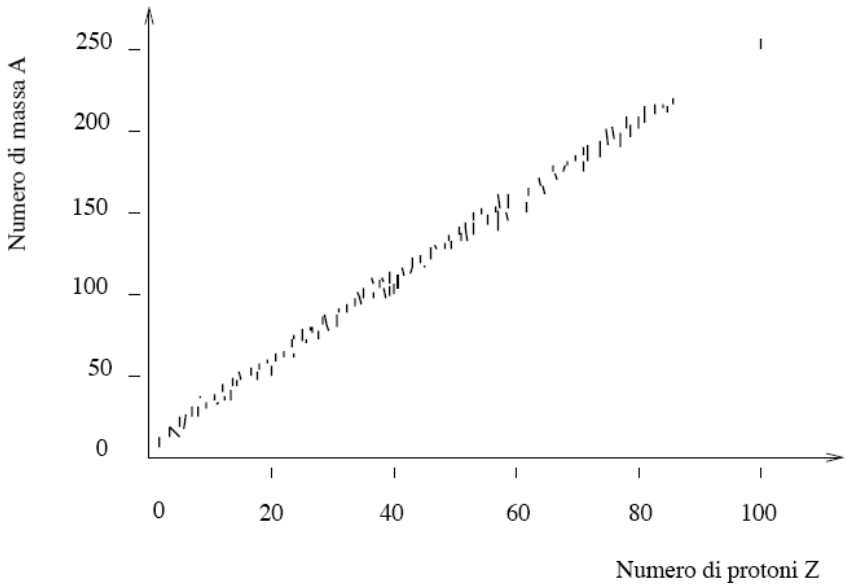

5.3.1 Operating Principle

In the detection process, particles are stopped in the depletion region, forming electron-hole pairs. The energy necessary to form a single electron-hole pair depends on the detector material, but is essentially independent of the energy of the incoming particle. The number of electron-hole pairs ultimately formed is thus directly proportional to the energy of the particle. The electric field in the depletion region sweeps the electrons to one terminal and the holes to the other. The resultant charge pulse is integrated in a charge sensitive preamplifier to produce a voltage pulse. The thickness of the depletion region depends upon the applied bias voltage, so that higher voltages give a thicker region, capable of stopping more energetic particles. The capacitance of the detector is given by:

$$C \sim w^{-1} \tag{5.2}$$

where W represents the thickness of the detector and is given by:

$$W \propto \sqrt{\rho V} \tag{5.3}$$

V is the applied bias in Volts and ρ the resistance in ohm/cm. It is thus possible to have a partially depleted or a fully depleted detector with and without overvoltage.

The noise level of charge-sensitive preamplifiers is usually given by the manufacturer as a certain value for zero input capacitance. The noise level increases with capacitance and this rate of increase is also specified. The detector capacitance is reduced at higher voltages, so that the lowest noise and best resolution are obtained at higher voltages

FIGURE 5.5: Thickness W of the depletion layer as a function of applied bias a: partially depleted detector, b: fully depleted detector. c: fully depleted detector with overvoltage

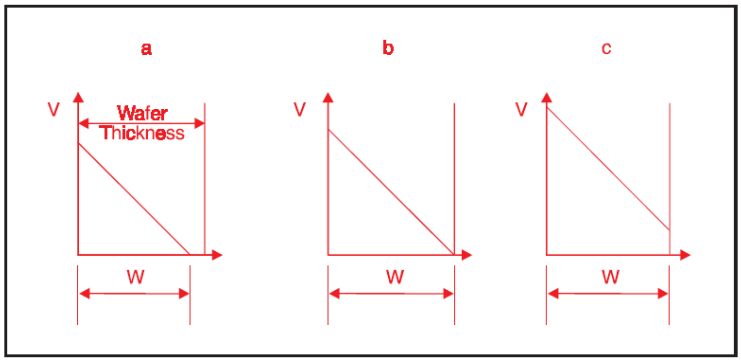

within the recommended range. At voltages above that recommended by the manufacturer, the reverse leakage current will likely increase, causing excessive noise and a loss of resolution.

5.3.2 Key Properties and Applications

Silicon Barrier Detectors were optimized for Alpha particle detection and Alpha Spectroscopy applications which require high *resolution*, high *sensitivity* and low *background*. High resolution is achieved by maintaining a uniformly thin entrance window over the detector surface and by reducing leakage current and noise. Alpha resolution of 17 keV (FWHM) is routinely achieved for a 450 mm^2 active area detector.
High sensitivity is enhanced by the thin window and ensured by depletion depth of about $100 - 120$ microns which will absorb Alpha particles of up to 10 MeV thus covering the complete range of all natural Alpha emitting radionuclides.

5.3.3 Factors Influencing Resolution and Efficiency

The main factors which influence the SBD energy resolution and efficiency are:

- **Detector-Source Distance** .When a source approaches the detector, line broadening (FWHM) is expected, as the mean slope of the alpha particles entering the detector is increased, resulting in an effectively increased thickness of the entrance window and subsequent higher energy straggling. For SBD this *energy straggling* is minimized due to the very thin entrance window of ≈ 50 nm.
- **Source Thicknes**. Sources must be homogeneous and thin in order to avoid energy straggling due to self-absorption. Self-absorption is proportional to the thickness of the source and inversely proportional to the specific activity..

5.3.4 Factors Influencing Contamination and Stability

The main factors which influence contaminationa and stability are:

- **Particulate and Recoil Contamination**. Contamination of detectors can take place when particles from sources gravitate to the detector surface and stick there or are splattered, sputtered, or splashed on the detector surface by the recoil energy imparted to the nucleus of an Alpha-emitting atom. In the latter case the energy of the particulates may be sufficient to implant them in the detector so that they cannot be removed nondestructively. Fortunately, much of the casual contamination can be removed from detectors by cleaning with a cotton ball saturated with acetone. Recoil contamination is almost never 100% removable so it is best avoided by careful sample preparation.
- **Stability**. Both long-term and temperature stability are important in detectors used for Alpha Spectroscopy because count times are many weeks and gain shifts during data accumulation lead to erroneous or unusable spectra.
- **Temperature Stability**. The leakage current of silicon diodes depends on the ambient temperature.

5.4 SBD at the Radioacivty Laboratory: optimization of the detecting system

At the radioactivity laboratory of the University of Milano Bicocca there are four active measurement lines: of the four SBDs, two of them have an active surface of 900 mm^2, while the other two of 1200 mm^2.
The measurement chain was optimezed during my PHD:

- The **radioactive backround** was lowered.
- the detection **efficiencies** were correctly modeled by the means of Monte Carlo simulations;
- a specific acquision, **DAQ**, was realized which allows to have decay time informations.
- several **measurements** were performed and their analysis gave useful results for the selection of the matearials which will be used for the CUORE experiment realization.

5.4.1 Cosmic Rays contribution to the backgrund

In this section I will describe the link between the SBD measurements, at the sea level, and the secondary cosmic rays interactions with the detecotors.
The observation of the energy released in the alpha decay of radioactive materials may in fact be masked by the interaction between the detector used and muons which, from

FIGURE 5.6: A picture of a vacuum chamber where the SBD's are operated. From the top: on the left there is the bias control, on the right there are some status control leds (to check leak curent as well as vacuum level...). In hte center there is the chamber with a silicon detecor inside faced to a copper sample.

cosmic rays through the atmosphere, strike the detector. It is therefore necessary and fundamental to measure the *background* generated by these particles, in order to have a *truthful* alpha decay spectrum. From cosmos several particles reach the terrestrial atmosphere with an average energy of about 2 GeV and some of them even of the TeV order: these are the cosmic rays and they are usually divided in *primary* and *secondary* cosmic rays.

The *primary* cosmic rays (CR) reach the stratosphere directly from cosmos They have an interaction path of 80 g/cm^2 and an absorption path of about 120 g/cm^2. Though the atmosphere thickness is of ≈ 1000 g/cm^2 (8 absorption paths) the CR interact several times before reaching the soil and they come in a reduced quantity.
The primary CR composition is: 87% protons, 11% He nuclei (α particles), 1% complex nuclei with $4 \leq Z \leq 26$, mainly Fe, Ni and Co, high energy electrons, neutrons and neutrinos.

The Cosmic Rays origin is not completely clear, it is common place to think they come from supernovae explosions or from binary stars.

The differential Energy distribution of primary CR is:

$$\frac{dN}{dE} \propto E^{-2.5} \tag{5.4}$$

it quikly decreases with energy.
For very high energy (E $\geq$ 10 GeV) CR the angular distribution respect to earth is isotrope. Less energetic CR (E $\approx$ 2 GeV) are deflected by galactic and extragalacti fields ($B \approx 0.4$ Gauss) which lead to wide deflections, due to the long distances crossed.

The *secondary* CR are produced by interaction of primary CR in the atmosphere.
The high energy CR mainly generate pions $\pi^{\pm}$. The multiplicity with which they are produced is $\sim 2E(GeV)^{1/4}$ and thus the number of created mesons grows slowly with E.
Moreover other particles are produced (K and p) following: 1 (π), 10^{-1} (K), 100^{-1} (p).
Charged pions show a relatively high cross section, they have a short life time ($\sim 10^{-8}$ s) and they decay in charged **muons** and muonic neutrinos.
Neutral pions decay into gammas and they thus generate electromagnetic showers, e^+ e^-, which can then generate X and γ rays etc.
The muons generated by charged pions electromagnetically decay with $\tau \sim 2.2$ μs, giving more electronic and muonic neutrinos. The number of muons which reach the earth is *more* than the pions which generated them because of the longer lifetime and the less interaction probability.
Muons are difficult to shield, thus they play an important role in low activity reseaches. Muons lose their energy in the rocks, through ionization, Bremsstralung interactions, nuclear reactions, with an average path of $\sim 2kg/cm^2g$.

FIGURE 5.7: The Bethe-Bloch curve relative to muons in copper. When particles, such as a muon, travel through a material they lose energy because of interactions with the electrons of the material. Interactions with the nucleus are negligible because of the relative size of the nucleus to that of the electron cloud. This energy is lost when the muon ionizes the atoms. The energy lost is described by the Bethe-Blocke equation. It is clear the minimun of the energy loss is approximately around 2-3 MeV.

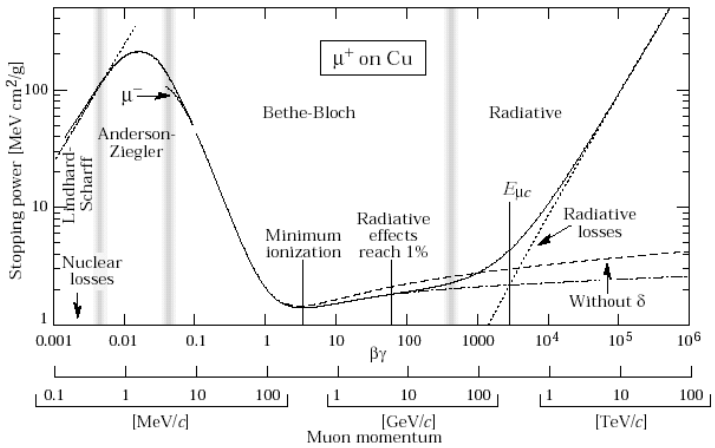

Considering the muons, once known the detector's density, the thickness crossed by the particle and its energy, it is possible to have a preliminary estimate of the energy released ΔE in the absorber, using the Bethe Block formulae for dE/dt and assuming the particle to be MIP (Minimum Ionizing Particle) $dE/dt \approx 2-3 MeV \cdot cm^2 \cdot g^{-1}$ with $t = \rho \cdot x$:

$$\Delta E \approx \int_0^x \left(\frac{dE}{d\rho \cdot x}\right)_{AVG} \cdot x \; dx \tag{5.5}$$

where ρ is the absorber density, x is the absorber thickness (100-120 μm) and $\left(\frac{dE}{d\rho \cdot x}\right)_{AVG}$ is the stopping power averaged on the particle energy.

With the goal of evaluating the CR contribution to the observed backgournd with SBD.

- I. An analytical and geometrical model was realized.
- II. A numerical model was realized.
- III. Anticoincidence measurements were performed.

As it will be illustrated later, I. and II. do not contemplate showers contribution which play the most important role in the observed background. For this reason a dedicate measurement, with an anticoincidence apparatus, was realized, with the aim of measuring the actual Cosmic Rays contribution to the acquired α spectra.

5.4.1.1 Analytical-Geometrical model

An anlytical model was realized to represent the muon's path inside the detector.
Once known the azimuth θ and polar ϕ angles for the incoming particle and once known the distance r from the center of the SBD it is then possible to calculate the distance $l(r, \theta, \phi)$ which is crossed by the muon inside the detector.

FIGURE 5.8: Azimuth θ and polar ϕ angles in the model

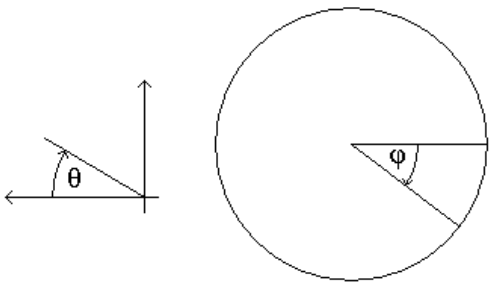

The expression for the angles are:

$$\begin{aligned} \theta_{l-MAX}(r) &= \arcsin\left(\frac{d}{\sqrt{D(r,\phi)^2+d^2}}\right) \\ D(r,\phi) &= \sqrt{r^2+R^2-2\cdot r\cdot R\cos\gamma} \\ \gamma &= \pi-\phi-\arcsin\left(\frac{r}{R}\sin\phi\right) \end{aligned} \tag{5.6}$$

where R is the detector (disk) radius ($R = 1.693$ cm), d is the thickness-height (120 μm). The expression for the path inside the detector is:

$$l(r,\theta,\phi) = \begin{array}{ll} \frac{D(r,\phi)}{\cos\theta} & 0 \le \theta \le \theta_{l-MAX} \\ \frac{d}{\sin\theta} & \theta_{l-MAX} \le \theta \le \pi/2 \end{array} \tag{5.7}$$

where θ_{l-MAX} is the azimuth angle which corresponds to the maximum path indide the detecotr (modelized as a disk).

With the analytical model a numerical model was developed too. The Monte Carlo simulations were run and gave plausibile results for the muon's incoming direction distribution. Again Monte Carlo simulations were used to calculate the energy release in

FIGURE 5.9: Plot of the Monte Carlo simulation output. The two plots are the ϕ and θ distribution and correctly describe the expected trend. The ϕ-distribution (polar angle) is uniform, while the θ-distribution reflects the $\cos^2\theta$ trend, which is the one assumed for the incoming muons on earth.

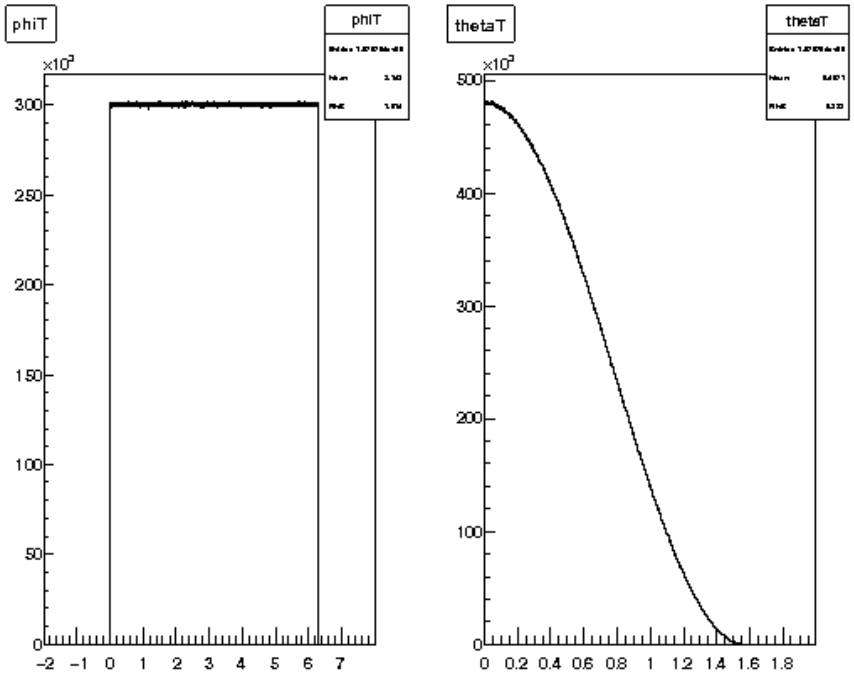

the detector. The simulation's result indicates that the most probable path is the almost

vertical one, as expected, thus only relatively small amounts of energy are expected in the experimental spectra.

FIGURE 5.10: Fit of the experimental spectrum, obtained with a coincidence measurement between a SBD and the organic scintillator. Fit of the **experimental** spectra The fit i performed: in the low-energy region ($\leq$ 300 keV, first plot from the left) and in an intermediate energetic region (up to $\sim$ 1600 keV, second and third spectra from the left). The first fit is a scaled exponential behaviour, $e^{-\alpha x} \cdot \beta$ which models the muons contribution. The second spectra is the sum of muons plus showers contribution, $e^{-Ax} \cdot B + e^{-Dx} \cdot C$ which agrees with the data. The third fit does not model the data at relatively high energy because it does not contemplate the shower contributions, but it is a simple scaled exponential which describes well the data at low energies (below the 'maximum' limit , see text).

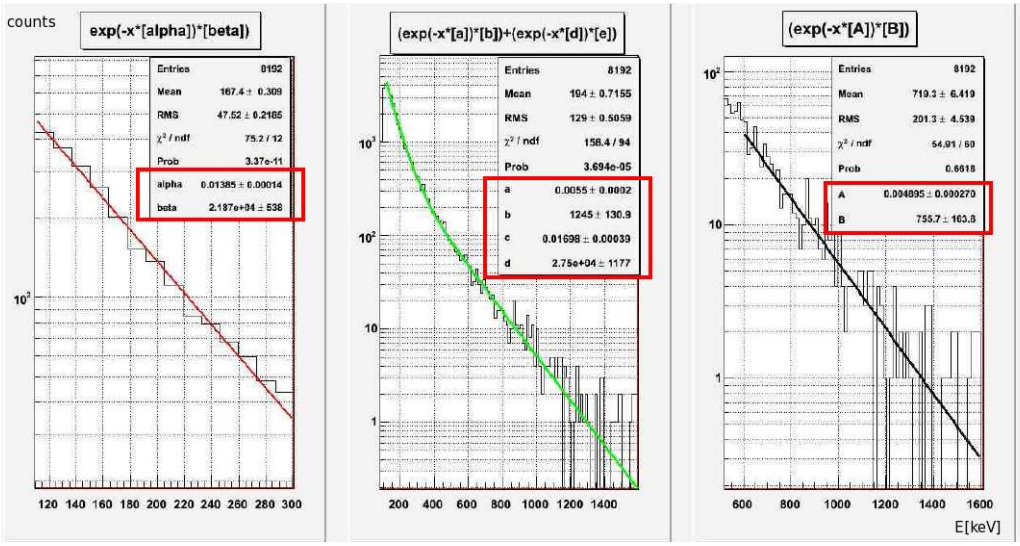

To test the realized models, anticoincidences measurements were performed. The measurements, as already mentioned, were performed with an organic scintillator (wich offers a fast time response) and a SBD.
With the geometrical information the upper limit for the muon's energy released in the SBD calculated is 250 keV.
In the anticoincidence measurements there are counts above the calculated limit, which is a clear indication that not only muons give contribution to the background spectra, but cosmic showers too.
The fit of the **experimental** and **simulated** data was performed. As hown in (Fig.3.10), different models were tested. The analytical functions assumed are:

- A scaled exponential $e^{\alpha x} \cdot \beta$, which describes the muons contribution to the background counts. The parameter β is a scale factor, while the α parameter (calculated from the fit) describes the 'behaviour'. This model works for the low energy part of the spectrum (muons), but it doesn't for higher energies, because it can't incorporate alone the muons and showers contributions.

- A sum of scaled exponetials $e^{Ax} \cdot B + e^{Cx} \cdot D$ which is the combination of muons and showers contribution. One addend is for low-energy ($\leq$ 250 keV - muons portion)

and the other is for higher energies ($\geq$ 250 keV - showers portion): obviously the parameters (A-C and B-D) are different for the two exponentials which describe different behaviours (just one addend is not enought to describe the process).

Thus the counts above the limit of 250 keV is due to electromagnetic showers interactions. The latter are created by the colliding muons with the structures which are above the silicon detectors. From these collisions several particles are created which are not MIP (Minumum IOnizing Prticles), which give counts in the acquired spectra which are at highter energies respect to the generating muons.
This moreover explains why the SBD show almost the same spectra at higher energies, even if they are placed at different locations, given the angles for shower distribution is wider than the muons one.

FIGURE 5.11: Comparison between a SBD experimental spectrum (in light green, obtained with the coincidence between the SBD and the organic scintillator) and three Monte Carlo simulation. The detector threshokd is higher than the simulated one. It is possible to appreciate the fact the simulations does not explain the background above the calculated upper energy limit.

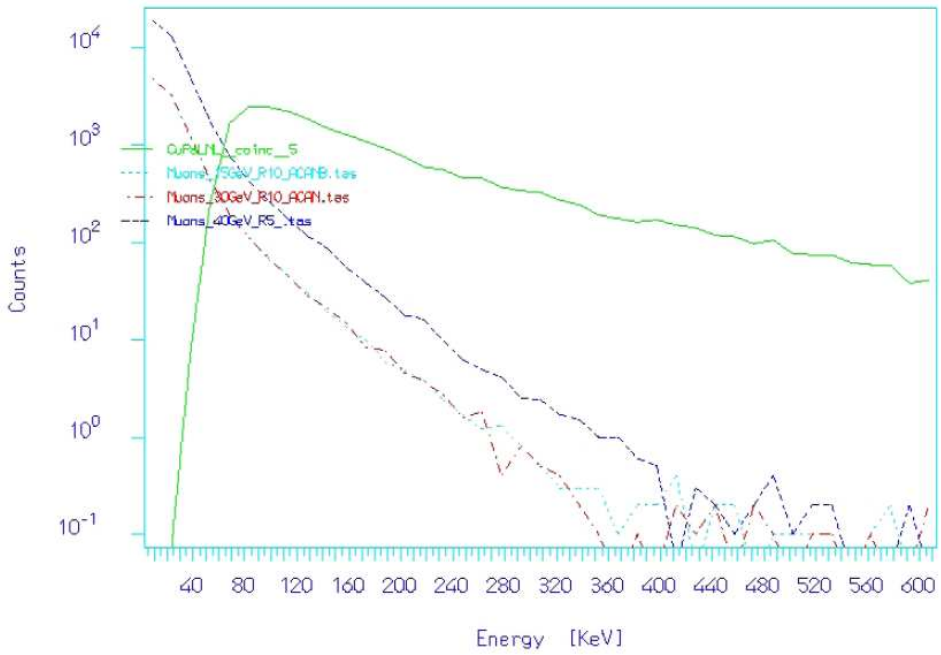

5.4.2 Coincidence measurements

The only way to evaluate the showers contribution is to experimentally measure their contribution to the acquired spectra, though it is pretty difficult to describe the showers with the device of numerical methods.
For this reason dedicated measurements were performed.
For the acquisition of data on muons from cosmic rays the four SBDs were used, in coincidence with an organic scintillator. The measurement time is was about 72 hours. The organic scintillator is placed above the four detectors: whenever it detects an event,

which is clearly due to CR interaction, a time gate is generated during which the SBD is ready to acquire a signal. The obtained is then the energy spectrum released by cosmic rays in the silicon.

The whole spectrum is the superimpostion of the muons and showers distribution described by: $e^{Ax} \cdot B + e^{Cx} \cdot D$. The calculated parameters (with the experimental and simulation data) were compared and the results are:

- At high energies the data dissagree, as expected, because the Monte Carlo simulation don't contemplate the EM showers.
- The parameters which give indication of the paths distribution inside the detectors ($A\&C$) are compatible within two sigmas.
- The scale factor ($B\&D$) are not compatible, as expected, because the event's number is clearly different.

All the described background counts can be eliminated by anticoincidences measurements.

FIGURE 5.12: Fit of the **simulated** spectra obtained as output of the Monte Carlo simualtion programm. Giving as inputs the minimum and maximum energy of the incoming muons, the program gives the the energy distribution spectrum. The fit is performed: in the low-energy region ($\leq$ 300 keV, first plot from the left) and in an intermediate energetic region (up to $\sim$ 1600 keV, second and third spectra from the left). The first fit is a scaled exponential behaviour, $e^{-\alpha x} \cdot \beta$ which models the muons contribution. The second spectra is the sum of muons plus showers contribution, $e^{-Ax} \cdot B + e^{-Dx} \cdot C$, the third is again a scaled exponential. As it is clear from the plots the assumed models do not work for the spectrum energy region which receives contributions from the showers, thought this contribution is not simulated, but only the muons are contemplated in the Monte Carlo simulation.

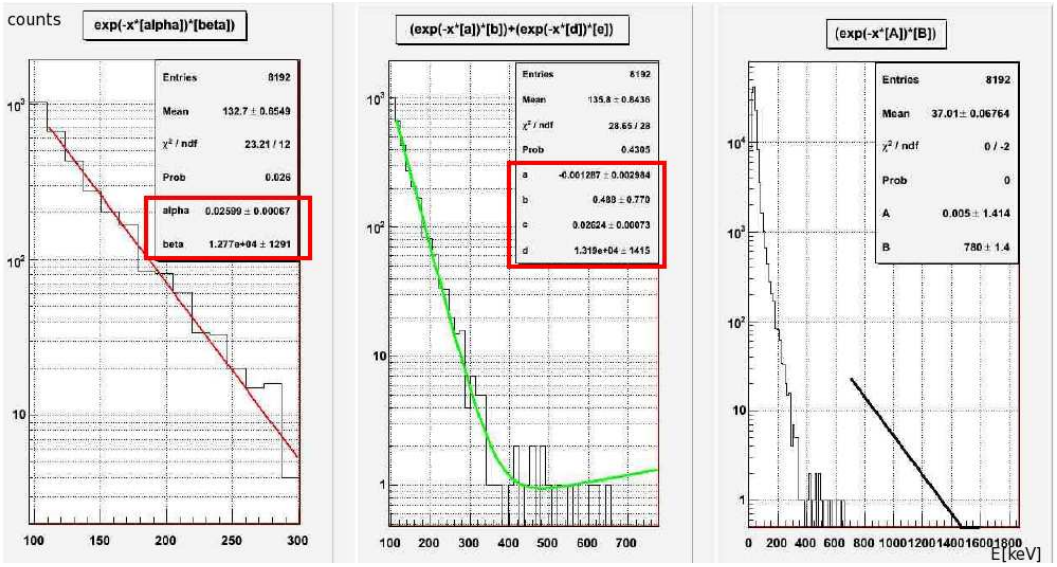

5.5 Dedicated DAQ

A dedicated DAQ, wiht the relative user graphical interface, was realized for the SBD measurements. It lets have the control on several measurement's parameters and, in particular, it allows to have event time information, which is a peculiarity of the used module.
To perform the acquisition the N957 CAEN MCA (Multi Channel Analyzer) was used. It has 8K channels and a USB 2.0 communication interface.

FIGURE 5.13: CAEN MCA used to perform the acquisition with event time information.

The module is software programmable through a set of 16-bits registers: the read or write access to these registers is possible by several functions belonging to module standard library. All the registers are 16-bits except for the ones containing temporal information: these are the *real-time* and *live-time* registers, (which are 32-bits). Thus the peculiarity of this MCA is the opportunity to obtain event-time infomation which can be useful for perfoming a time analysis of the acquired spectra. In fact, in the case ^{232}Th and ^{238}U, the final part of the chain is charachterized by a relatively short time distance between the alpha peaks. The realization of a dedicated event's time-arrival anaylsis would let discriminate the events which effectively belong to the radioactive chain from the events which do not, allowing a more detailed knowledge of the sample contaminations.

5.6 Montecarlo simulations for detection efficiencies

In order to evaluate correctly the detection efficiencies, the Monte Carlo simulation method can be used. Many processes, real physical processes or imaginary ones, can be idealized as a sequence of choices. If it is possible to approximate each choice by some probability function, then one can establish a model which simulate the process. The most common is the Montecarlo method. According to this model many events are generated, each event being the result of a particular sequence of choices. These events are then counted, classiffied and distributed according to criteria as if they were real events. One can then make comparison with existing real data, or predictions of what

FIGURE 5.14: N957 user interface which allows to control several measurement parameters, as the measurement's live time and real time.

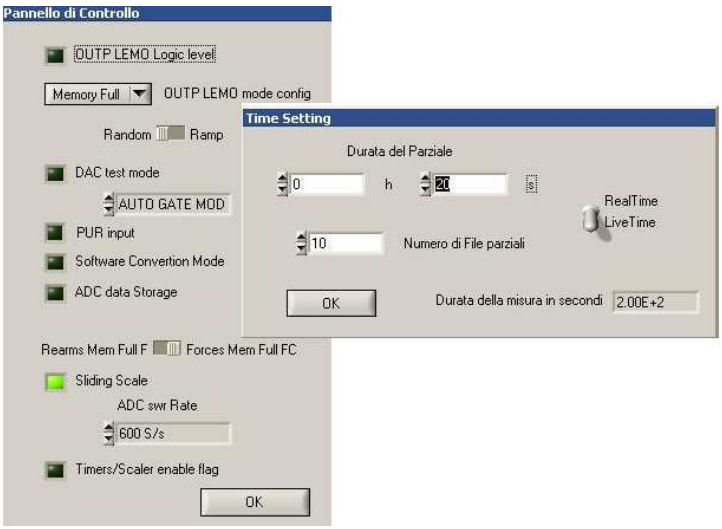

should be the outcome of a given real experiment, provided that the established model simulates nature sufficiently well.
To evaluate the SBD detection efficiencies the Montecarlo method was used to generate events of known origin (a chosen radioactive contamination with a chosen localization), in order to set upper limits (or to calculate, when observed, contaminations) depending on depht of contaminations in the sample materials measured (by comparing these simulated events with the measured data). A code based on the *Geant4* package was used for this pourpose. An hypotesis test was performed.

5.6.1 Simulated surface contaminations

Different contamination hypothesis were simulated for the SBDs, in order to estimate the correct α detection efficiency.
The Monte Carlo Simulation were realized with *Arby* sofware, based on *Geant4* package. It is one of the first successful attempt to re-design a a big package of High Energy Physics (HEP) software for the next generation experiments using an Object-Oriented environment. *Geant4* has many types of geometrical descriptions, in order to have the flexibility to simulate the most complicated and realistic geometries.
The sofware Arby lets the user to describe the desired geometry, detectors and physical process to be used for the simulation. Moreover it permits to choose the wanted depht of contaminants and the analytical profile of contamination.

Several dephts of contaminations were hypotized, from 0.001 μm to 5 μm, and the contaminants studied were: ^{232}Th, ^{238}U and ^{210}Pb/Po. The latter were simulated separately, to discriminate the source of contaminations.
Uniform and decreasing exponential profiles were tested, but this profile determination is much harder than the depht's determination.
The reason for which different dephts of contaminations were studied is to explain not only the peaks observed in the experimental spectra, but the tails too. The deeper

FIGURE 5.15: Three different simulation output compared, relative to ^{232}Th contamination and to different dephts. As it is clear, the deeper the contamination is, the broader are the peaks and the more are their respective tails.

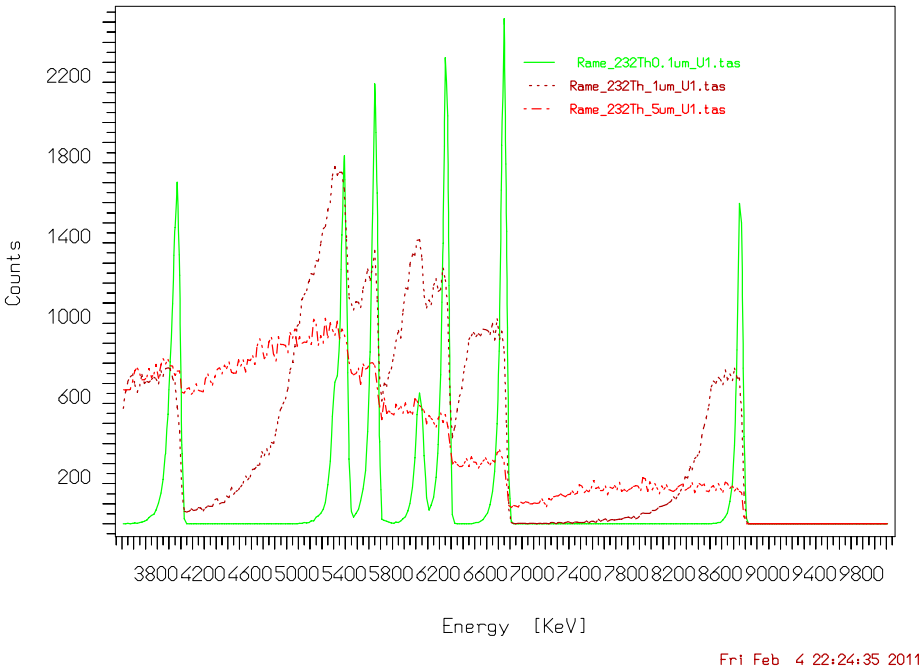

the contaminants are in the source, the more peaks are broadened and the more their respective tails.

The energy regions, where the analysis was performed, are:

- $4-5$ MeV and $7-7.7$ MeV, where it is assumed that the contributions are mainly due to ^{238}U (α's 4.19 MeV, 4.775 MeV, 4.687 MeV, 4.784 MeV, 7.686 MeV, (with the highest energy branching in the mentioned intervals). There arn't thorium's alpha decays with energies that fall within this range.
- $6.1-7$ MeV and $8-8.8$ MeV, where it is assumed that the contributions are mainly due the ^{232}Th (α's 6.04 MeV, 6.288 MeV, 6.778 MeV, 8.785 MeV (again, those which have the highest energy Branching Ratios in the mentioned intervals. No contributions coming from the ^{238}U chain fall in this regions.
- For comparison with the CUORICINO data, also the $3-4$ MeV region was analyzed.
- The peak at 5.3 MeV ^{210}Pb-Po received dedicated attention.

In order to perform the MC simulations informations such as: the expected *rate* of events (estimated from other radioactivity measurements), the time and energy resolution of

FIGURE 5.16: Three different simulation output compared, relative to the 5.3 peak and to different dephts.

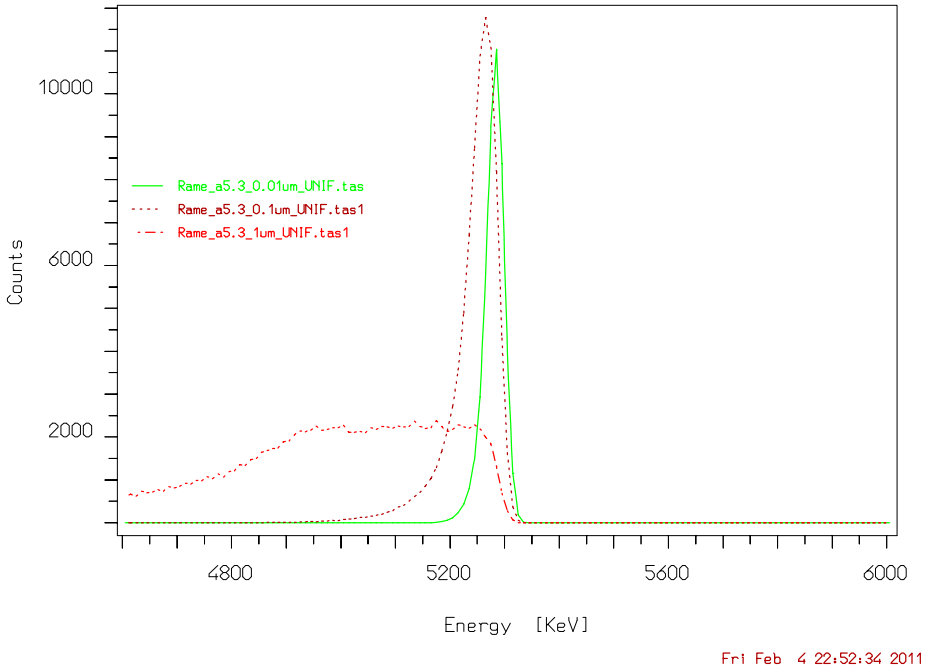

detectors used were necessary as inputs.
The formula which gives the final surface contamination: is:

$$\begin{aligned} Activity[Bq \cdot cm^2] &= \frac{N_c}{\Delta t \cdot \epsilon \cdot S_{sample}} \\ \epsilon &= \frac{N_{c_{MC}}}{N_{ev_{MC}}} \end{aligned} \tag{5.8}$$

where N_c is the number of observed counts in the experimental spectrum, Δt is the measurement time in $[s]$, ϵ is the detection efficiency, calculated from Monte Carlo simulations, $N_{c_{MC}}$ is the number of observed counts in the *simulated* spectrum, $N_{ev_{MC}}$ is the number of generated Monte Carlo events and S_{sample} is the sample's surface in $[cm^2]$.

5.7 Measurements and CUORE material selection

Several materials were measured with the SBDs to let a selection, based on the radiopurity CUORE's requests, to be possible.

The first step for a correct contamination limit evaluation was the **blank** determination. In order to have a reference material, with the aim of establishing a minimum radioactive level of the detecting system, several samples of various materials were measured for a

time of about four weeks. The proper *background material*, to be measured before and after every sample measurement, was found.
This material is common plastic, polyethylene, used also to store the cleaned parts of the cuore detector.

The detectors *calibration* is another crucial step.
Due to the extremely high levels of radiopurity of the measured materials (required for CUORE and the rare event physics experiments in general) the calibration of the detectors becomes difficult, given often no peaks are bserved in the acquired experimental spectra.
The method developed consits in using the detector intrinsic background combined wiht ^{222}Rn contamination. In fact,as previuosly mentioned in this chapter, alpha spectroscopy systems needs a vacuum pump to evacuate the alpha spectrometers. Inserting a new sample in the vacuum chamber needs the latter to be opened and led to atmospheric pressure for a short time. Obviously, the chamber's opening lets the particulate enter the chamber, and in particular, it lets the Radon/Thoron access the chamber where the SBD is located, which is an isotope (inert gas) intermediate in all the natural radioactive chains. Being an inert gas it can easily migrate and, in the case of ^{222}Rn , it is the main reason for the ^{238}U chain secular equilibrium interruption. Its daughter radionuclide with longer life, ^{210}Pb, attaches easily to aerosol and it can stick on surfaces through water as well with dry deposition. The ^{222}Rn daughter isotopes in the uranium chain lead to some α peaks in the experimental spectrum (6 and 7.7 MeV). These peaks, even if negatively contribute to increasing the background, are a clear signature which can be used to calibrate in energy the detector's spectrum.

5.7.1 Measured Materials

The several materials measured can be divided in 4 main groups:

- I. Copper (cleaning screening).
- II. Passive components: pins, teflon, Si heaters, gold wires
- III. Packaging material selection
- IV. Lapping pads (for crystal cleaning).

I. Copper All the copper cleaning techniques realized at the LNL (Laboratori Nazionali di Legnaro) were checked, from the point of view of the radiopurity. The copper surface faced to the CUORICINO detectors is indeed more than the surface faced to the SBD detectors. Although this the SBD measurements are crucial for isolating the contaminations of each kind of cleaning technique and thus for performing a screening on them.
The analysis results are useful and interesting if compared with the previous experimental results.
The results agree with CUORICINO results, while they give lower contamination limits than the Three Towers (TT) results. This is an aspect which needs to be understood with more attention.

II. Passive components In the case of the small passive components the SBD measurements have the advantage of presenting a greater sesitivity (active surface) than the bolometers. The measurements performed gave the possibility of excluding some components as responsible for the flat background observed in CUORICINO.

II. Packaging material selection A study of the packaging materials was performed. This let a selection of the radiopure materials necessary for the storage and transport.

II. Lapping pads Samples of the lapping pads were measured to estimate their contaminations. Even if the mechanism trhough which the contaminants are transferred to the crystals from the pads is not obvious, it is important to use pads as clean as possible. It in fact turned out that the pads initially used were contaminated in ^{238}U and ^{232}Th. The background observed in the crystals produced after the change, with bolometric measurements (known as CCVR measurements, Chinese Crystal Validation Run), is lower respect the background observed befor the change.

The reached limits are, on average:

- $\sim 10^{-7}$ and 10^{-8} (in the best situations) Bq/cm^2 for the 'high' energy region, i.e., from 6 up to 8.9 MeV, which is the last part of Thorium an Uranium chains.
- $\sim 10^{-6}$ Bq/cm^2 for the region from $4-6$ MeV where the parent nuclides α decay.

The SBD measurements give very important information which let to exclude some components as responsible of the observed background in CUORICINO.

Chapter 6

Electron stability

6.1 Introduction

Though the main scientific goal of CUORE and CUORICINO is the search for neutrinoless double beta decay of ^{130}Te, there are several other studies that can be carried out with these low background detectors. They include, for example, the search of dark matter, rare nuclear processes, double beta decay modes other than $\beta\beta0\nu$ to the ground state and the electron decay.
In this chapter the study of the process $e^- \rightarrow \gamma + \nu_e$ and its application to the CUORICINO data will be presented.

6.2 Charges in Physics

The standard model of elementary particle physics is in excellent agreement with all experimental results obtained until now.
Looking for physics beyond the standard model the search for rare events in testing fundamental laws of physics is rather promising. One of the possible tests is that of charge conservation. In the context of gauge field theories, the invariance of the Lagrangian under a given gauge transformation corresponds to the conservation of some specific type of conserved charge. In some grand unified theories, for example, terms appear in the Lagrangian which break the global gauge invariance associated with baryonic charge leading to proton decay at some level [130]
In the electroweak sector the *local* gauge invariance of the Lagrangian, corresponding to the equations of quantum electrodynamics, dictates strict electric charge conservation and a massless photon. Therefore we do not expect electrons to decay, because there is no lighter charged lepton into which it can decay, and the decay into photons and/or neutrinos requires the violation of charge conservation. Non conservation of the electric charge will only be possible if the Lagrangian of QED contains terms which destroys global as well as local gauge invariance.
Just as proton would decay, among other particles, for istance, to a positron and a neutral pion (if the constraint imposed by baryon number conservation is removed), so would the electron decay into a photon and a neutrino (also into a neutrino and neutrino-antineutrino pair) if electric charge conservation is not respected. Such decay of the electron in closed shells of atoms would cause vacancy giving rise to emission of

x-rays and Auger electrons.

There are two possible tests for the electron decay which can be carried out with TeO_2 CUORE bolometers: the search for the 255.5 keV γ rays coming from the decay $e^- \rightarrow \gamma + \nu_e$, and the decay $e \rightarrow \nu_e + \nu_e + \overline{\nu_e}$. The latter is the so-called *disappearance* approach and it is used to search for all electron decay modes, in which the decay particles escape the detector without depositing energy. In this case the only signatures of the decay are the characteristics X-rays.
The best limits for these channels are:

- $\tau > 4.6 \cdot 10^{26}$ yr 90% C.L for $e^- \rightarrow \nu_e + \gamma$, CTF Borexino [1].
- $\tau > 3.7 \cdot 10^{24}$ yr 90% C.L for $e^- \rightarrow \nu_e + \nu_e + \bar{\nu}_e$, DAMA collaboration [2]

The search for the rare electron decay requires a detector with ultralow background, not to loose the expected weak signal at $\sim$ 255.5 keV , over the background radiation. The TeO_2 bolometric crystals, which have been used searching for neutrinoless double-beta decay, give such possibility. The disappereance channel was not investigated because such low thresholds are not available wiht CUORICINO data, even if they will be reasonably reachable with the CUORE experiment facility.

6.3 Models for the electron decay

As already mentionded, the electron would decay into a photon and neutrino ($e^- \rightarrow \nu_e \gamma$) or in three neutrinos ($e^- \rightarrow \bar{\nu}_e \nu_e \nu_e$) if the law of electric charge conservation is *not* respected.
Decay rate for this process would lead to a electric CNC (Charge Non Conserving) parameter estimation . Nowadays consistent theories which could describe the electric charge violation and which could parametrize the actual experimental limits are *not* available.

One possible theoretical model which would give rise to $e^- \rightarrow \nu_e \gamma$ decay is that where the electron and the neutrino are considered composite particles : the electron is regarded as the first excited state, while the neutrino as the ground state of a 1/2 spin particle , bound to a scalar particle; the photon is seen as a bound state of a fermion-antifermion pair on spin 1. The model is pretty similar to the Fermi and Young model for the composit pion and η particle. [120].

Another model (based on *elementary* particles) [121] which deals with the CNC parameter is that which contemplates a weak-interaction lagrangian L that includes a CNC piece, in the usual form, but with the electron, in the leptonic current, replaced by a neutrino:

$$L = L_0 + \delta L$$

with

$$\delta L = \frac{1}{2} \beta e \gamma^\mu (1 - \gamma^5) \nu A^\mu$$

The model is that presented by Suzuki in [133] and assumes a massive photon in the decay rate calculation.
As it is pointed out in the article (and by Okun and Zeldovich [134] and by Voloshin and Okun [135]) even a tiny breaking of electromagnetic gauge symmetry generates a disaster known as the hyperphoton catastrophe [136], if the breacking is explicit rather than spontaneous. To avoid the hyperphoton problem, one must resort to spontaneous breaking of electromagnetic gauge symmetry by a charged Higgs field. [134] [135]. From the slightly photon massiveness some costraints are imposed on physical parameters.

The vertex for this decay is $\frac{1}{2}\beta e\gamma^{\mu}(1-\gamma^{5})$ and the β CNC parameter can be factorized as $\alpha\epsilon$.

FIGURE 6.1: Feynman diagram for the electron decay $e^{-} \rightarrow \nu_e\gamma$.

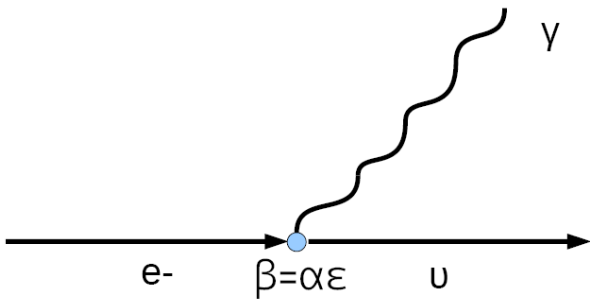

6.3.1 Decay rate calculation for $e^{-} \rightarrow \gamma + \nu_e$

I calculated the decay rate for the process $e^{-} \rightarrow \gamma + \nu_e$, following the Suzuki model, illustrated in the previous section.

As first approach, as it is found in litterature, I considered a massive photon and a massless neutrino (as it is in the Standard Model of elementary particles), even if nowadays the ν oscillation experiments have given evidence of the neutrinos massiveness. The result for this calculation, in natural units ($c = \hbar = 1$), is

$$\Gamma = \frac{\alpha^2 \cdot \epsilon^2 \cdot m_e}{8\pi} \cdot (1 + (\frac{m_e}{m_\gamma})^2) \tag{6.1}$$

As inputs, for the CNC parameter, the following values can be used:

$$m_e = 0.511 MeV$$
$$\alpha = \frac{1}{137}$$
$$m_\gamma \leq 10^{-18} eV$$
$$\tau \leq 4.6 \cdot 10^{26} y$$

where, for γ mass, the value in PDG [122] is used as input and for τ the DAMA collaboration limit is used.
The evalutation of ϵ from this calculation is then,

$$\epsilon \approx 8.76 \cdot 10^{-35} \quad [MeV^{-1}]$$

in natural units ($\hbar = c = 1$).

The second hypotesis used for the cross section caculation is that which assumes not only a massive γ, but a massive neutrino too.
This is a new calculation, respect to what it is found in litterature. The result is:

$$\begin{aligned}
\Gamma &= \frac{m_e^3 \cdot \beta^2}{32 m_\gamma^2 \cdot \pi^2} - \frac{m_\nu^2 \cdot \beta^2}{32 m_e \cdot \pi^2} + m_e \cdot \left(-\frac{\beta^2}{32\pi^2} - \frac{m_\nu^2 \beta^2}{8 m_\gamma^2 \pi^2} \right) = \\
\Gamma &= \frac{\beta^2}{32\pi^2} \cdot \left(\frac{m_e^3}{m_\gamma^2} - \frac{m_\nu^2}{m_e} - m_e - \frac{4 \cdot m_e \cdot m_\nu^2}{m_\gamma^2} \right) \\
\Gamma &= \frac{\epsilon^2 \cdot \alpha^2}{32\pi^2} \cdot \left(\frac{m_e^3}{m_\gamma^2} - \frac{m_\nu^2}{m_e} - m_e - \frac{4 \cdot m_e \cdot m_\nu^2}{m_\gamma^2} \right)
\end{aligned} \tag{6.2}$$

where m_ν is the neutrino mass and the value used for this paramtere is $\approx eV$ (from the tritium decay $m_\nu \leq 2eV$ [137]). The evaluation of ϵ from this hypothesis is

$$\epsilon \approx 3.11 \cdot 10^{-34} \quad [MeV^{-1}]$$

in natural units ($\hbar = c = 1$).

6.4 Experimental result with CUORICINO data

6.4.1 CUORICINO data RUN II analysis

In Cuoricino each detector is monitored by an independent trigger. When the trigger threshold is exceeded (due to the presence of a pulse) a sample of 512 points, corresponding to a 4 sec window, is acquired and stored to disk. The off-line analysis takes care of extracting, from each sample, the most relevant parameters useful to characterise the pulse. These are the channel number (corresponding to the detector that fired), the pulse height, few estimators of the pulse shape (like rise and decay time of the pulse) and the pulse occurring time.
The pulse height is then converted into an energy value, by means of calibrating parameters that are extracted from "calibration runs" (i.e. runs where the detectors are exposed to a ^{232}Th calibrating source). Before this conversion, a correction for possible gain drifts of the detectors (induced by temperatures variation in time) is applied. Also a check of the data quality is applied, channel by channel, and eventually time intervals corresponding to a "bad" performance of a particular detector can be removed from the data. This "dead time cut" is properly accounted for by reducing accordingly the live time of the corresponding detector.
In table (4.1) the live time for big and small detectors is reported; this is obtained as

the sum of the live-times of each detector belonging to one of the two groups. The data that are made available for the study of the different physics channels are nuples in which an entry (event) corresponds to a pulse triggered on a particular channel. Stored in the event are - as mentioned - the *energy*, the occurring *time* and the *pulse shape* parameters.
For the analysis discussed in this chapter a spectrum have been produced, starting from the whole collection of run II nuples and appling the following set of cuts:

- A fixed *dead time cut* used to reject time intervals centered on the heater firing. The heater is a device used to produce a reference pulse in each detector, with a fixed periodicity. This pulse is used to measure the gain of the detector and eventually apply the mentioned gain correction. In order to avoid possible interference between a particle signal and a heater signal a fixed dead time cut is applied. This reduces the live time of each detector by 97.7%.
- A *pulse shape cut* applied to remove spurious triggered signals (that have a shape different from the typical response of the bolometer and can then be distinguished with a proper pulse shape analysis) or true signals deformed by noise (since the noise can alter the pulse height evaluation). Since this cut can remove true signals it has an associated efficiency that will be discussed later in the section (4.7.3).
- An *anticoincidence* cut that consists in the removal of events that corresponds to contemporary hits on more than one crystal. Indeed we search for a single event hit therefore this cut does not reduce the signal (if not for accidental coincidences) but itt is effective in reducing the background. The accidental remove of single-hit signals is evaluated again in terms of an efficiency as discussed later in the section (6.7.4).

Crystal Type	**Crystal Mass [g]**	**Live Time[h]**
Big	790	608586
Small	330	190747

TABLE 6.1: Live time statistics and mass for the two crystal types: big and small crystals.

The idea of the present work is to search for γ rays which could be produced by the decay of any electron in the TeO_2 bolometers and in its surrounding, by analyzing the energy distribution collected during Run II.
The exact value of the visible energy (E_v) deposited in the detector depends on where the electron decay occurs: if it happens in lead or in copper (in our case) or if it happens in one of the crystals, but it is detected by a nearby one. . Given it is a two body decay, the available energy ($m_e - E_B$) is shared between the final neutrino and the photon.

$$m_e = E_\gamma + E_\nu + B.E. \tag{6.3}$$

where *B.E.* is the binding energy.

If the decay happens outside the sensitive volume of the detector the deposited energy is simply equal to the energy released by the photon:

$$E_v = \frac{\left(m_e c^2 - E_b\right)}{2} \tag{6.4}$$

where $m_e c^2$ keV is the electron mass and E_b is the binding energy of the decaying electron in the corresponding atomic shell. If the electron decay occurs in the sensitive volume of the detector, the energy deposited in it is a sum of the photon energy E_γ and of the energy released by the X-rays or Auger electrons following the atomic deexcitation (with total energy of E_b):

$$E_v = \frac{\left(m_e c^2 - E_b\right)}{2} + E_X = \frac{\left(m_e c^2 + E_b\right)}{2} \tag{6.5}$$

where $m_e c^2$, 511 keV, is the electron mass and E_b is the binding energy of the decaying electron on the corresponding atomic shell i.e., for the electron decay in the crystal either E_b 32 keV for the K shell or E_b 4.9 keV keV for the L1 shell, etc.). The approximation $E_b \approx E_X$ for Te is made in the last equation.
The materials studied in this analysis are: tellurium crystals, mounting copper bars, mounting copper box and roman lead shield.
Data for binding energies are taken from [125].
I summarize in tables (6.2), (6.3) and (6.4) the several signatures (γ rays), which depend on where the decay happens, i.e., in which material and in which atomic shell.
In order to calculate the final limit it is necessary to take into account the Doppler broadening due the electrons orbital motion in the atomic shells. This effect is not negligible, especially for materials, like lead, for which the broadening is $\sim$ 90 keV.

6.4.2 Doppler broadening

The Doppler broadening of the γ lines is due to the orbital motion of the electrons in the atomic shells. The broadened line shape is calculated by assuming that the electrons have a temperature corresponding to the expectation value of kinetic energy asssociated with a given energy level and that the virial theorem is fulfilled. According to the theorem:

$$< E_{kin} >= -\frac{1}{2} < E_{pot} > \tag{6.6}$$

in the case of a Coulomb potential. The Doppler line shape is given by:

$$\begin{aligned} I(E) &= \frac{1}{\sqrt{(2\pi)} \cdot \sigma} e^{\frac{-(E-E_v)^2}{2\sigma^2}} \\ \sigma &= E_v \cdot \sqrt{\frac{kT}{m_e c^2}} \end{aligned} \tag{6.7}$$

Here k is the Boltzmann's costant, T is the absolute temperature, m_e is the electron mass and E_v is the transition visible energy, i.e., the γ-ray energy from the decay of the electron in a given shell.

The overall FWHM's will be dispayed in the next section.
For the calculation only the K-shells are considered.

6.5 Detector Response function

The detector's response function to the signature expected is the convolution of two factors:

- Gaussian response function
- Doppler broadening

And:

$$FWHM = 2.35\sigma_{tot} = \sqrt{FWHM^2_{Doppler} + FWHM^2_{resp}}$$
$$\sigma_{tot} = \sqrt{\sigma^2_{Doppler} + \sigma^2_{resp}}$$

where $\sigma_{Doppler}$ was defined previously.

6.5.1 Signatures

For the electron decay study four different materials were taken into examination:

- TeO_2 crystals. The decay in Tellurium was considered.
- Copper, in detail, copper mounting *box* and copper mounting *bars*.
- Lead, in detail, the shielding.
- 50 mk shield (copper).

Considering the crystals, there are two class of decays: external eq. (6.4) and internal eq. (6.5) decay, respect to the active volume of the detector. The second case was studied with the aim of Monte Carlo simulations. It was found the containment efficiency for Tellurium's X-rays (which could go out from the crystal), is 100%; therefore this kind of signature does not need to be accounted for.

These two classes lead to different signatures. Regarding copper and lead, only the situation in which the deexcitation X-ray isn't detected is possible, i.e., the signature can be only of the eq. (6.4) kind.
All the informations on signatures and shapes are summarized in the tables below. $\mathbf{E_V}$ is the visible energy, $\mathbf{E_B}$ is the binding energy, $\mathbf{FWHM_{Doppler}}$ is the FWHM considered only the Doppler broadening and finally $\mathbf{FWHM_{tot}}$ is the total FWHM, calculated considering the convolution of the detector response function and the doppler effect on the line shape:

Material	**M[kg]**	$\mathbf{N_{electrons}}$
Oxigen	8.16	$2.46 \cdot 10^{27}$
Tellurium	32.540	$7.99 \cdot 10^{27}$
Copper bars	5.88	$1.62 \cdot 10^{27}$
Copper Box	8	$2.20 \cdot 10^{27}$
50 mK	6.477	$1.78 \cdot 10^{27}$
Lead shield	174.15	$4.15 \cdot 10^{28}$

TABLE 6.2: In hte first column there is the kind of material considered for the simulations, in the second one the relative total mass and in the third the amount of relative electrons, potentially decaying.

$\mathbf{E_V}$**[keV]**	$\mathbf{E_B}$**[keV]**	$\mathbf{FWHM_{Doppler}}$**[keV]**	$\mathbf{FWHM_{tot}}$**[keV]**
255.5	0.09	8.04	8.45
258	4.63	56.60	57.77
270	31.81	140.49	158.57

TABLE 6.3: TeO_2 signatures.

$\mathbf{E_V}$**[keV]**	$\mathbf{E_B}$**[keV]**	$\mathbf{FWHM_{Doppler}}$**[keV]**	$\mathbf{FWHM_{tot}}$**[keV]**
255.5	0.08	7.58	7.95

TABLE 6.4: Oxygen signatures.

$\mathbf{E_V}$**[keV]**	$\mathbf{E_B}$**[keV]**	$\mathbf{FWHM_{Doppler}}$**[keV]**	$\mathbf{FWHM_{tot}}$**[keV]**
251	8.98	78.15	78.23
255.5	0.09	8.04	8.45

TABLE 6.5: Copper signatures.

$\mathbf{E_V}$**[keV]**	$\mathbf{E_B}$**[keV]**	$\mathbf{FWHM_{Doppler}}$**[keV]**	$\mathbf{FWHM_{tot}}$**[keV]**
251	8.98	78.15	78.23
255.5	0.09	8.04	8.45

TABLE 6.6: 50 mK signatures.

$\mathbf{E_V}$**[keV]**	$\mathbf{E_B}$**[keV]**	$\mathbf{FWHM_{Doppler}}$**[keV]**	$\mathbf{FWHM_{tot}}$**[keV]**
211	88.01	205.78	205.79
248	14.69	98.84	98.88
255.5	0.316	14.94	15.17

TABLE 6.7: Lead signatures.

6.6 Efficiencies with Monte Carlo simulations

In order to evaluate the detection efficiency Monte Carlo simulations were used to generate about $5 \cdot 10^6$ events for each decay line being investigated.
With the program *Tower-4.9.3*, based on GEANT4, the lines were simulated within the crystals of the CUORICINO tower. At first approximation, the *bare* efficiencies were calculated without any correction, i.e., nor the experimental active channels, neither the real detection thresholds were considered.
Thus, the signal containment efficiencies were about 80%, for example, for the Tellurium 255.5 keV line.
This *naïve* approach is *not* satisfactory, considered that during CUORICINO runs, not all the channels were always active and that the thresholds in some crystals were too high to make the expected signal detectable.
The evaluation of the live time and the detection efficiency were corrected processing the output of Monte Carlo simulation with a dedicated code. *simu2qino* [128]. The latter accounts for all the experimental details: for the time periods in which one or more detectors were not operative and for the experimental detection *thresholds* of all the crystals.

FIGURE 6.2: 255 keV gamma line counts simulated in thec crystal bulk, after the application of the cuts due to the simu2qino code: the switch off of some detectors is clearly evident.

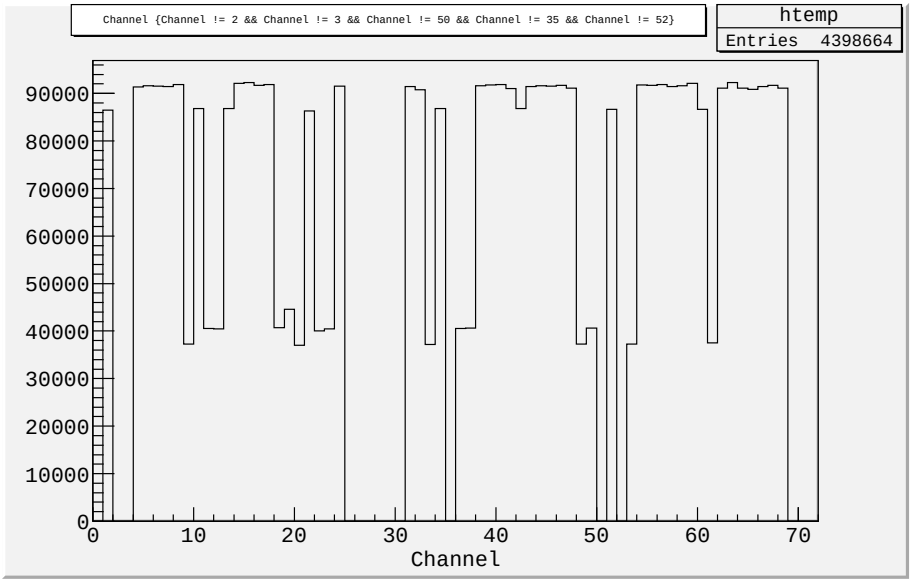

The code was used for all the simulated signals and the respective materials in which the decay happens.

6.7 Inefficiencies

The signal efficiency is the *probability* that a signal event is detected, its energy is reconstructed accurately, and it passes the data selection cuts.

FIGURE 6.3: Sum-Spectra over all the Cuoricino detectors for all the possible e-decay signatures due to: Teo_2 crystals, copper mounting bars and copper mounting box, lead shield, 50 mK in logarithmic scale, with no Doppler broadening.

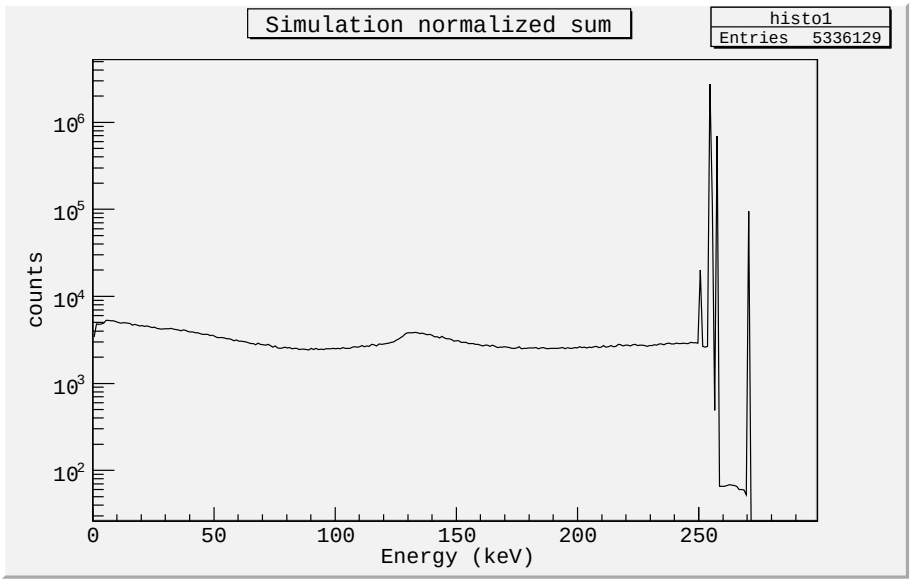

FIGURE 6.4: Sum-Spectra over all the Cuoricino detectors for all the possible e-decay signatures due to: Teo_2 crystals, copper mounting bars and copper mounting box, lead shield, and 50 mK in linear scale, with no Doppler broadening. On the top there is a zoom of the energy region between 200 and 300 keV, where the best fit is computed. (see section (6.9)).

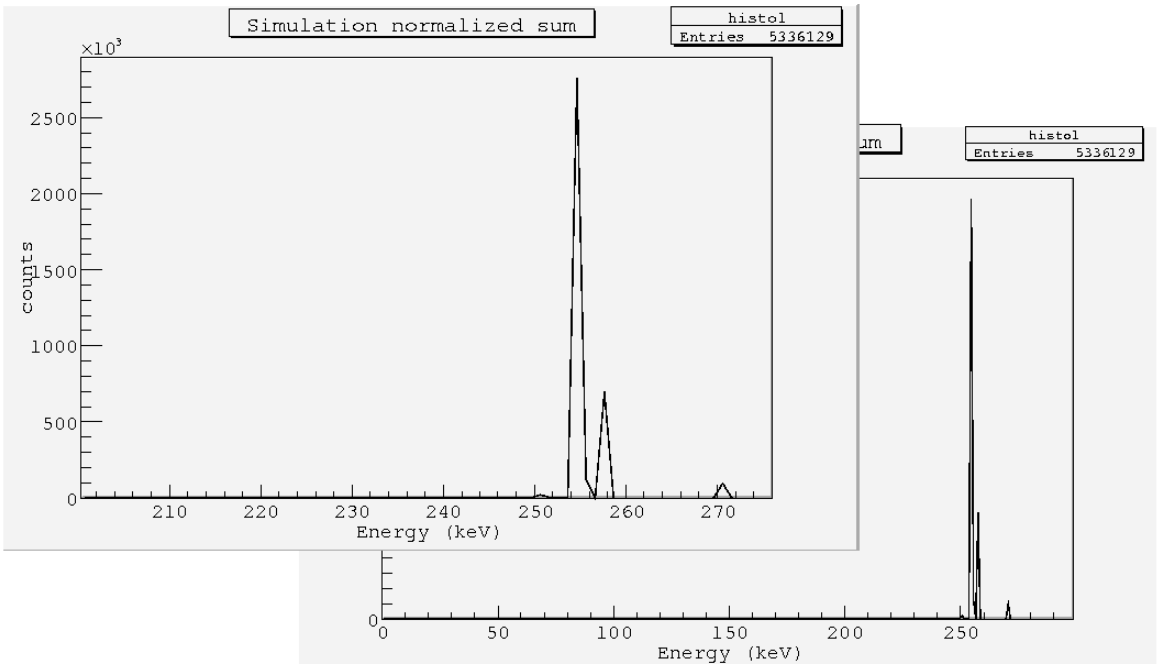

Among the mechanisms for loss of signal efficiency there are the pulse shape cut and the anticoincidence cuts. In the following sections they will be discussed.

6.7.1 Pulse shape cut

A pulse shape cut is applied to remove events that are not consistent with a single physical pulse in the acquisition window. Some events rejected by the pulse shape cut are spurious fluctuations of the thermistor voltage due to noise or temperature instabilities that are large enough to trigger the data acquisition. The pulse shape cut also removes pileup involving multiple events in the same acquisition time interval, including most cases of pileup on the rise of the pulse, except when two events in the same crystal occur so close in time as to be indistinguishable from a single event with the sum of their energies.
Effciency loss occurs if the pulse shape cut rejects any good events. The pulse shape cut is designed to be conservative, i.e., good events should be retained with close to 100 % efficiency.
To evaluate the efficiency of the pulse shape cut different three peaks were studied, for different resons.

- the peak at 239 keV, due ^{212}Pb background contamination. This peak is chosen because the pulse shape cut is energy-dependent and the 239 keV peak is the closest to 255.5 keV. Unfortunately this peak's statistics is not enough, thus another peak was analyzed with the aim of having a more realistic evaluation of the PSA inefficiency, the 511 keV peak.
- the escape peak at 511 keV, which has more statistics than the previous one and it is not too far in energy from where the signal is expected to be found.

The efficiency for this kind of cut is

$$\epsilon_{PSA} = (0.972 \pm 0.010)$$

and it is the wheightened average of the values obtained for the 239 keV and 511 keV peaks. The uncertainity is due the fit errors. This result is the ratio between the gaussians areas, computed with the fit, after and before the PSA cut. It gives an estimate of the lost events. As it is possible to appreciate also from the plot in fig.(6.5) and (6.6), the PSA cut consistently ($\sim 30\%$ reduction) cuts down the background counts at the peak location.

6.7.2 Anti-coincidence cut

An anti-coincidence cut is applied to suppress background, given the electron decay signature searched is a single-crystal event.
The anti-coincidence cut rejects any events that occur within 100 ms of an event in another crystal. The only efficiency loss from the anti-coincidence cut is due to the possibility of a random coincidence with another event. The probability of an event

FIGURE 6.5: Fit of the 239 keV peak before and after the Pulse Shape cut. The ratio between the area after and before the cut is an estimator of the loss of *good* events

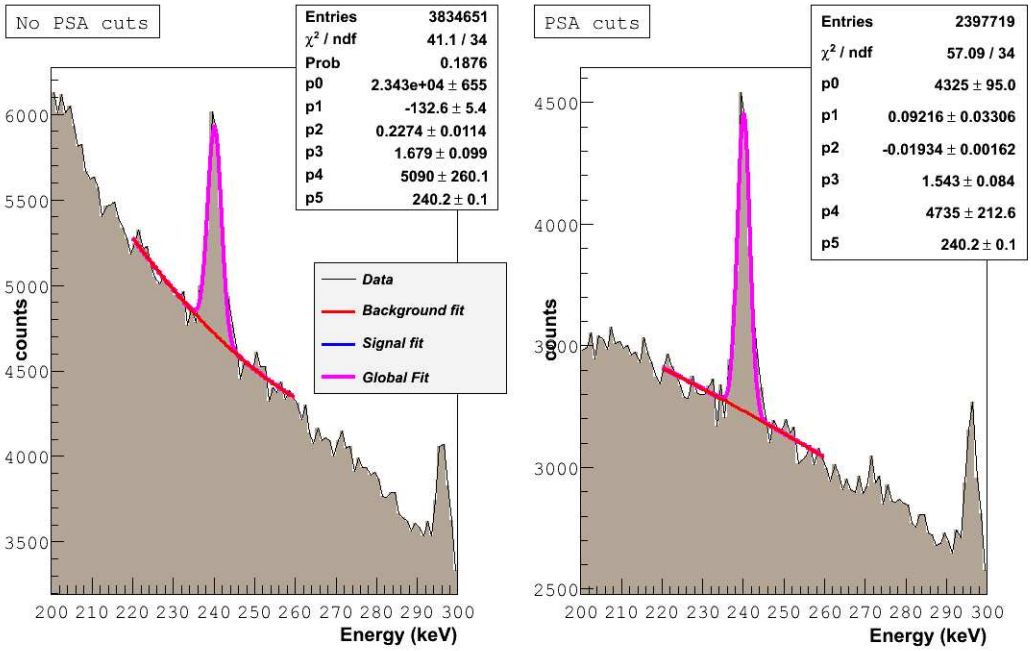

FIGURE 6.6: Fit of the 511 keV peak afer and before the Pulse Shape cut.

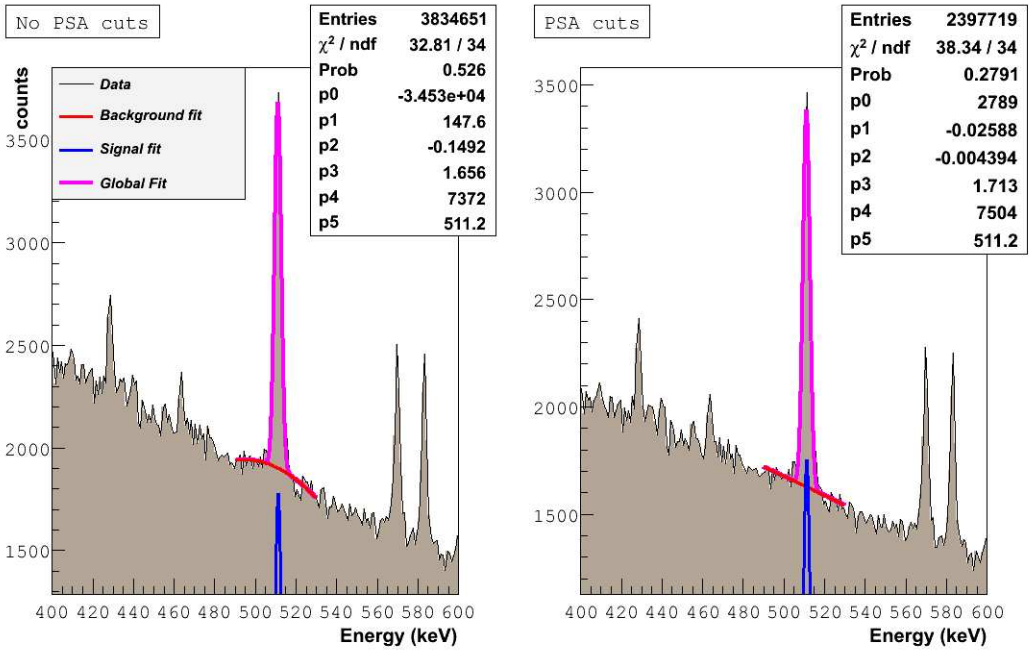

randomly occurring (for paralyzable detectors) within $\pm\Delta$T of a particular event is given by

$$Prob(random\ coincidence) = 1 - e^{-2r\Delta T}$$

where r is the total event rate on all other bolometers. The signal efficiency, being the probability that a random coincidence does not occur, is $\approx e^{-2r\Delta T}$.
For this analysis the efficiency due to the anti-coincidence cut is evaluated following the same procedure used for the pulse shape cut efficiency. In this case the peak used is only the 1460 ^{40}K, because it is the only available gamma peak which doesn't have physical concidences.
For CUORICINO the fit result for the efficiency of the anti-coincidence cut is (0.995 ± 0.010).

FIGURE 6.7: Fit of the 1460 keV peak before and after the Pulse Shape and the anticoincidence cuts. As explained in the section, only this single-nuclide peak offers the possibility to evaluate the events loss due to spurious concidences

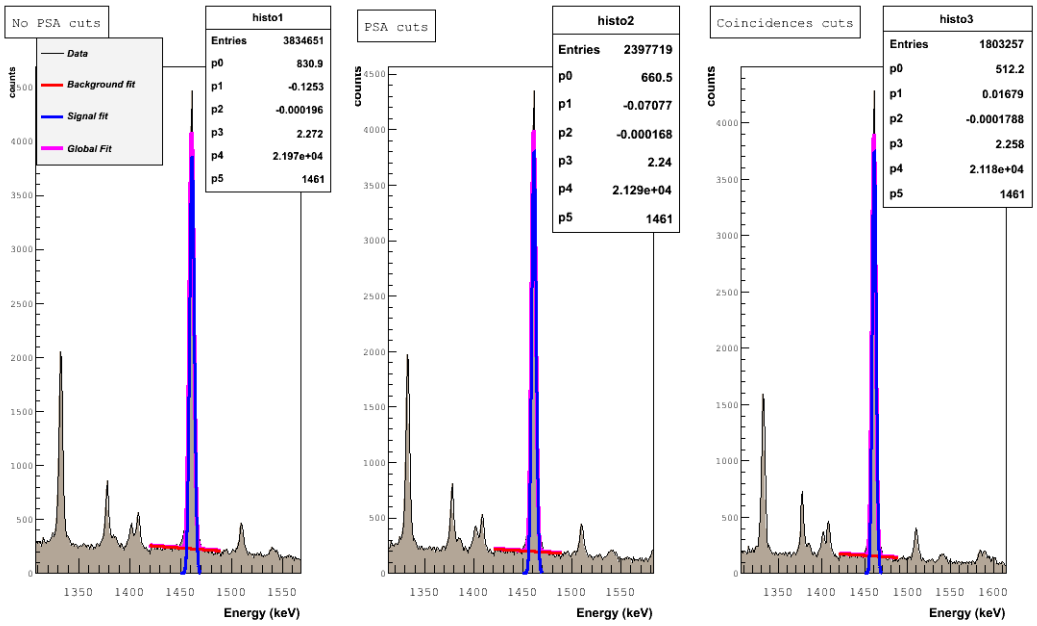

6.7.3 Overall efficiency

The overall efficiency, which accounts for the loss of good events, is the product of the indipendent factors:

$$\epsilon_{tot} = \epsilon_{PSA} \cdot \epsilon_{coinc} = (0.967 \pm 0.010) \tag{6.8}$$

where ϵ_{tot} is the total efficiency, ϵ_{PSA} is the efficiency after the PSA cuts and ϵ_{coinc} is the efficiency after the anticoincidences cuts.

6.8 Analysis with Timezzo

6.8.1 Limit technique

Since no signal for the electron decay is observed, an *upper limit* on the decay rate is set.

Almost the same code, **Timezzo**, based on MINUIT and used in [126] is here used.
In general the expected number of counts c produced in a detector by a physical process with half life $\tau_{1/2}$ can be expressed as

$$c = \frac{ln2}{\tau_{1/2}} \cdot N \cdot t \cdot \epsilon \tag{6.9}$$

where N is the number of decaying candidates put under observation, t is the duration of the observation and ϵ is the detection efficiency for a given decay pattern.
Therefore the half life corresponding to a certain number of observed counts is given by

$$\tau_{1/2} = \frac{ln2 \cdot N \cdot t \cdot \epsilon}{c} \tag{6.10}$$

However, in order to claim for a positive signal, the number of counts produced by the studied physical process must be significantly higher than the possible fluctuations in the number of background events. Assuming Poisson statistics, the previous statement translates in the requirement that $c > n_\sigma\sqrt{b}$, where b is the number of background counts and n_σ is the number of standard deviations, which expresses the statistical significance of the result.
Therefore the half life sensitivity $S_{1/2}$ for a given physical process can be written as

$$S_{1/2} = \frac{ln2 \cdot N \cdot t \cdot \epsilon}{n_\sigma\sqrt{b}} \tag{6.11}$$

In other words, the sensitivity of an experiment is defined as the half life corresponding to the minimum number of signal events observable above background at a given confidence level. For experiments in which the number of background counts scales as the total mass of the detector, it can be expressed as [127].
Equation (6.10) can be easily obtained in the assumption of Poisson statistics, starting from the consideration that a positive signal is found if the number of observed events in the region of interest differs by more than n_σ standard deviations from the number of background events in the same region. In eq. (6.10) ϵ is the detection efficiency, N_a is the Avogadro number, η is the isotopic abundance of the studied nucleus, A is its atomic mass number, M is the total detector mass, t is the live time of the experiment, ΔE is the energy resolution and b is the background, expressed in terms of $counts/(keV \cdot kg \cdot years)$.
The detector sensitivity assumes a different form if no background is present (or at least the number of background counts is negligible over the life of an experiment):

$$S^{0\nu} = \epsilon \cdot \eta \cdot M \cdot t \tag{6.12}$$

Thus, in contrast to the previous case, in which the sensitivity scales as the squared root of the mass M and of the measurement time t, in a *zero background* experiment the dependence on these two parameters is linear.

6.8.2 Results

The code assumes Poisson statistics for the binned data, the fit procedure is formulated in terms of the likelihood chi-square analysis.

$$P(n_k, f_k) = \frac{e^{-f_k} f_k^{n_k}}{n_k!}$$
$$\prod_k \frac{e^{-f_k} f_k^{n_k}}{n_k!} = \text{Ł} \tag{6.13}$$

$P(n_k, f_k)$ is the probability of finding n events in the k^{th} bin, if the expected value is f and L is the Poisson likelihood. So the logarithm of the Poisson likelihood can be taken as the sum of contributions of the form

$$lnL(\Gamma) = \sum_k (-f_k + n_k ln f_k - ln(n_k!)) \tag{6.14}$$

The question is which kind of f describes the decay experimental signature.

If the signal under study is a simple **single gaussian**, the number of observed events is calculated from the peak's fit. From the latter is then possible to calculate the decay's probability, Γ. This is what the code Timezzo *usually* does, as for example the $\beta\beta0\nu$ decay, given it some input parameters, as the signal efficiency, the total detector mass, the FWHM, etc.

For the electron decay the detector response function is *not* a single gaussian.
The function which is used to describe this process is the **sum of several gaussian**, whose relative intensities are ruled by the effective number of potential emmitters and by the branching ratios (*B.R.*) for the specific decay from a particular atomic shell. The gaussians are located at different energies, have different shapes (different FWHM's, due to different Doppler broadening), intensities and efficiencies. However, these several signatures have the same Γ.
The starting hypothesis is that the experimental spectra is described by:

$$f(E) = B(E) + \sum_{j.k} n_{j,k}(E) \tag{6.15}$$

where $n_{j,k}(E)$ is the observed line, in the experimental spectrum, of the j^{th} material and at the k^{th} energy and $B(E)$ is the function which describes the background (peaks and continuum).
The general shape of the line is:

$$n_{j,k}(E) = N_{j,k} \cdot BR_{j,k} \cdot \epsilon_{geo-j,k} \cdot gaus\ S(E)_{j,k} \cdot \Gamma_{elect} \tag{6.16}$$

where: $N_{j,k}$ is the number of electrons from the j^{th} material which give the k^{th} line, $BR_{j,k}$ is the related branching (respect to the total number if electrons in that material), $\epsilon_{geo-j,k}$ is the efficiency for that signature , and the gaussian shape at the proper energy

and with the right FWHM, which results from the convolution of a gaussian detector response function (with a FWHM due to the detector resolution) and a gaussian which describes the Doppler broadening (and whose FWHM is different for each signature).
The equation 6.14 can be written as:

$$f(E) \cdot t = B(E) \cdot t \cdot + \Gamma_{elect} \cdot NORM \cdot G(E) \cdot t \tag{6.17}$$

where $G(E)$ is the overall gaussian response function

$$G(E) = \sum (N_{j,k} \cdot BR_{j,k} \cdot \epsilon_{geo-j,k} \cdot gaus\ S(E)_{j,k}) / NORM \tag{6.18}$$

Thus the code Timezzo uses the model of (6.16) to perform the spectrum fit, with the analitical function described by (6.17), which is peculiar to the electron decay.
Finally Timezzo gives as output $\Gamma \cdot NORM$ and then Γ is obtained dividing the output by the NORM factor.

Let describe in details the calculations performed: the studied materials are

- Tellurium
- Copper: in detail, Copper Mounting Bars and Copper Mounting Box
- Lead shield

Each of the listed materials (x) shows several peaks and each peak is featured by: (I) a different geometrical efficiency (which is computed by the mean of Monte Carlo simulations), and by (II) a different number of electrons (belonging to a specific atomic shell) which effectively concur to a specific signature.
Assume, for semplicity of description, there are two materials contributing to the decay signature, x_1 and x_2. Thus the geometrical efficiencies are:

$$eff_{geo(x_1,\alpha_1)} = \frac{m_{x_1,\alpha_1}}{M} \qquad\qquad eff_{geo(x_1,\alpha_1)} = \frac{m_{x_2,\alpha_2}}{M} \tag{6.19}$$

where $m_{x_1,\alpha_1 - x_2,\alpha_2}$ is the total number of events at the signature (α_1, α_2) positions found in the Monte Carlo spectra and M, common to all the simulations, is the total number of generated events. But this is not the unique information to account for: there is need to include the total number of potential emitters for the material x and the B.R. for the specific line (denoted by greek lettters).
Thus the *overall* efficiency for each material X and each specific line α is.

$$\epsilon_{ov} = \frac{N_x \cdot BR_\alpha \cdot eff_{geo,x,\alpha}}{NORM} \tag{6.20}$$

The normalization factor $NORM$ is thus:

$$NORM = \sum_{x,\alpha} eff_{geo,x,\alpha} \cdot BR_\alpha \cdot N_x \tag{6.21}$$

Thus the efficiency whihch is the input for the code is the one indicated by eq. (6.11) and the final rate outuput is rinormalized for the factor NORM. The further inclusion of the PSA plus coincidences cuts loss ϵ_{cuts} of efficiencies is made in the very last step. The final used formula is:

$$\tau = \frac{NORM}{Rate_{T_{1/2}}} \cdot \epsilon_{cuts}$$

The resulting best fit for the electron decay is:

$$\Gamma_{Best} = (-2.19^{+1.47}_{-1.46}) \cdot 10^{-26} yr^{-1} \tag{6.22}$$

The upper bound on the half-life , calculated assuming a linear background shape is:

$$\tau \geq 6.24 \cdot 10^{25} yr \ @ \ 90\% C.L. \tag{6.23}$$

FIGURE 6.8: Timezzo output on the experimental spectra. In the energy region under study it is possible to appreciate four lines: the light blue line is the background fit (linear), the two positive curves in light pink are the fit at 68% and 90% C.L., while the light pink negative curve is the best fit.

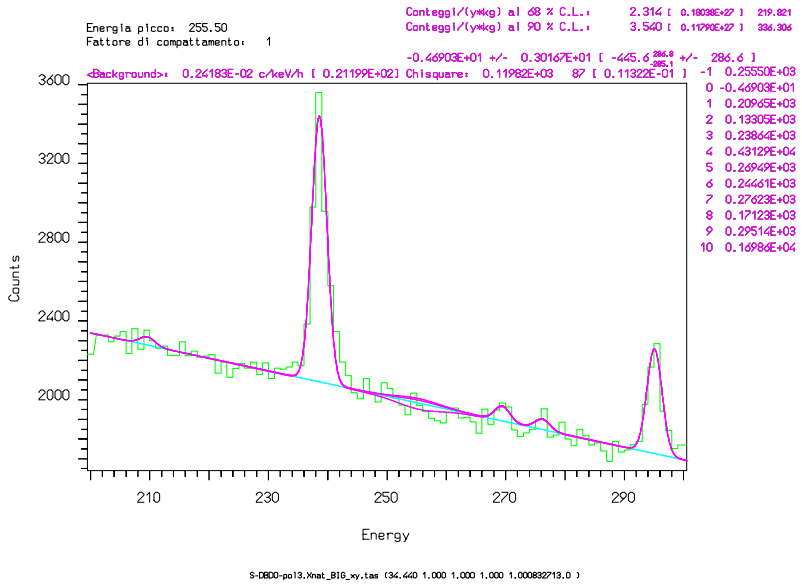

6.8.2.1 Considerations on the background

To calculate the fit the choice is to use 200-300 keV energy windows which includes all the expected signatures and contains some background peaks due to natural radioactivity. These peaks are: 209 keV (^{228}Ac), 239 keV (^{212}Pb), 270 keV (^{228}Ac), 277 keV (^{208}Tl) and 295 keV (^{214}Pb). Given all the listed peaks (save for the last one at 295 keV which belongs to the uranium chain) belong to the ^{232}Th chain, it is useful to check whether the relative intensities of the peaks respect their respective Branching Ratios (BR), in order to validate the assumptions made on the background.

FIGURE 6.9: Plot of all the signature (obtained with Monte Carlo simulation) in the energy region of interest, in log scale, and the relative sum sperctra.

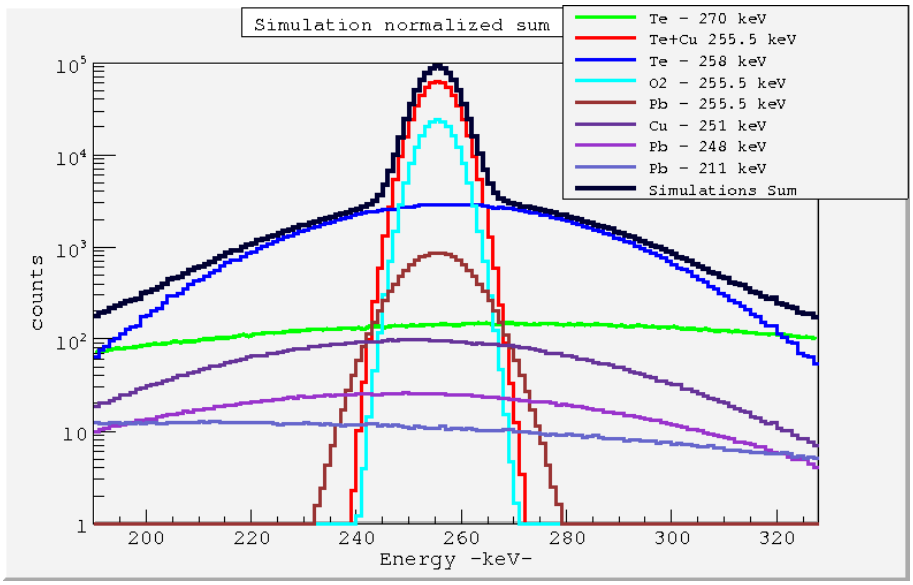

Overall NORMALIZATION	$8.0 \cdot 10^{27}$
Material	**NORMALIZATION**
Oxigen	$1.6 \cdot 10^{27}$
Tellurium	$5.3 \cdot 10^{27}$
Copper bars	$2.7 \cdot 10^{26}$
Copper Box	$5.3 \cdot 10^{26}$
50 mK	$1.4 \cdot 10^{26}$
Lead shield	$1.4 \cdot 10^{26}$

TABLE 6.8: Overall NORMALIZATION factor and *weight* of each material.

Peak energy [kev]	**BR**	**BR ratios**	**Intensity ratio**
209	0.04	0.09	0.03 ± 0.03
239	0.45	**1**	**1**
270	0.04	0.08	0.06 ± 0.02
277	0.02	0.05	0.04 ± 0.02

TABLE 6.9: Chek of the peaks intensities respect to the relative BR's for the ^{232}Th chain. The most intense pek, at 239 keV, is the reference peak to which all the others are compared .

FIGURE 6.10: Energy region of the spectra where the fit is performed. The peaks from I) to IV) belong to the ^{232}Th chain, while the V) belongs to the ^{238}U chain.

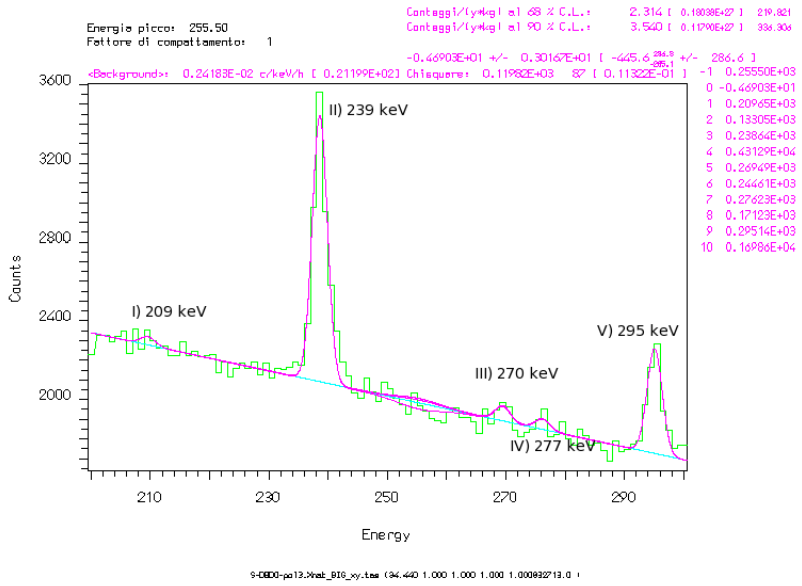

The results agree with the expected ratios. The background representation, at least fot the peaks, is satisactory.

6.8.2.2 Systematic errors

The sources of systematic errors on the electron decay rate result are:

- The uncertainty on the *energy scale*. Actually this contibution is negligible (~ 0.3 for the used calibration).
- The almost arbitrary choice of *energy window* for the fit.
- uncertainty in the *background shape*

The definition of the energy window used to fit the spectrum, the hypothesis assumed for the background shape and the number of free parameters used to describe the background itself are important for the choice of the analysis procedure and for the determination of its systematic. The choice of the energy window is somehow arbitrary, but it influences the background representation. If the energy window is too wide (compared to the FWHM) a physical model able to describe the background shape is mandatory. Obviously there is also a *minimum* size of the energy window necessary to be able to evaluate the background level beyond the electron decay peaks.

Appendix A

Ackoweledgements

I would like to thank the CUORE collaboration for all the support to my thesis work.
Innanzitutto, voglio ringraziare il prof. Ezio Previtali per tutto il supporto che mi ha dato in questi anni, per tutto ciò che ha cercato di insegnarmi, di fisica, e non solo. Per il sostegno per scrivere questa (ed anche le altre due) tesi. Grazie, davvero.
Vorrei poi ringraziare Monica per avermi supportato e sopportato tutte le volte che le inviavo versioni non aggiornate di elementi di matrice.
Grazie mille a Maura e Oliviero per l'enorme aiuto che mi hanno dato per far decadere l'elettrone. Grazie a Chiara, per avere avuto un *occhio* di rigardo nei miei confronti.
Grazie a Stefano e Carlo, per le preziosissime osservazioni (cioè, per avermi salvato all'ultimo momento).
Grazie poi a tutti coloro che mi hanno aiutato *informaticamente*: Sergio Di Domizio (ora simu2qino funziona), Maria (che ormai ha paura di connettersi a skype) e Silvia, grazie ad Andrea (che mi ha dato un *macro* aiuto). Grazie a Filippo (giuro che non sbaglio più chat e numero di telefono),
Ringrazio i miei genitori, zia Flavia, Alessandro e Mary, che hanno sostenuto i miei studi per tutti questi anni e mi sono sempre stati vicini, soprattutto nei momenti difficili.
Grazie a mia cugina-sorella Vale.
Grazie ai miei compagni si ufficio: LucaP (che non mi fa mai lavorare e manomette la mia tesi), Luca G. (che NON manomette la mia tesi e per le mille discussioni super-produttive), Marco (per le chat notturne...e Battlestar), Elena e Matteo.
Grazie a tutti i miei amici teorici...nel senso di fisici teorici, che hanno cercato di insegnarmi tanto, a fatica. Grazie Antonio, Massimo (Chanovitz) e Giordano.
Grazie a tutti coloro con cui ho passato questi anni, soprattutto le serate: Giacomino, Laura (w i limocelli), Alberto (quanti tandem), Elena (quanti caffè e sigarette), Max (per tutto, tutto).
Grazie a tutti i miei amici di vecchia data: Fede e Boccetta (sempre presenti), Bocceta junior (w le bombette), Viola e Teo, Bigna, Sergio, Tania...tutta la 5^aF; grazie a Chiara, Fra e Marta (w i cappuccini pugliesi alle 5 del mattino).
Grazie ai miei cugini ed amici di Gatta, non vedo l'ora di un altro matrimonio.
Thank you Brent and Swanee and thanks to my little evil boys, Daniel and Caleb, and to the sweet Ester.
Thanks to all the people I know which are somewhere in the Washington State and all over the world (Gerben, Ralph, Philip...Ala), I miss you.
Grazie a Chicco, per essermi sempre stato vicino, per aver sempre rimediato a tutti i

miei casini, informatici e non.
Grazie a te, Fra, sempre sorridente agli imprevisti della vita.

Bibliography

Bibliography

[1] G.Steigman, Int. J. Mod. Phys. E 15, 1 (2006) arXiv:astro-ph/0511534.

[2] C.A.Baker et al., Phys. Rev. Lett. 97, 131801 (2006) arXiv:hep-ex/0602020.

[3] M.Pospelov and A. Ritz, Annals Phys. 318, 119 (2005) arXiv:hep-ph/0504231.

[4] H.Murayama, Talk given at 22^{nd}INS International Symposium on Physics with High EnergyColliders, Tokyo, Japan, 8-10 Mar 1994. Published in Proceedings, eds. S. Yamada and T. Ishii. World Scientific, 1995. 476p. hep-ph/9410285.

[5] H.Davoudiasl, R. Kitano, T. Li and H. Murayama, Phys. Lett. B 609, 117 (2005) arXiv:hepph/0405097.

[6] H. Murayama, Talk given at 22nd INS International Symposium on Physics with High Energy Colliders, Tokyo, Japan, 8-10 Mar 1994. Published in Proceedings, eds. S. Yamada and T. Ishii. World Scientific, 1995. 476p. hep-ph/9410285.

[7] V.F. Weisskopf, Phys. Rev. 56, 72 (1939).

[8] N. Arkani-Hamed and S. Dimopoulos, JHEP 0506, 073 (2005) [arXiv:hep-th/0405159].

[9] V. Agrawal, S.M. Barr, J. F. Donoghue and D. Seckel, Phys. Rev. D 57, 5480 (1998) [arXiv:hepph/9707380].

[10] R. Harnik, G. D. Kribs and G. Perez, Phys. Rev. D 74, 035006 (2006) [arXiv:hep-ph/0604027].

[11] M. Veltman, Acta Phys. Polon. B12, 437 (1981); S. Dimopoulos and S. Raby, Nucl. Phys. B192, 353 (1981); E. Witten, Nucl. Phys. B188, 513 (1981); M. Dine, W. Fischler and M. Srednicki, Nucl. Phys. B189, 575 (1981).

[12] R. Barbieri and G. F. Giudice, Nucl. Phys. B306, 63 (1988); G.W. Anderson and D. J. Castano, Phys. Lett. B347, 300 (1995) [hep-ph/9409419]; Phys. Rev. D 52, 1693 (1995) [hep-ph/9412322].

[13] H. Murayama, Supersymmetry phenomenology, ICTP Summer School in Particle Physics, Trieste, Italy, 21 Jun - 9 Jul 1999. Published in PARTICLE PHYSICS 1999: Proceedings.

[14] Edited by G. Senjanovic and A.Yu. Smirnov. Singapore, World Scientific, 2000. 394p. (ICTP Series in Theoretical Physics, Vol. 16). arXiv:hep-ph/0002232. S. P. Martin, arXiv:hep-ph/9709356.

[15] E. Farhi and L. Susskind, Phys. Rept. 74, 277 (1981).

[16] C. T. Hill and E. H. Simmons, Phys. Rept. 381, 235 (2003) [Erratum-ibid. 390, 553 (2004)] [arXiv:hep-ph/0203079].

[17] D. B. Kaplan and H. Georgi, Phys. Lett. B 136, 183 (1984).

[18] H. Georgi and D. B. Kaplan, Phys. Lett. B 145, 216 (1984).

[19] N. Arkani-Hamed, A. G. Cohen, E. Katz, A. E. Nelson, T. Gregoire and J. G. Wacker, JHEP 0208, 021 (2002) [arXiv:hep-ph/0206020].

[20] N. Arkani-Hamed, A. G. Cohen, E. Katz and A. E. Nelson, JHEP 0207, 034 (2002) [arXiv:hepph/ 0206021].

[21] . S. Manton, Nucl. Phys. B 158, 141 (1979).

[22] L. J. Hall, Y. Nomura and D. R. Smith, Nucl. Phys. B 639, 307 (2002) [arXiv:hep-ph/0107331].

[23] G. von Gersdorff, N. Irges and M. Quiros, Nucl. Phys. B 635, 127 (2002) [arXiv:hepth/0204223].

[24] C. Csaki, C. Grojean and H. Murayama, Phys. Rev. D 67, 085012 (2003) [arXiv:hepph/0210133].

[25] R. Contino, Y. Nomura and A. Pomarol, Nucl. Phys. B 671, 148 (2003) [arXiv:hepph/0306259].

[26] K. Agashe, R. Contino and A. Pomarol, Nucl. Phys. B 719, 165 (2005) arXiv:hep-ph/0412089

[27] .H. C. Cheng, J. Thaler and L. T. Wang, JHEP 0609, 003 (2006) arXiv:hep-ph/0607205.

[28] H. C. Cheng and I. Low, JHEP 0408, 061 (2004) [arXiv:hep-ph/0405243].

[30] S. Nussinov, Phys. Lett. B 165, 55 (1985).

[31] K. G. Begeman, A. H. Broeils and R. H. Sanders, Mon. Not. Roy. Astron. Soc. 249, 523 (1991).

[32] G. G. Raffelt, Dark matter: Motivation, candidates and searches, 1997 European school of high energy physics, Proceedings edited by N. Ellis and M. Neubert. Geneva, Switzerland, CERN, 1998. 351p. (CERN-98-03)arXiv:hep-ph/9712538.

[33] R. H. Cyburt, Phys. Rev. D 70, 023505 (2004) arXiv:astro-ph/0401091.

[34] D. J. Eisenstein et al. [SDSS Collaboration], Astrophys. J. 633, 560 (2005)arXiv:astroph/0501171.

[35] B. J. Carr, Astrophys. J. 201, 1 (1975).

[36] L. J. Hall and S. Hsu, Phys. Rev. Lett. 64, 2848 (1990).

[37] B. Paczynski, Astrophys. J. 304, 1 (1986).

[38] P. Tisserand et al. [EROS-2 Collaboration], arXiv:astro-ph/0607207.

[39] C. Alcock et al. [MACHO Collaboration], arXiv:astro-ph/9803082.

[40] W. M. Yao et al. [Particle Data Group], J. Phys. G 33, 1 (2006).

[41] S. Tremaine and J. E. Gunn, Phys. Rev. Lett. 42, 407 (1979).

[42] D. N. C. Lin and S. M. Faber, Astrophys. J. 266, L21 (1983).

[43] A. Morales, Nucl. Phys. B Proc. Suppl. 87 (2000) 477 `astro-ph/9912554` and Review Talk given at TAUP 2001, Sept. 2001, LNGS,`astro-ph/0112550`, Nucl. Phys. B Proc. Suppl. 110 (2002) 39.

[44] A. K. Drukier, K. Freese and D. N. Spergel, Phys. Rev. D 33 (1986) 3495.

[46] S. Elliott and P. Vogel, Ann. Rev. Nucl. Part. Sci.52 (2002) 115.

[47] V. I. Tretyak and Yu. G. Zdesenko, Atomic Data and Nuclear Data Tables, 80 (2002) 83.

[48] Yu. G. Zdesenko, Rev. Mod. Phys., 74 (2002) 663.

[49] H. Ejiri, Prog. in Part. and Nucl. Phys. B 48 (2002) 185.

[50] A. Morales and J. Morales, Nucl. Phys. B (Proc. Suppl.) 114 (2003) 141

[51] O. Cremonesi, Nucl. Phys. B (Proc. Suppl.) 118 (2003) 287

[52] A. Giuliani, Talk given at the 8th Int. Workshop on Topics in Astroparticle and Underground Physics (TAUP2003), 5 - 9 September, 2003, Seattle, USA.

[53] Y. Fukuda et al., the SuperKamiokande Collaboration, Phys. Rev. Lett., 85 (2000) 3999

[54] T. Toshito et al., the SuperKamiokande Collaboration, Proceedings of the XXXVIth Rencontres de Moriond on Electroweak Interactions and Unified Theories and `arXiv:hep-ex/0105023`.

[55] Y. Hayato et al., the SuperKamiokande Collaboration, Talk given at the Int. EPS Conference on High Energy Physics, July 17 - 23, 2003, Aachen, Germany.

[56] M. Ambrosio et al., the MACRO Collaboration, Phys. Lett. B 566 (2003) 35.

[57] Q. R. Ahmad et al., the SNO Collaboration, Phys. Rev. Lett. 87 (2001) 071301.

[58] Q. R. Ahmad et al., the SNO Collaboration, Phys. Rev. Lett. 89 (2002) 011301 and 011302.

[59] S. N. Ahmed et al., the SNO Collaboration,`arXiv:nucl-ex/0309004`.

[60] S. Fukuda et al., the SuperKamiokande Collaboration, Phys. Lett. B 539 (2002) 179.

[61] M. B. Smy et al., the SuperKamiokande Collaboration, `arXiv:hep-ex/0309011`.

[62] K. Eguchi et al., the KamLAND Collaboration, Phys.Rev.Lett. 90 (2003) 021802, and `arXiv:hep-ex/0310047`.

[63] M. Apollonio et al., the CHOOZ Collaboration, Phys. Lett. B 466 (1999) 415.

[64] M. H. Ahn et al., the K2K Collaboration, Phys.Rev.Lett. 90 (2003) 041801.

[65] S. Pascoli and S. T. Petcov, Phys. Lett. B 544 (2002) 239, and Addendum, arXiv:hep-ph/0310003.

[66] M. Maltoni, T. Schwetz, M. A. Tortola and J. W. F. Valle,arXiv:hep-ph/0309130

[67] F. Feruglio, A. Strumia and F. Vissani, Nucl. Phys. B 637 (2002) 345, and Addendum, Nucl. Phys. B 659 (2003) 359.

[68] S. M. Bilenky, S. Pascoli and S. T. Petcov, Phys. Rev. D 64 (2001) 053010.

[69] H. V. Klapdor-Kleingrothaus, H. Ps, A. Yu. Smirnov, Phys. Rev. D 63 (2001) 073005.

[70] T.Tomoda, Rep. Prog. Phys. 54, (1991), pp. 53-126.

[71] Journal of Physics: Conference Series 173 (2009).

[72] M. Kortelainen, O. Civitarese, J. Suhonen, J. Toivanen, Phys. Lett. B 647 (2007) 128.

[73] M. Kortelainen, J. Suhonen, Phys. Rev. C 76 (2007) 024315.

[74] M. Mayer, Phys. Rev. 75 (1949) 1969.

[75] M. Kortelainen, J. Suhonen, Phys. Rev. C 76 (2007) 024315.

[76] O. Axel, J.H.D. Jensen, H.E. Suess, Phys. Rev. 75 (1949) 1766

[77] To build and diagonalize the Hamiltonian matrix.

[78] E. Caurier, G. Martinez-Pinedo, F. Nowacki, A. Poves, A.P. Zuker, Rev. Modern Phys. 77 (2005) 427.

[79] Tomoda, F. Faessler, K.W. Schmid and F. Grummer, Nuc. Phys. 452 A 591 (1986).

[80] Masaru Doi, Tsuneyuki Kotani and Eiichi Takasugi, Prog. Theor. Phys. Supp. 83 1 (1985).

[81] G. Pantis, F. Simkovic, J. D. Vergados and Aman Faessler, Phys. Rev. C 53 695 (1996).

[82] F. Iachello and A. Arima, The Interacting Boson Model, Cambridge University Press, 1987.

[83] F.Iachello and P. Van Isacker, The Interacting Boson Fermion Model, Cambridge University Press, 1991

[84] T. Otsuka, A. Arima and F. Iachello, Nucl. Phys. A309, 1 (1978).

[85] A. Arima, T. Otsuka, F. Iachello, and I. Talmi, Phys. Lett. B66, 205 (1977).

[86] T. Otsuka, A. Arima, and F. Iachello, Nucl. Phys. A309, 1 (1978).

[87] T. Tomoda, Rep. Prog. Phys. 54, 53 (1991).

[88] Simkovic et al., PRC60(1999)

[89] Suhonen et al., PRC53(1996)

[90] Suhonen et al , PR300(1998)

[91] Suhonen et al. JoP: Conference series 173 (2009) 012012

[92] Tomoda et al., RPP54(1991)

[93] Simkovic et al. PRC 77 (2008) 045503

[94] Suhonen et al. JoP: Conference series 173 (2009) 012012

[95] Poves et al. NPA 818 (2009) 139

[96] Iachello et al. PRC 79 (2009) 044301

[97] C. Kittel, Introduction to Solid State Physics, 7th ed. (Wiley, 1996).

[98] M. Barucci et al., J. Low Temp. Phys. 123, 303 (2001).

[99] A. Alessandrello et al., Phys. Lett. B247, 442 (1990).

[100] D. McCammon, Appl. Phys. 99, 35 (2005),arXiv:physics/0503086

[101] E. E. Haller, J. Appl. Phys. 77, 2857 (1995).

[102] C. Arnaboldi, G. Pessina, and E. Previtali, IEEE Trans. Nucl. Sci. 50, 979 (2003).

[103] A. Alessandrello et al., Nucl. Instrum. Meth. A412, 454 (1998)

[104] E. Fiorini and T. O. Niinikoski, Nucl. Instr. Meth. A224, 83 (1984).

[105] A. Alessandrello et al., Phys. Lett. B335, 519 (1994).

[106] A. Alessandrello et al., Phys. Lett. B433, 156 (1998).

[107] A. Alessandrello et al., Phys. Lett. B486, 13 (2000).

[108] CUORICINO Collaboration, C. Arnaboldi et al., Phys. Rev. C78, 035502 (2008), arXiv:0802.3439

[109] F. Bellini et al., Astropart. Phys. 33, 169 (2010), arXiv:0912.0452

[110] E. Andreotti et al., Submitted to Astropart. Phys. (2010), arXiv:0912.3779.

[111] C. Arnaboldi et al., Submitted to J. Crystal Growth (2010).

[112] R. Ardito et al., (2005), arXiv:hep-ex/0501010.

[113] H. V. Klapdor-Kleingrothaus et al., Latest Results from the Heidelberg-Moscow Double Beta Decay Experiment, Eur. Phys. J., vol. A12, pp. 147154, 2001, hep-ph/0103062

[114] S. P. Ahlen et al., Study of penetrating cosmic ray muons and search for large scale anisotropies at the Gran Sasso Laboratory, Phys. Lett., vol. B249, pp. 149 156, 1990.

[115] P. Belli et al., Deep underground neutron flux measurement with large bf-3 counters, Nuovo Cim., vol. A101, pp. 959966, 1989.

[116] C. Arnaboldi et al., The temperature stabilization system of CUORICINO: An array of macro bolometers, IEEE Trans. Nucl. Sci., vol. 52, pp. 16301637, 2005.

[117] C. Arnaboldi, G. Pessina, and E. Previtali, A programmable calibrating pulse generator with multi- outputs and very high stability, IEEE Trans. Nucl. Sci., vol. 50, pp. 979986, 2003

[118] A. Alessandrello et al., Measurements of internal radioactive contamination in samples of Roman lead to be used in experiments on rare events, Nucl. Instrum. Meth., vol. B142, pp. 163172, 1998

[119] M. Pedretti. et al., Measurement of thermal properties for modeling and optimization of large mass bolometers, Physica B, vol. 329, pp. 16141615, 2003.

[120] E. Fermi and C.N. Yang, Phys. Rev. 76 1379 (1949).

[121] J.N. Bahcall, Rev. Mod. Phys. 50, 881 1978!; Neutrino Astrophysics Cambridge University Press, Cambridge, England, 1993, p. 360

[122] PDG :`http://pdg.lbl.gov`.

[123] S. Capelli and M. Pavan, CUORE Collaboration Internal Note 2007-01.

[124] A. Bryant, CUORE Collaboration Internal Note 2010-02

[125] WebElements: the periodic table on the web `http://www.webelements.com`

[126] Phys. Rev. C.78 (2008) 035502

[127] I. Avignone, Frank T., S. R. Elliott, and J. Engel, Double Beta Decay, Majorana Neutrinos, and Neutrino Mass, Rev. Mod. Phys., vol. 80, pp. 481516, 2008, 0708.1033.

[128] S. Di Domizio, "Search for Double Beta Decay to Excited States with CUORICINO and Data Acquisition System for CUORE" Universit degli Studi di Genova - Scuola di Dottorato in Scienze e Tecnologie per l'Informazione e la Conoscenza - XXI Ciclo - A.A. 2006-2009 `http://www.roma1.infn.it/exp/cuore/thesis.html`

[129] .A. Simpson Ann. Rev. Nucl. Part. Sci. ,33:323 (1983)

[130] J.C. Pati and A. Salam, Phys. Rev. Lett. 31 275 (1973).

[131] S.Weinberg, E.Witten, " Limits on massless particles", Physics Letters B, vol.96, pp. 59-61, (1980).

[132] H.V. Klapdor-Kleingrothaus, I.V. Krivosheina, I.V. Titkova, "A new experimental limit for the stability of the electron", Physics Letters B 644 (2007) pp. 109118.

[133] M.Suzuki, "Slightly massive photon", Phys.Rev.D, vol.38, number 5, 1998.

[134] L.B.Okun and Ya.B.Zeldovich, Phys.Lett, **78B**, 597(1978).

[135] M.B.Voloshin and L.B.Okun, Pis'ma Zh. Eksp. Teor.Fiz **28**, 156(1978)[JETP Lett.**28**, 145 (1978)].

[136] S.Weinberg, Phys.Rev.Lett.**13**, 495(1964).

[137] `http://pdglive.lbl.gov/Rsummary.brl?nodein=S066`